TAMPERE UNIVERSITY OF TECHNOLOGY

VILLE VUORINEN

FRONT-END ELECTRONICS FOR FAST IN VITRO BIOLOGICAL MEASUREMENTS

MASTER OF SCIENCE THESIS

Examiners and topic approved by the Faculty Council of the Faculty of Computing and Electrical Engineering on April 4th 2012.

Examiners: Professor Jari Hyttinen
Research fellow Tomi Roinila

ABSTRACT

TAMPERE UNIVERSITY OF TECHNOLOGY
Degree Programme in Electric Engineering
VUORINEN, VILLE: Front-end Electronics for Fast in Vitro Biological Measurements.
Master of Science Thesis, 95 pages, 6 Appendix pages
December 2012
Major subject: Biomedical Engineering
Examiners: Professor Jari Hyttinen, research fellow Tomi Roinila
Keywords: binary sequence, bioimpedance, electrochemical impedance spectroscopy, retinal pigment epithelium

Epithelium forms tight membranes that efficiently take part in secretion and absorption between the two lining tissues. A tight membrane of this nature has a low DC conductivity and this is generally used to assess the integrity of cultured epithelium cell layers. Recent studies have shown that impedance spectroscopy gives more information about the electrophysiological structure of the cells.

Collaborative research by Department of Biomedical Engineering at Tampere University of Technology and stem cell research group at University of Tampere has shown that electrochemical impedance spectroscopy is useful in assessing the maturity and functionality of differentiated retinal pigment epithelium (RPE) cells. However the time expenditure of the traditional frequency sweeping method is a poor candidate for drug permeability or multichannel studies where several frequency responses have to be measured within a short time. The aim of this Thesis was to develop the front end electronics for fast impedance spectroscopy measurement employing inverse-repeat binary sequence as the broadband excitation signal. Also the DC potential across the cell membrane was to be measured with the device.

The developed device was first tested using a custom built test box and plastic film as artificial membrane. In addition several electrode materials were used to study the observed polarization impedances. Further testing with differentiated RPE cell layers was done using the Ussing chamber and the well plate setups that are commonly used in cell culturing studies. All the measured frequency responses were referenced with a commercial device widely used in epithelium research.

The observed measurement differences between the device and the reference were largely caused by the load dependent output current of the device and by the electrode polarization taking place at the voltage measurement electrodes. Due to the input current error the relative difference of the measured impedance levels was typically from 5 % to 10 % with load impedances larger than 700 ohms. With lower load impedances the measured relative difference increased rapidly. A method to compensate for the input current error is presented in this thesis. DC potential measurements with the device were not successful as the electrodes used had very high offset voltages.

The frequency responses measured with the device give a good measure of the capacitance present in the cell layer. Capacitance of the cell layer can be used to assess the maturity of the cell layer and for such purpose the device suits well. For impedance level measurements the device has a relatively large error margin and further research needs to be done to improve the accuracy and to eliminate the DC current flow. In addition the accuracy of the measurement system would improve by dividing the input stage between the DC potential and frequency response measurements. Also more carefully designed electrodes would help to control the electrode offset voltages.

TIIVISTELMÄ

TAMPEREEN TEKNILLINEN YLIOPISTO
Sähkötekniikan koulutusohjelma
VUORINEN, VILLE: Elektroniikan pääteaste nopeisiin biologisiin in vitro mittauksiin.
Diplomityö, 95 sivua, 6 liitesivua
Joulukuu 2012
Pääaine: Lääketieteellinen tekniikka
Tarkastajat: Professori Jari Hyttinen, tutkijatohtori Tomi Roinila
Avainsanat: binäärisekvenssi, bioimpedanssi, retinan pigmenttiepiteeli, sähkökemiallinen impedanssi-spektroskopia

Epiteelisolut muodostavat tiivisliitoksia, jotka ovat tärkeässä roolissa kudosten välillä tapahtuvassa erityksessä sekä absorptiossa. Tiivisliitoksen tasavirtajohtavuus on heikko ja tätä ominaisuutta hyödynnetään yleisesti viljeltyjen epiteelisolukerrosten tiiviyden sähköisessä tarkastelussa. Tutkimukset ovat kuitenkin osoittaneet, että impedanssispektroskopia antaa enemmän tietoa solujen elektrofysiologisesta rakenteesta kuin yksinkertainen resistanssimittaus.

Tampereen Teknillisen Yliopiston Biolääketieteen laitos sekä Tampereen Yliopiston kantasolututkimusryhmä ovat yhteistyössä osoittaneet elektrokemiallisen impedanssispektroskopian soveltuvan kantasoluista erikoistettujen retinan pigmenttiepiteelisolujen (RPE) kypsyyden ja toiminnallisuuden arviointiin. Perinteiset taajuuspyyhkäisyä hyödyntävät taajuusvasteanalysaattorit soveltuvat kuitenkin hitaudeltaan heikosti tutkimuksiin, joissa mittauskohteessa tapahtuu nopeita muutoksia tai missä useita taajuusvasteita mitataan lyhyellä aikavälillä. Tämän diplomityön tavoitteena oli kehittää pääteasteen elektroniikka mittausjärjestelmälle, joka hyödyntää laajakaistaista binäärijaksoa herätesignaalina ja mahdollistaa näin huomattavasti nopeamman impedanssispektroskopian. Kehitettävän laitteen tuli myös mitata solukerroksen yli oleva DC potentiaali.

Diplomityössä kehitettyä laitetta testattiin aluksi in vitro mittauksia varten kehitetyllä testijärjestelmällä, jossa solukerrosta jäljiteltiin ohuella muovikalvolla. Näissä mittauksissa testattiin myös eri elektrodimateriaalien vaikutus havaittuun polarisaatioimpedanssiin. Viljeltyjen RPE solujen taajuusvasteita mitattiin työssä käyttäen sekä Ussingin kammio- että kuoppalevymittausasetelmia. Laitteella mitattujen taajuusvasteiden hyvyyttä arvioitiin vertaamalla tuloksia kaupallisella taajuusvasteanalysaattorilla mitattuihin vasteisiin.

Kehitetyllä laitteella mitattujen vasteiden ero analysaattorilla mitattuihin johtui suurilta osin herätevirran riippuvuudesta kuormasta sekä jännitemittauselektrodien polarisaatioimpedansseista. Yli 700 ohmin kuormilla herätevirrasta aiheutuva virhe oli tyypillisesti 5 % – 10 %, kun taas matalimmilla kuormilla virhe kasvoi nopeasti. Tämän virheen kompensoimiseksi on kuitenkin esitetty metodi tässä diplomityössä. Epiteelisolukerroksen yli olevaa DC jännitettä ei onnistuttu mittaamaan johtuen käytettyjen elektrodien korkeista offset-jännitteistä.

Tässä diplomityössä kehitetyllä laitteella mitatut taajuusvasteet noudattavat hyvin analysaattorilla mitattujen vasteiden käyrämuotoja ja laite soveltuu täten solukerroksen kapasitanssin arviointiin. Solukerroksen kapasitanssia voidaan käyttää apuna solujen kypsyyden arvioinnissa. Laitteella mitatut impedanssitasot eroavat kuitenkin analysaattorilla mitatuista ja jatkokehitys DC virtojen eliminoimiseksi sekä elektrodien erisuuruisten offset-jännitteiden kompensoimiseksi on suositeltavaa.

PREFACE

This Master of Science thesis was carried out at the Department of Biomedical Engineering of Tampere University of Technology. The functionality of the device was tested at Finn-Medi while the cell measurements were performed at Regea Cell and Tissue Center. The funding for thesis was provided by the Human Spare Parts project, a research program of BioMediTech.

I would like to express my gratitude to professor Jari Hyttinen and research fellow Tomi Roinila for all the invaluable guidance and advice they have provided. I would also like to give special thanks to MSc Virpi Savolainen for her expertise with the RPE cells and measurement practicalities. I have also been helped by various other people during the process, including Pasi Kauppinen, Raimo Peurakoski and Jarmo Verho. My sincere thanks to all of you.

Finally I want to thank Kaisa for her unfailing encouragement during all these years.

This work is dedicated to my father who passed away in 2006.

Tampere 19.11.2012

Ville Vuorinen

CONTENTS

ABSTRACT II
TIIVISTELMÄ III
PREFACE IV
CONTENTS V
NOTATIONS AND ABBREVIATIONS VII
1 INTRODUCTION 1
2 THEORETICAL BACKGROUND 4
2.1 BIOIMPEDANCE 4
2.1.1 Electrical Impedance 4
2.1.2 Frequency Variation and Representation of Bioimpedance 5
2.2 IMPEDANCE MEASURING TECHNIQUES 8
2.2.1 Analog Methods 8
2.2.2 Sine Correlation 10
2.2.3 Pulse Excitation Methods 14
2.3 EPITHELIAL TISSUE 19
2.3.1 Electric Properties of Epithelium 19
2.3.2 Equivalent Circuit Models of Epithelium 20
2.3.3 Frequency Response of Epithelium 23
2.4 IN VITRO MEASUREMENTS OF TISSUES 24
2.4.1 Measurement Errors 25
2.4.2 Ussing Chamber 28
2.5 COMMERCIAL APPLICATIONS OF IMPEDANCE SPECTROSCOPY 30
2.6 ELECTRONIC DESIGN 33
2.6.1 Current Injection 33
2.6.2 Voltage Sensing 35
2.6.3 Optocoupling 36
2.6.4 DC Potential Measurement 37
3 METHODS 39
3.1 COMPONENT SELECTION 39
3.1.1 Optocouplers 39
3.1.2 Operational amplifiers 40
3.1.3 Instrumentation amplifiers 40
3.1.4 Other components 41
3.2 SIMULATION OF THE ELECTRODE IMPEDANCES 43
3.3 MEASUREMENT SYSTEM 45
3.3.1 Generation of the Excitation Signals 45
3.3.2 Data Acquisition 46
3.3.3 Implementation of Electronics 46
3.3.4 Experimental Setups 51
3.3.5 Parafilm M and RPE Cells 55

3.4 MEASUREMENT PROCEDURE 57
4 RESULTS 58
4.1 SIMULATION OF POLARIZATION EFFECTS 58
4.2 EQUIVALENT CIRCUIT FREQUENCY RESPONSE 61
4.3 IN VITRO MEASUREMENTS WITH THE FIRST PROTOTYPE 63
4.3.1 Test Box with Ag/AgCl Electrodes 63
4.3.2 Impedance Levels with Different Electrode Materials 65
4.3.3 Ussing Chamber measurements 69
4.3.4 Frequency Dependency of the Measurement Differences 71
4.4 IN VITRO MEASUREMENTS WITH THE SECOND PROTOTYPE 72
4.4.1 Test Box with Ag/AgCl electrodes 72
4.4.2 Well Plate Measurements 77
4.4.3 Transepithelial potentials 78
4.4.4 Noise Measurements 78
4.5 OUTPUT IMPEDANCE COMPENSATION 79
4.5.1 Current output error 79
4.5.2 Compensated RPE impedances 80
5 DISCUSSION 82
5.1 ANALYSIS OF THE MEASUREMENT RESULTS 82
5.2 SOURCES OF ERROR IN THE MEASUREMENT SYSTEM 84
5.3 FUTURE CONSIDERATIONS 86
5.4 CONCLUSIONS 87
REFERENCES 88
APPENDIX 1: EXCITATION SCRIPT 96
APPENDIX 2: COMPONENT LISTING 99
APPENDIX 3: COMPLETE SCHEMATICS OF THE DEVICE 100

NOTATIONS AND ABBREVIATIONS

Notations

C	Capacitor
C_1, C_2, C_3	Capacitors used in schematics
c_1, c_2	Concentrations of the liquid junction
C_{ap}	Capacitance of apical membrane
C_{bl}	Capacitance of basal membrane
C_{epi}	Epithelial capacitance
C_p	Polarization capacitance
C_{p1}, C_{p2}	Polarization capacitances
E	System voltage
G	Frequency response function
G_m	Measured frequency response function
H	Transfer function
i	Excitation current used in schematics
i_0	Output current of a current source
I, I_{exc}	System excitation current
IA_1	Instrumentation amplifier used in the schematics
I_F	Forward current of diode
I_{PD1}, I_{PD2}	Photodiode currents
$K1$, $K2$, $K3$	Optocoupler gains
k_B	Boltzmann's constant
n	Number of electrons in the unit reaction
N_f	Number of integration cycles
OA_1, OA_2	Operational amplifiers used in schematics
P	Sine wave perturbation
R	System resistance
R_0	Resistance of Cole-Cole plot at zero frequency
R_∞	Resistance of Cole-Cole plot at infinite frequency
R_1, R_2, R_3, R_4,R_5, R_6	Resistors used in circuits
R_{ap}	Resistance of apical membrane
R_{bl}	Resistance of basal membrane
R_{epi}	Epithelial resistance
R_p	Polarization resistance
R_{p1}, R_{p2}	Polarization resistances
R_{para}	Paracellular resistance
R_{set}	Resistor used to set the excitation current level
R_{sub}	Subepithelial resistance
R_{trans}	Transepithelial resistance
S	Response to sine wave perturbation
T	Absolute temperature in kelvins
T_{exc}	Duration of chirp excitation
U	Potential across a conductor
U_{offset}	Potential difference due to imbalance of operational amplifiers' input stages
v	Control voltage used to generate the excitation current in a basic membrane experiment

v_n	Thermal noise RMS value
Δv	Voltage measured over the membrane in a basic membrane experiment
V_0	Material specific standard half-cell potential
V_{CC}	Supply voltage
V_F	Forward voltage of a diode
V_{in}	Input voltage of a circuit
V_Z	Voltage across unknown impedance
V_{ch}	Chirp excitation pulse
V_e	Error voltage due to polarization
X	System reactance or Fourier transformed excitation
x	System excitation
x_k	Maximum length binary sequence
Z	System impedance
$\tilde{\boldsymbol{Z}}$	Total impedance vector
Z_1, Z_2, Z_3, Z_4	Impedance elements of AC bridge
Z_{eq}	Equivalent circuit
Z_f	Impedance of practical Cole-Cole plots
Z_{Im}	Imaginary part of complex impedance
Z_L	Load impedance
Z_O	Output impedance of a current source
Z_p	Polarization impedance
Z_{Re}	Real part of complex impedance
α, β, Δe, Δi, Δi	Lissajous figure parameters
$\alpha_{C\text{-}C}$	Cole-Cole plot depression angle exponent parameter
α_{ox}, α_{red}	Ion concentration specific activities
θ	Phase angle
τ	Time constant

Abbreviations

AC	Alternating Current
BW	Bandwidth
CMRR	Common Mode Rejection Ratio
DAQ	Data Acquisition System
DC	Direct Current
DUT	Device Under Test
EIS	Electrochemical Impedance Spectroscopy
EIT	Electrical Impedance Tomography
FFT	Fast Fourier Transform
FRA	Frequency Response Analyzer
FRF	Frequency Response Function
GBP	Gain-Bandwidth Product
IA	Instrumentation Amplifier
IC	Integrated Circuit
IPS	Induced Pluripotent Stem cell

IRS	Inverse-Repeat Binary Sequence
LED	Light-emitting Diode
LIS	Lateral Intercellular Space
MLBS	Maximum-length Binary Sequence
PRBS	Pseudo-random Binary Sequence
RMS	Root Mean Square
RPE	Retinal Pigment Epithelium, cell layer between choroid and retinal visual cells.
SNR	Signal-to-Noise Ratio
TEP	Transepithelial Potential
TER	Transepithelial Resistance
TJ	Tight Junction

1 INTRODUCTION

Impedance measurements of biological matter provide information about the resistive and dielectric properties of the sample under study. Resistance and potential measurements of epithelial tissue have been done for nearly fifty years and also the impedance of epithelial tissue has been examined for several decades. The aims of many of the early studies have been in determining an electrical model for epithelial cells and thus increase understanding of the cellular structure. (Cole 1965; Schifferdecker 1978) More recently these models have been used in cell culturing in assessing the integrity and maturity of the cell layer (Krug et al. 2009; Savolainen et al. 2011; Onnela et al. 2012).

In order to build an equivalent circuit with capacitive and resistive elements the measurements are typically done in the frequency domain; that is, the models are obtained as frequency responses. The prevailing technique to obtain the responses has been the use of a sine-sweep-based network analyzer. The use of the sweeps usually yields reliable and accurate responses but the method suffers from some deficiencies of which the most vital one is the length of time required for a complete measurement. A single frequency sweep can take up to several minutes depending on the desired frequency resolution. As the addition of drugs or chemical agents can induce changes in the electrical properties of cells, these changes cannot be measured due to the time expenditure of the method. (Asphahani 2007; Grimnes & Martinsen 2008)

An additional property of interest in cell measurements is the transepithelial potential (TEP). In several studies this potential has been measured with a battery operated, handheld device, where user inserts the “chopstick” electrodes by hand (McNeil 2006; Savolainen 2011b). This method is prone to error and a potential measurement using fixed electrodes can eliminate errors due to variations in electrode placement.

There are variety of devices available on the market for measuring electrical properties of biological materials. Low-cost devices such as volt-ohm meters can be used to determine transepithelial potential (TEP) and transepithelial resistance (TER) (Millipore, 2012; World Precision Instruments, Inc. 2012). Also LCR-meters employing the auto-balancing bridge technique can be used in determining TER (Agilent Technologies, 2012). More expensive impedance analysers are able to cover frequency ranges up to tens of MHz. With the addition of front-end amplifiers and impedance interfaces the impedance can be measured highly accurately using four-terminal setup. Most of the older devices used to apply the traditional frequency-sweep, but more modern equipment employ a faster method; time domain spectroscopy. (Good Will Instrument Co. 2010; Grimnes & Martinsen 2008; Molecular Devices 2012; nanoAnalytics 2012a; Solartron Analytical 2011a)

Fundamental division between techniques can be made according to the independent variable present in measurements. This can be either frequency or time. Frequency domain methods usually consist of applying a sine wave excitation and measuring the response. Modern computers however have paved way for time domain measurements that utilize time-to-frequency conversions like Fourier and Laplace transformations. With time domain methods the excitation signal is designed so that it covers the frequency band of interest with multiple discrete frequencies. The resulting time domain response is transformed to frequency domain and this enables the use of powerful signal processing algorithms. (Barsaukov & MacDonald 2005)

The time taken by the traditional sweep-based measurement can be drastically reduced by using broad-band excitation signals such as the maximum-length pseudorandom binary sequence (MLBS) and correlation techniques. The MLBS-based measurement techniques have been used as a general method (Sun et al. 2007) to measure the frequency responses of various linear systems. They have been applied for example for impedance spectroscopy of single living cells and acoustics (Gawad 2007; Vanderkooy 1994). The specific challenge in the application of the thesis is to design a high-quality current source that feeds precise wide-band excitation current. This is a complex task due to noise and various non-idealities. There are many studies that present different solutions for the front-end electronics used in wide-band impedance measurements. However, most of these studies concentrate on microfluidic applications (Annus, 2008; Ojarand, 2011; Pliquett, 2010).

The Human Spare Parts is a TEKES funded research program that involves University of Tampere and Tampere University of Technology. One of the aims of the program is to develop sensors and measurement methods for analysis and validation of biological systems and their functions. One of the application areas is electrophysiological assessment of cellular functions of stem cell -derived retinal pigment epithelium (RPE). The motivation for this is the age-related macular degeneration found in five percent of the Finnish population. (BioMediTech2012) There are no effective treatments for the condition at the moment and drug therapy only slows down the progress of the disease. If left untreated, the degeneration ultimately leads to blindness. The studies by Onnela et al. (2012, p. 112) and Savolainen et al. (2011, p. 3066) show that the development and confluence of the cultivated RPE cell layer can be assessed with impedance analysis without harming the cells.

The objective of this thesis is to develop a device for impedance spectrum and transepithelial potential measurements using macro-size electrodes and pulse excitation. This requires designing of a constant wide-band current injection circuitry. Once a stable enough current feeding with an adequate bandwidth has been achieved it will be tested with voltage sensing circuitry and MLBS signal using an equivalent load circuit of cell layer and electrodes. After the equivalent circuit measurements the performance of the device will be tested with in vitro measurements using a plastic test box and a plastic film as the artificial membrane. Finally the frequency response measurements

will be done with live RPE cells. All the measurement results will be referenced with a sine-sweep network analyser.

2 THEORETICAL BACKGROUND

This chapter introduces the theoretical concepts used in the thesis. **Chapter 2.1** presents the variable to be measured and its variation in tissue with frequency. Also the connection between the measured frequency response and the electrical properties of tissue under study is explained. **Chapter 2.2** is a review of the most common techniques and excitation signals used in the field of impedance spectroscopy. Both the frequency domain and the time domain approaches are discussed. **Chapter 2.3** introduces the object of measurements, epithelial cell layer. Several different electrical equivalents of the cell layer are presented and the effect of cell layer confluence on the frequency response is explained in detail. **Chapter 2.4** focuses on the experimental setup used with in vitro impedance measurements and also presents the two important sources of voltage measurement errors, the equilibrium potential under zero current conditions and the electrode polarization. **Chapter 2.5** presents the commercial applications of impedance spectroscopy and few other applications of interest. Finally **Chapter 2.6** contains the theory used in the design of the front-end electronics. This chapter also gives the prerequisites and requirements for the next chapter where component selection is introduced.

2.1 Bioimpedance

Impedance is the frequency dependent property of an object to resist (*impede*) current flow. Bioimpedance describes this property in a living organism or in an organism that has lived. The tissue under study may be from a human, plant or animal. Measurement of bioimpedance is non-destructive and non-invasive and it can be used to characterize and identify different tissue types. This has made it widely popular for research purposes and as a result also various commercial applications exist. Different clinical applications of bioimpedance are for example impedance cardiography, the determination of body composition, detection of tumours and quantification and classification of skin irritation. (Grimnes & Martinsen 2008)

2.1.1 Electrical Impedance

According to Ohm's law, resistance R describes the relationship between the direct current (DC) I flowing through a conductor and the potential U measured across the conductor. Impedance extends this relationship to alternating current (AC) circuits by presenting the impedance as a complex ratio of the voltage U to the current I. The real part Z_{Re} of the impedance represents the frequency independent resistance R and the com-

plex part Z_{Im} the frequency dependent reactance X. The sign of the reactance determines whether the total circuit reactance is capacitive or inductive.

A circuit that has a nonzero reactance exhibits a phase shift. This means that the current flowing through the circuit is not in phase with the voltage applied across the circuit. Phase angle θ describes how much the current is ahead of the voltage. A graphical representation of the complex impedance can be seen in **Figure 2.1**.

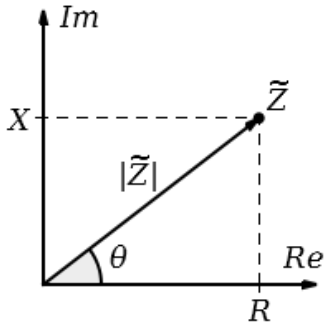

Figure 2.1. *The complex impedance plane with real element R and imaginary element X. The magnitude of impedance $\tilde{Z}$ is shown as $|\tilde{Z}|$with phase angle θ.*

The magnitude of the impedance $\tilde{Z}$can be derived according to equation (1) while the phase angle θ can be calculated using a basic trigonometric function.

$$|\tilde{Z}| = \sqrt[2]{R^2 + X^2} \tag{1}$$

$$\theta = arctan\left(\frac{X}{R}\right) \tag{2}$$

2.1.2 Frequency Variation and Representation of Bioimpedance

All biomaterials exhibit dispersion, that is, frequency dependent permittivity.(Grimnes & Martinson 2008). As permittivity decreases due to loss of different polarization processes the circuit's ability to store energy decreases. This is seen as higher conductance or in other words, lower impedance. Schwan and Kay (1957b) presented three dispersion groups for tissues and cell suspensions termed α-, β- and γ-dispersions, according to their mechanisms. At the lowest frequency range the first step-like decrease of permittivity, α-dispersion, is due to tangential flow of ions across cell surfaces and active cell membrane effects. The next dispersion region, β-dispersion, results from passive cell membrane capacitance, intracellular organelle membranes and build-up of charge due to Maxwell-Wagner effect. The disperse phenomena taking place at the high frequencies, γ-dispersion, is due to dipolar rotation of media such as water, salts and proteins. (Markx & Davey 1999; Grimnes & Martinson 2008) The dispersion regions are shown in **Figure 2.2**.

When the impedance is measured using several frequencies the procedure is called impedance spectroscopy. The result is known as frequency response that can be

represented by using a Bode plot, a graph that plots the logarithmic impedance versus logarithmic frequency (Dorf & Bishop 2008). Also the phase information describing frequency dependent phase shift is usually included in the Bode plot. Bode plots are also used to illustrate corner frequencies that are extensively in electronic filter design. A corner frequency is the frequency where the impedance level has dropped by three decibels.

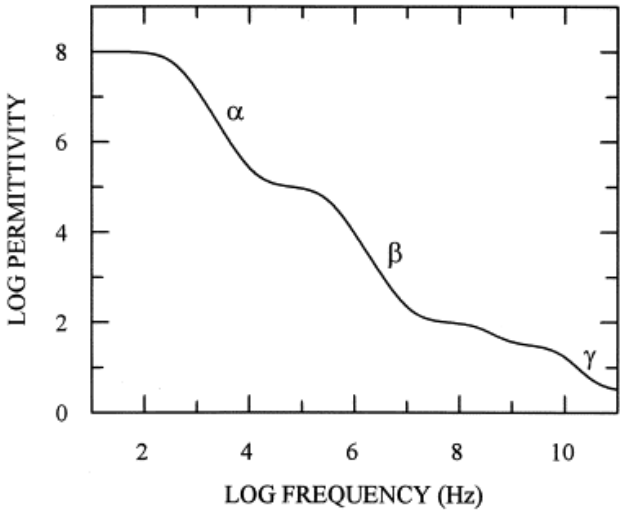

Figure 2.2. *Idealized dispersion regions for tissues and cell suspensions. (modified from Markx & Davey 1999)*

Another method to represent the tissue impedance as a function of frequency is the Cole-Cole plot (Cole & Cole 1941). This method plots the real component R versus imaginary component X in the complex series impedance with the frequency as parameter. **Figure 2.3A** presents a three element model of tissue impedance that exhibits a single time constant τ. This time constant is produced by a resistor $R_2$and a capacitor C connected in parallel. The Cole-Cole plot of this circuit is a semicircle with radius $(R_0-R_\infty)/2$, where R_0 is the dc resistance of the circuit and R_∞ the resistance of the circuit at infinite frequency. The theoretical plot can be seen in **Figure 2.3B**.

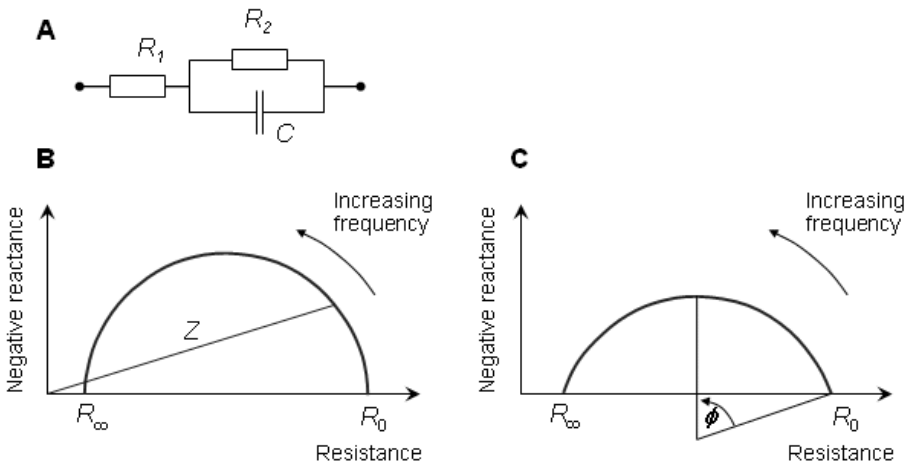

***Figure 2.3**. A) Three element model of tissue impedance with a single time constant. B) Corresponding theoretical Cole-Cole- plot with Z as the frequency dependent impedance.C) Practical Cole-Cole- plot with depression angle ϕ.(Malmivuo & Plonsey 1995)*

In practise the plot is not necessarily on the real axis, but can be depressed below it, so Schwan & Kay (1957a) formulated the following equation for impedance Z_f to represent practical measurements

$$Z_f = R_0 + \frac{R_0 - R_\infty}{1 + j\omega\tau^{(1-\alpha_{C-C})}} \quad (3)$$

where $\omega = 2\pi f$ and $\alpha_{C\text{-}C}$ is related to the depression angle $\phi = (1 - \alpha_{C\text{-}C})\pi/2$.

2.2 Impedance Measuring Techniques

This chapter presents the most common techniques to measure impedance. The following **Chapters 2.2.1 and 2.2.2** describe three common frequency domain methods to measure the system impedance. The transfer function *G* of a system can be expressed as a ratio of output and input signals:

$$G(j\omega) = \frac{X_{out}(j\omega)}{X_{in}(j\omega)} \tag{4}$$

In the special case where the output signal is the system voltage *E* and the input is excitation current *I*, the transfer function is the system impedance *Z*.

$$G(j\omega) = \frac{E(j\omega)}{I(j\omega)} = Z(j\omega) \tag{5}$$

As stated in **Chapter 2.1**, the impedance amplitude and phase may change in respect to input. This is why we must express the impedance *Z* in complex form

$$Z(j\omega) = Z' + jZ'' \tag{6}$$

where *Z'* is the real part and *Z''* is the complex part of the system impedance *Z*.

The first of the following chapters presents the analog methods more common in the past whereas the second chapter describes the impedance measurement technique used by commercial frequency response analysers. **Chapter 2.2.3** presents two time domain methods.

The standard methods presented in following chapters require a sufficiently small perturbation so that the response is linear (Barsaukov & MacDonald 2005). In practise the low end value is limited by noise level. It should be also noted that nonlinearities may occur due to external reasons, for example electrode polarization (Grimnes & Martinsen 2008).

2.2.1 Analog Methods

In the past the measurements were purely based on analysis of analog signals. Before the advent of modern computers one direct analog method for measuring impedance was to record the input voltage and current (a voltage across a series resistance) with two-beam oscilloscope and calculate the magnitude of the impedance from the peak-to-peak values of measured voltages. Also the phase angle could be observed from the horizontal distance of the peaks.

Impedance magnitude and phase information can be presented with a single beam oscilloscope by the method of Lissajous figures (Barsaukov & MacDonald 2005). In this method the measured current and voltage are presented with an ellipse and the

impedance can be calculated from the dimensions of the ellipse. The Lissajous figure is presented in **Figure 2.4**.

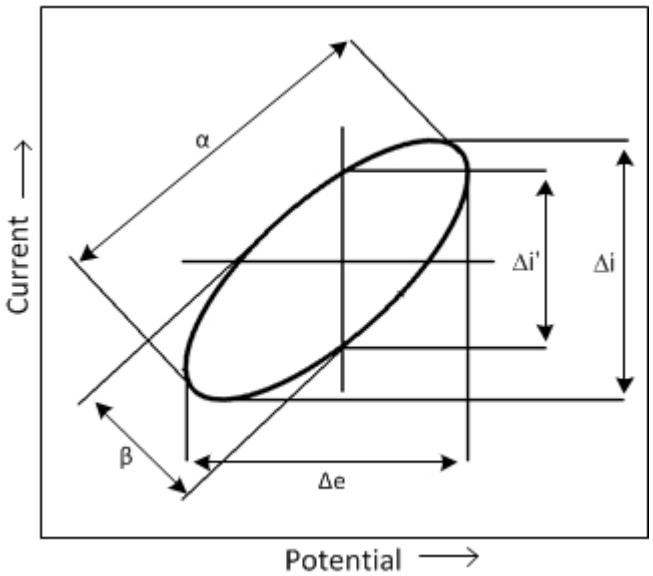

Figure 2.4: *Lissajous figure and dimensions needed in impedance evaluation (redrawn from Barsaukov & MacDonald 2005).*

The magnitude and phase angle of the impedance can be evaluated as

$$|Z| = \frac{\Delta e}{\Delta i} \tag{7}$$

$$sin(\theta) = \frac{\Delta i'}{\Delta i} = \frac{\alpha\beta}{\Delta i \Delta e} \tag{8}$$

Low precision and oscilloscope linearity in order of 1% make this method prone to error. With an oscilloscope the impedance magnitude can usually be measured with an uncertainty of 3%. Phase angle can rarely be measured with a higher precision than 2 degrees. The low end of the frequency band is usually limited to about 10^{-2} Hz due to available oscilloscope storage. Limitations in the high frequency end are primarily imposed by stray capacitances and transmission line effects of the leads. Frequencies above 10^5 Hz are usually tolerable. (Barsaukov & MacDonald 2005)

Another analog method to measure impedance is to use ac coupled bridge. The general principle is shown in **Figure 2.5**.

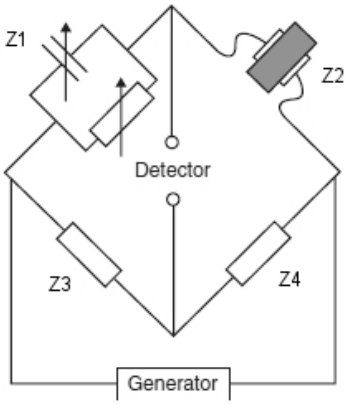

Figure 2.5: *Impedance measurement with an AC bridge (modified from Grimnes & Martinsen 2008).*

The bridge is balanced by adjusting Z_1 so that the signal at the detector is zero. The unknown impedance Z_2 can now be calculated from

$$Z_1 Z_4 = Z_2 Z_3 \tag{9}$$

By using AC coupled bridges with precisely known impedances the unknown impedance can be measured with high resolution. This feature is extremely important with low frequency tissue measurements. Impedance can be measured with an AC coupled bridge from 10 Hz up to MHz region. (Grimnes & Martinsen 2008)

2.2.2 Sine Correlation

The techniques used in bioimpedance measurement have changed enormously with the advent of digital computers. Automated computing has enabled the process of inserting a single frequency perturbation and calculating the response to be repeated in such a manner that a frequency response is obtained in a relatively short time. These devices are known as frequency response analyzers (FRAs) and they have been used by a number of experimenters and impedance researchers for the last three decades. Typically FRAs utilize single-sine or multi-sine correlation methods to measure the impedance. A general schematic of a transfer function analyser using the single-sine analysis is shown in **Figure 2.6**.

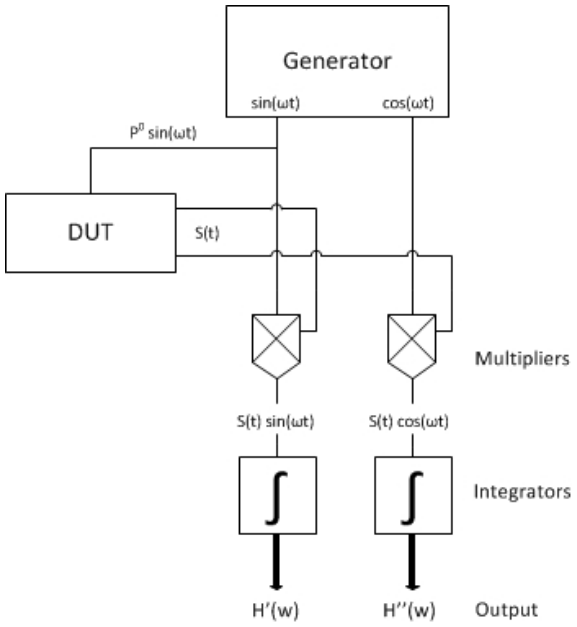

Figure 2.6: *Transfer function analysis schematic (modified from Barsaukov & MacDonald 2005).*

The sine wave perturbation applied by the generator to the device or system under test (DUT) can be presented as

$$P(t) = P^0 \sin(\omega t) \tag{10}$$

where P^0 is the amplitude and ω is the frequency. The response *S(t)* is given by

$$S(t) = P^0|Z(\omega)|sin[\omega t + \phi(\omega)] + \sum_m A_m sin(m\omega t - \phi_m) + N(t) \tag{11}$$

where $\left|Z(\omega)e^{j\phi(\omega)}\right|$ is the transfer function of the DUT and the first right hand term the fundamental component of the response. Nonlinearities in the excited system will create *m* harmonics and measurement environment noise (typically from the power lines) will couple to the response. These are presented by the second and third right hand terms. Next the response is multiplied by reference waveforms, that is, the original sine wave and the 90 degree phase shifted. The real and imaginary components of the impedance are given by equations 6 and 7

$$H'(\omega) = \frac{1}{T}\int_0^T S\,(t)sin(\omega t)dt \tag{12}$$

$$H''(\omega) = \frac{1}{T}\int_0^T S\,(t)cos(\omega t)dt \tag{13}$$

These equations can be extended by using eq. 5. Thus we obtain

$$H'(\omega) = P^0|Z(\omega)| \int_0^T sin[\omega t + \phi(\omega)]sin(\omega t)dt + \frac{1}{T}\int_0^T \sum_m A_m sin(m\omega t - \phi_m)sin(\tau t)dt + \frac{1}{T}\int_0^T N(t)sin(\omega t)dt \quad (14)$$

$$H''(\omega) = P^0|Z(\omega)| \int_0^T sin[\omega t + \phi(\omega)]cos(\omega t)dt + \frac{1}{T}\int_0^T \sum_m A_m sin(m\omega t - \phi_m)cos(\tau t)dt + \frac{1}{T}\int_0^T N(t)cos(\omega t)dt \quad (15)$$

Presuming the noise is completely random, the last integrals are equal to zero if the integration is carried over infinite number of perturbations. In practise the integration is carried over N_f perturbations and the equivalent filter of frequency Δf is given by (Gabrielli 1984)

$$\Delta f = f_1/N_f \quad (16)$$

where f_1 is the center frequency in hertz. The transfer function corresponding this is given by

$$|H(\omega)| = \frac{2}{\pi N}\left[\frac{1}{1-(\omega/\omega_0)^2}\right] sin(N\pi\omega/\omega_0) \quad (17)$$

where ω/ω^2 is normalized angular frequency. The value of transfer function plotted against normalized frequency is shown in **Figure 2.7**.

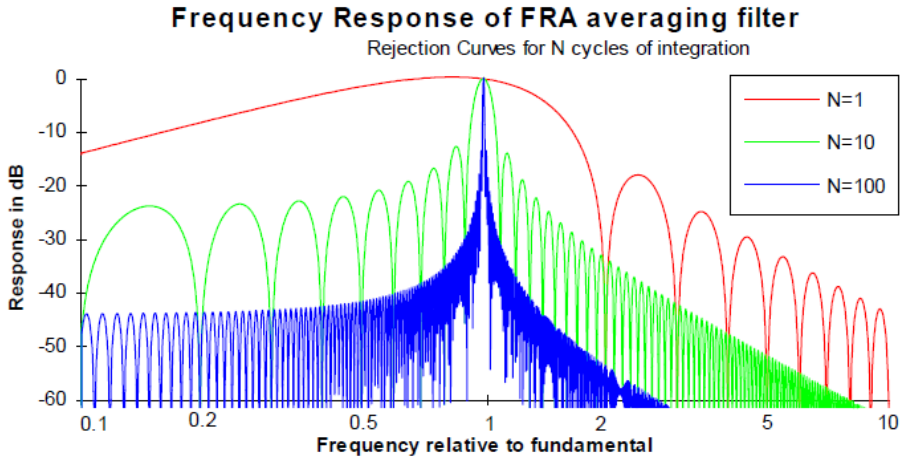

Figure 2.7: *The effect of integration cycles on the bandwidth of the response (Solartron Analytical 1998).*

Equations 14 and 15 still contain the harmonics and the may be expanded to read

$$\int_0^T sin(m\omega t - \phi_m)sin(\omega t)dt =$$
$$cos(\phi_m)\int_0^T sin(\omega t)sin(m\omega t)dt - sin(\phi_m)\int_0^T sin(\omega t)cos(m\omega t)dt \quad (18)$$

$$\int_0^T sin(m\omega t - \phi_m)cos(\omega t)dt =$$
$$cos(\phi_m)\int_0^T cos(\omega t)sin(m\omega t)dt - sin(\phi_m)\int_0^T cos(\omega t)cos(m\omega t)dt \quad (19)$$

Right hand integrals obey the following

$$\int_0^{k\pi T} sin(nx)sin(mx)dx = \begin{cases} 0\ if\ m,n\ integers, m \neq n \\ \frac{k\pi}{2} if\ m,n\ integers, m = n \end{cases} \quad (20)$$

$$\int_0^{k\pi T} sin(nx)cos(mx)dx = \begin{cases} 0\ if\ m,n\ integers, m+n\ even \\ \frac{2k\pi}{(m^2-m^2)} if\ m,n\ integers, m = n \end{cases} \quad (21)$$

If the integrals in equations 14 and 15 are carried over multiples of 2π the integrals involving the harmonics are identically equal to zero. This is how FRAs reject harmonics. With the harmonics and noise eliminated the real and imaginary outputs from the integrators of figure 2.4 are given as

$$H'(\omega) = P|Z(\omega)|cos[\phi(\omega)] \quad (22)$$

$$H''(\omega) = P|Z(\omega)|sin[\phi(\omega)] \quad (23)$$

By using a high number of integration cycles very accurate measurements with wide bandwidths can be done by using a frequency response analyzer. For example Solartron 1260 (Solartron Analytical, UK) has a measurement range from 10 μHz to 32 MHz. However with a growing number of integration cycles the acquisition time also increases considerably. One measurement cycle usually takes several minutes (Roinila et al. 2009a). As a result the method is not best suited for accurate on-line measurements of dynamic systems. (Barsaukov& MacDonald 2005)

2.2.3 Pulse Excitation Methods

Pulse-like wideband excitation signal enables fast impedance spectroscopy on dynamic systems. Frequency swept pulsatile excitations have been implemented successfully in radar and sonar techniques, seismological and optical studies, etc. (Müller & Masarani 2001; Misaridi & Jensen 2005; Barsaukov & MacDonald 2005).

This chapter presents two pulse excitation methods, the chirp signal and the maximum length binary sequence (MLBS). The chirp signal as the excitation in impedance spectroscopy measurements has been studied extensively by Min et al. The method is presented here for comparative purposes and to illustrate the challenges that pulse excitations have with high frequencies and energy content, whereas the MLBS excitation method will be used with the front-end electronics.

Chirp signal

The simplest wideband excitation signal is a half cycle rectangular pulse (Pliquet, Gersing and Pliquett 2000).The energy content of this simplified pulse excitation on the bandwidth of interest is, however, low. For example a unipolar rectangular pulse with duration of 10µs only has a useful bandwidth of 44 kHz. Only 65% of generated energy falls on the bandwidth of interest and root mean square (RMS) spectral density is effectively zero at 100 kHz. (Min et al. 2011) This example is shown in **Figure 2.8**.

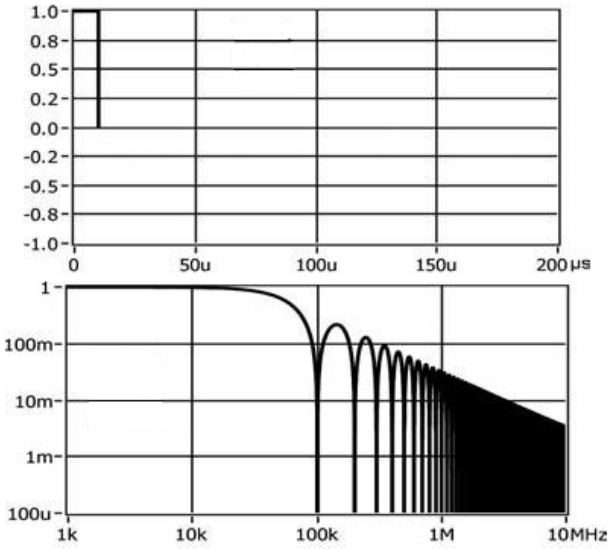

Figure 2.8. *Unipolar 10µs rectangular pulse and corresponding density of RMS spectra (modified from Min et al. 2011a).*

By using a chirp signal the generated energy can be concentrated more efficiently on the bandwidth (BW) of interest. The chirp signal is a signal with increasing or decreasing frequency content (up-chirp or down-chirp). The change of the frequency is typically linear or exponential and the waveform of the chirp is based on sine-wave or rectangular wave (Paavle et al. 2011). A sine chirp pulse comparable to the rectangular

pulse presented in **Figure 2.8** is seen in **Figure 2.9**. This chirp excitation pulse can described as

$$V_{ch}(t) = \sin[2\pi(2BW/T) \cdot t_2/t] \tag{24}$$

where $0 < t \leq T_{exc}$ and duration $T_{exc} = T/2$ of the chirp pulse is the same as half-cycle of sine wave. The inner parentheses contain the chirp rate BW/T_{exc} that corresponds to the excitation bandwidth of 100 kHz. This is covered by the chirp pulse spectrum during one half-cycle $T/2$ = 10 µs of sine function that is equation 24. In **Figure 2.9** about 80% of generated energy lies on the desired frequency band. Also the -3 dB RMS level is located at 100 kHz.

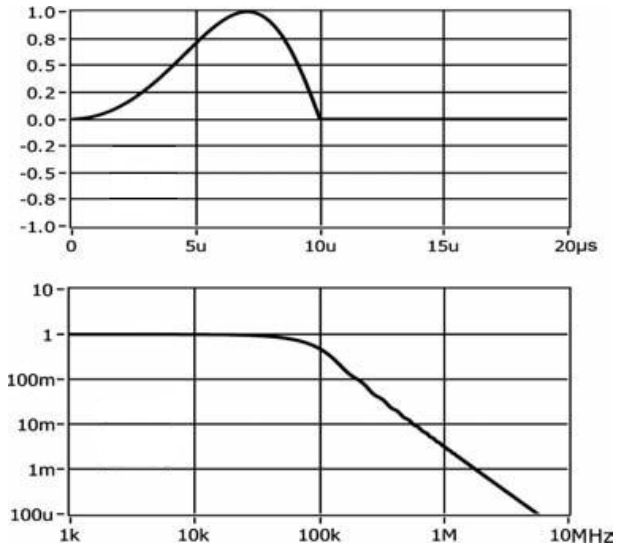

Figure 2.9. *Chirp pulse comparable to unipolar rectangular pulse and corresponding RMS spectral density (modified from Min et al. 2011a)*

Measurement system by Trebbels et al. (2010) utilizing chirp as excitation signal is shown in **Figure 2.10**. First the voltage signal V_{ch} from the generator is converted by the V/I block to excitation current I_{exc}. This excitation current is used to stimulate the unknown impedance $\dot{Z}_z$ and a known reference impedance $\dot{Z}_r$. The both response signals V_z and V_r are then Fourier transformed and a complex division of signals is done. With some additional signal processing the ratio of amplitude spectra and the difference between both phase spectra is obtained.

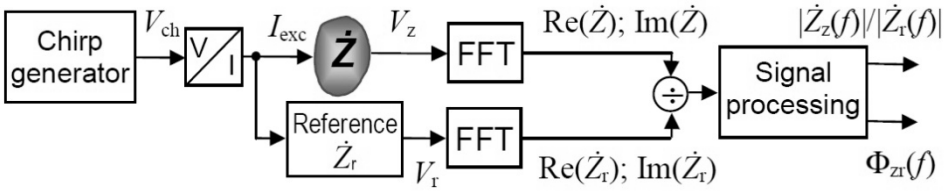

Figure 2.10. *Impedance measurement system using chirp as the excitation pulse. (Min et al. 2011b)*

Design of a short chirp pulse has two opposite goals: in order to avoid significant impedance changes the pulse needs to be as short as possible. On the other hand the longer the signal is the more energy is used to excitation and thus better signal-to-noise ratio (SNR) is achieved. Double scalability gives additional degrees of freedom in designing the excitation. This means that measurement time and bandwidth can be adjusted almost independently (Min et al. 2011a).

The main advantages of chirps are the low power consumption and fast measurement. The first is the most important in implantable devices while the latter is highly needed in high throughput biological measurements, for example microfluidic applications. However the generation of a high quality sine wave chirp requires complicated hardware (Paavle et al. 2008) but researchers are coming up with low-cost solutions to generate the chirp pulse (Paavle et al. 2011).

Maximum Length Pseudo-random Binary Sequence

The impedance spectrum can also be measured in short time by using easily generated binary broad-band excitation signals such as pseudo-random binary sequences (PRBS) and appropriate correlation methods of which the cross-correlation is a widely studied nonparametric system identification method (Roinila et al. 2009b). Nonparametric means that the method makes no assumptions concerning the possible model (Ljung 1987). Correlation method has been used for example to assess the frequency response of digitally controlled power converters (Miao et al. 2004), switched-mode power supplies (Roinila et al. 2009b) and the impedance spectrum of a single biological cell in suspension (Sun et al. 2007). Also acoustics have been studied using maximum length sequences (Shanin & Valyaev 2011).

The impulse response of a linear time-invariant system is the complete characterization of the system (Ljung 1987). The time domain response can be transformed to frequency domain and presented as frequency response function (FRF). A typical FRF measurement arrangement is shown in **Figure 2.11**. The excitation signal *u(t)* is generated by the signal generator, then filtered and amplified. This processing is shown as transfer function *N(s)*. *x(t)* is used to perturb the DUT presented by transfer function *G(s)*. As a result the corresponding output response *y(t)* is obtained. Excitation and response are measured and these measurements are contaminated by noise. The measured excitation and output are denoted as $x_e(t)$ and $y_t(t)$.

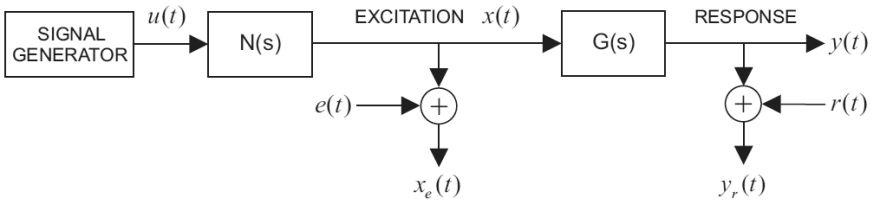

Figure 2.11. *Frequency response function measurement setup (Roinila et al. 2009a).*

The system FRF $G(j\omega)$ can be expressed as

$$G(j\omega) = \frac{Y(j\omega)}{X(j\omega)} \tag{25}$$

where $X(j\omega)$ and $Y(j\omega)$ are Fourier transformed input and output spectra of the corresponding signals $x(t)$ and $y(t)$. With measurement noise $e(t)$ and $r(t)$added to the excitation the measured FRF $G_m(j\omega)$can be denoted by

$$G_m(j\omega) = \frac{Y_r(j\omega)}{X_e(j\omega)} \tag{26}$$

where $X_e(j\omega)$ and $Y_r(j\omega)$are the Fourier transforms of the measured signals $x_e(t)$ and $y_r(t)$. Denoting the error signals with their Fourier transforms $E(j\omega)$ and $R(j\omega)$, the measured FRF becomes

$$G_m(j\omega) = G(j\omega)\frac{1+[R(j\omega)/Y(j\omega)]}{1+[E(j\omega)/X(j\omega)]}. \tag{27}$$

If the SNR is low at the input or output the measured FRF may deviate a lot from the actual system FRF. By using the spectral presentations of auto- and cross-correlation functions the white noise at the input and output can be minimized. White noise is an uncorrelated signal with a flat spectrum over the whole bandwidth under study. If we assume the input $x_e(t)$ is ideal then the cross-correlation function according to (25) can be given as

$$G(j\omega) = \frac{\sum_{k=1}^{N} Y_{rk}(j\omega)X_{ek}^*(j\omega)}{\sum_{k=1}^{N} X_{ek}(j\omega)X_{ek}^*(j\omega)} \tag{28}$$

where N is the number of averaged measurements and the asterisk denotes complex conjugate. This equation minimizes the uncorrelated noise at the output but ignores the noise at the input. This assumption is valid however since the input was presumed ideal. With an excitation that resembles white noise the cross-correlation neglects external errors that do not correlate with the measurements. (Miao 2004; Roinila et al. 2009c)

Maximum length binary sequence has similar spectral properties as true random white noise. MLBS $\{a_k\}$ satisfies the linear recurrence

$$a_k = \sum_{j=i}^{n} c_i\, a_{k-i} (mod\ 2) \tag{29}$$

where c_i has a value of 1 or 0 and a_k has a period of $P = 2^n$-1 (Golomb 1967). With appropriate choice of c_i the sequence has maximum length. MLSB can be generated using an n bit shift register with exclusive or (XOR) feedback. The process is shown in **Fig-**

ure 2.12. By mapping the values 0 and 1 generated by the process to +1 and -1 the maximum length sequence signal $\{x_k\}$ is symmetrical with mean close to zero.

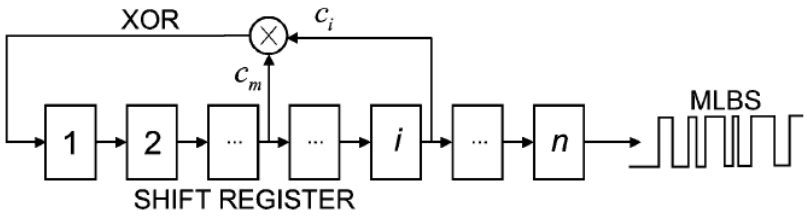

Figure 2.12: *Generation of MLBS excitation signal with n-bit shift register. (Roinila et al. 2009a)*

Since the generated sequence is deterministic it can be reproduced precisely. This makes it possible to synchronously average the response periods and thus increase the SNR.MLBS method assumes that the process under consideration is linear. According to Grimnes and Martinsen (2008, p. 130) every biomaterial can be considered linear with sufficiently small excitation energies. However nonlinearities are often present in in-vitro measurements due to electrolyte/electrode system used (ibid). To minimize the effects of nonlinearities an inverse-repeat binary sequence (IRS) is proposed. The IRS is generated by doubling the MLBS and toggling every other digit of the doubled sequence. (Roinila et al. 2009a)

2.3 Epithelial tissue

The four tissue types found in human body are connective tissue with fat as a type of connective tissue, muscle tissue, nervous tissue and epithelial tissue. Of the four classic tissue types, the epithelial cells are the most prolific. Epithelial tissue can be characterized by its structure and cell shape. Structure can be simple, where epithelium consists of a single layer of cells, or it can be stratified, which signifies an epithelium consisting of two or more layers. Shape of cells can be flat, *squamous*, box-shaped, *cuboidal*, or columnar. There are no blood vessels in epithelium.

Epithelial tissue has several functions in the body. Epithelial cells line the cavities in the body and create a boundary between the body and the environment. Much of the sensory information is registered by the epithelium tissue for example in the nose and the eye. In addition to protecting organs and tissues, epithelium sustains the homeostasis and produces hormones and secretions that control the different functions of the body. Epithelial tissue that is specialized to produce and secrete different substances is called glandular epithelium. These glands can be further divided into exocrine and endocrine glands depending on their secretion method. Another more specialized type of epithelium is transitional, which is found in the urinary tract and is able to vary in shape when stretched. (Haug et al. 1999; Laitala-Leinonen 2004; King 2010)

2.3.1 Electric Properties of Epithelium

All organs in the body are surrounded by epithelia. Cells in epithelia form gap junctions and particularly in tight membranes these junctions are special tight junctions (TJ). These junctions between the cells have very low DC conductance. Measured DC conductivity is therefore very dependent on what sorts of epithelia and lipid bilayers the current has to cross. (Grimnes & Martinsen 2008)

The inverse of DC conductivity of epithelium is referred to as transepithelial resistance (TER). This parameter is used extensively to assess the confluence of cell layers. In practise TER is not measured with DC current as this leads to electrode polarization (ibid) but with a low frequency AC current. These frequencies typically range between 2 Hz and 20 Hz (Günzel et al. 2012). TER measurement results include the sum of the resistances of all current impeding components between the recording electrodes. These include epithelial cells and subepithelial tissues. In cell culturing the filter supports and bath solution medium resistances are added to the measurement result.

TER measurements provide sufficient information on the level of tightness of the epithelium in many applications like monitoring of cell growth and cell layer formation during culture. TER measurements do not however provide conclusive information on the structure of the epithelium and especially on the tight junctions for reasons mentioned above. As cell membranes act as capacitors the impedance measurements reveal much more information about the electrical properties and structure of the epithelium than TER measurements. (ibid).

Since the epithelium actively regulates ion flow through it with ion channels, transporters and ion pumps, this creates an imbalance of ions across the epithelium. The net movement of negative and positive ions from the apical side to the basolateral side generates a potential. This potential is equal to the potential difference between the apical membrane and the basolateral membrane and it is known as transepithelial potential (TEP). (Li et al. 2004; Onnela et al 2012) This potential varies in different parts of the body. For example Dubé et al. (2010) measured TEPs between 10 and 60 mV from normal human epidermis whereas Maminishkis et al. (2006) and Quinn and Miller (1992) measured potentials below 4 mV from adult and fetal RPE. As with TER measurements the integrity of the sample has a strong effect on the measured TEP values (Savolainen 2011).

Apical surfaces of many epithelial layers are covered with microvilli. Examples of these are the RPE and the epithelium covered mucous membrane of small intestine. The microvilli increase the surface of the epithelium and thus improve important functions like absorption and secretion. From the perspective of electrophysiology the microvilli functions as a capacitive element. The loss or absence of microvilli in epithelium is seen as lowered capacitance values (Bertrand et al. 1998; nanoAnalytics 2012b).

2.3.2 Equivalent Circuit Models of Epithelium

There exist two approaches to build an electrical model of epithelium, descriptive and explanatory. Descriptive models reflect primarily the phenomena, that is, the measured values and time courses. The microanatomy of the epithelium is not necessarily imposed on the model nor do the components of the model exist as physiological processes. Explanatory models are built using the basic concepts of electrical theory and these models include only discrete electrical components unlike descriptive models that may include for example constant phase elements that do not exist in practise. In explanatory models the components represent physical processes and anatomical structures. Accurate modelling of physiological processes with discrete electrical components results in highly complex structures where the heuristic analogy to electronic components is lost. However explanatory models can be useful for representing the frequency response at one single frequency. (Grimnes & Martinsen 2008)

An electrical model that is an electrical equivalent produces the same frequency response as the actual measured response by impedance spectroscopy. Thus it is more of a descriptive model than an explanatory model. In epithelial monolayers the current has several paths; these are illustrated in **Figure 2.13**. These intra- and paracellular current paths have been modelled with varying degrees of complexity in equivalent circuits over the past decades.

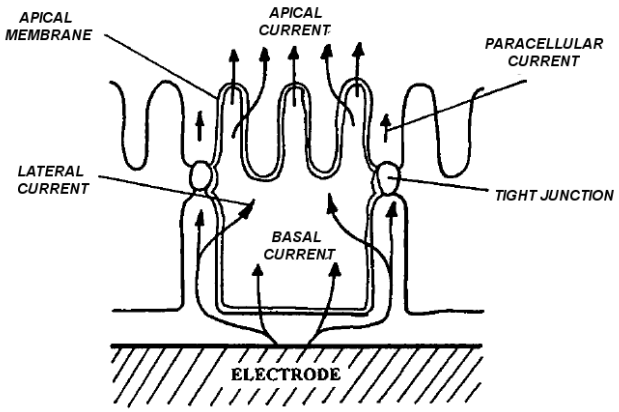

Figure 2.13. *Epithelial cell monolayer in tissue culture and the various current paths. (Lo et al. 1995)*

The simplest lumped model represents epithelia with three parameters: an epithelial capacitance C_{epi}, an epithelial resistance R_{epi} and a subepithelial resistance R_{sub}. This type of simplified model can be determined by impedance spectroscopy measurements. Since no distinction is made between intracellular and paracellular current pathways this is referred by Günzel et al. (2012) and Krug et al. (2009) as "one-path impedance spectroscopy". The impedance $Z_{eq}$of the equivalent circuit can be expressed as

$$Z_{eq} = R_{\text{sub}} + \frac{R_{\text{epi}} \cdot \left(1 - j \cdot \omega \cdot R_{\text{epi}} \cdot C_{\text{epi}}\right)}{1 + \left(\omega \cdot R_{\text{epi}} \cdot C_{\text{epi}}\right)^2} \tag{30}$$

where ω is the angular frequency determined as $2\pi f$ with f being the frequency under study.

To reflect the paracellular current pathways the resistance R_{epi} can be replaced by two resistors in parallel. Paracellular resistance is now presented with R_{para}. Although this model offers more information about the flux of predominant ions, that is, Na^+ and Cl^-, moving along the paracellular space, it requires more complex instrumentation than "one-path impedance spectroscopy". For example Schifferdecker et al. (1978) impaled microelectrodes into epithelial cells to determine R_{para} and R_{trans} whereas Gitter et al. (1997a) employed "conductance scanning" method. Also a marker substance, more precisely an ionic form of fluorescein, has been used in determination of R_{para} (Günzel et al. 2012). These measurements with the assumption of separate current pathways are called "two-path impedance spectroscopy" by Günzel et al. (ibid) and Krug et al. (2009). With auxiliary measurements the model can be further improved by presenting the apical and basolateral membranes as two parallel RC circuits in series (Lewis and Diamond 1976). The presented equivalent circuits are shown in **Figure 2.14**.

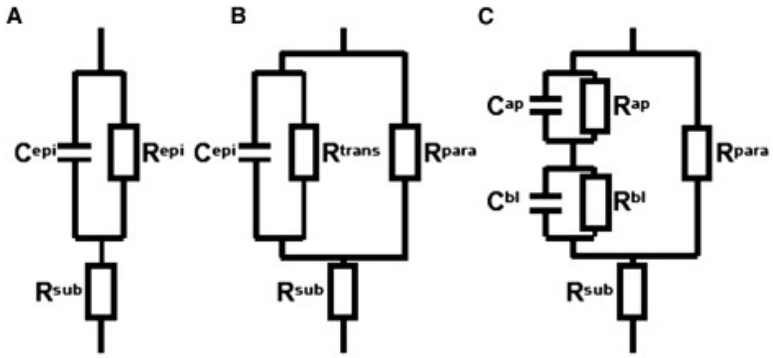

Figure 2.14. *Equivalent electrical circuits for epithelium impedance measurements. Circuit A shows the one path model and circuits B and C the two path model. Circuit C is similar to B except that it has apical and basolateral membranes presented as separate elements (Krug et al. 2009).*

The circuits presented in **Figure 2.14** are commonly known as lumped models. These models present incorrectly the paracellular resistance R_{para} where the resistance is formed by the tight junction and a long narrow space such as the lateral intercellular space (LIS). Clausen et al. (1979) proposed a distributed model of an epithelium that has distributed resistance in series with the lateral but not the basal portion of basolateral membrane. This distributed resistance impedes current flow at high frequencies but not at low frequencies. As a result the lumped model seriously underestimates the basolateral capacitance (ibid). The LIS and the distributed resistance model are shown in **Figure 2.15**.

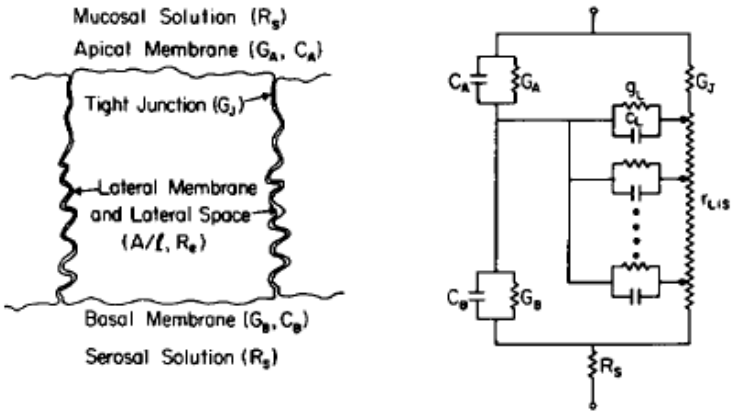

Figure 2.15. *Left: Epithelium monolayer with long and narrow LIS. Right: The equivalent circuit of the distributed resistance model. The resistances are shown as conductance, inverse of resistance. (modified from Clausen et al. 1979)*

More complex models require auxiliary measurements in order to solve the mathematical relations. Additional measurements may also not be suitable for the measurements of dynamic systems or they may cause damage to the cell membrane structure. (Bertrand et al. 1998)

2.3.3 Frequency Response of Epithelium

The frequency response of epithelium can be used to determine all the components of the simplest one-path equivalent circuit of epithelium. The response is typically measured with a range of frequencies between 1 Hz and 100 kHz. (Günzel et al. 2012)

Figure 2.16 shows the shape of frequency responses typical to epithelium measurements. The level of the higher plateau is equal to the transepithelial resistance as the excitation current flows through resistance R_{epi} instead of capacitance C_{epi} at low frequencies. As higher frequencies are inserted the capacitance presents a lower impedance current path and as a result the level of impedance at high frequencies is determined solely by the resistance R_{sub}.

The change in the level of impedance takes place at a frequency determined by the parallel RC circuit. R_{epi} and C_{epi} form a low pass filter with a specific time constant τ. This time constant can be expressed as a simple product of capacitance and resistance with a unit of second. This is the time required to charge and discharge the capacitor through the resistor to about 63% of the final or initial value. If the capacitance of the epithelium is low, this charging and recharging takes place at high frequencies and a flat response is measured at the frequencies of interest.

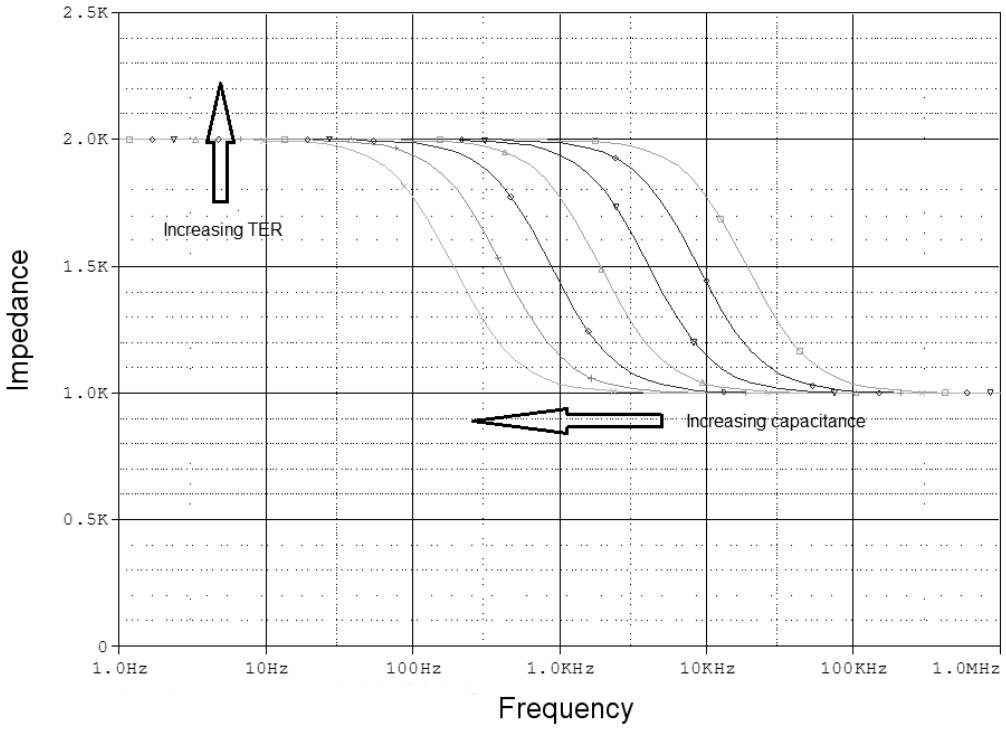

Figure 2.16. *The frequency responses of one-path equivalent circuit where both the resistances* R_{epi} *and* R_{sub} *are 1 kilo-ohm and the capacitance* C_{epi} *varies between 1 µF and 10 nF.*

2.4 In vitro Measurements of Tissues

In this chapter the basic experimental setup used in membrane or cell layer measurements is introduced. The setup has however several significant sources of measurement errors due to non-ideal current pathways and the material or placement of electrodes. These sources of error are presented with some examples of measurement difficulties encountered using commercial voltage measurement devices. The chapter ends with the presentation of Ussing Chamber, a measurement setup that overcomes many of the sources of measurement errors recognized in this chapter.

The basic membrane experiment is done by dividing a volume filled with electrolyte into two compartments by a membrane. Each of the compartments contains two electrodes: one for carrying current and the other for voltage pick-up. This makes the total number of electrodes four. This type of arrangement is shown in **Figure 2.17** where a voltage *v* is used to generate excitation current *i*. This current flows through the membrane and gives rise to electric potential difference *Δv* measured by the inner voltage electrode pair.

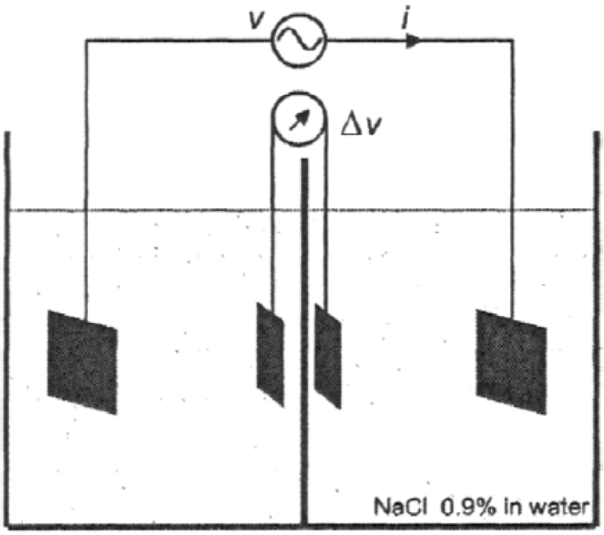

Figure 2.17. *Basic membrane experiment with saline solution as electrolyte. (Grimnes & Martinsen 2008)*

As the voltage electrodes are connected to buffer amplifiers with high input impedances virtually no current flows through the electrodes. This four-electrode system ideally eliminates the influence from external electrode polarization and it is the most suitable electrode setup for *in vitro* measurements. (Grimnes & Martinsen 2008)

2.4.1 Measurement Errors

The measurement errors present in in vitro impedance measurements can be divided into three categories depending on their origin: the electronics used to excite the object under study and measure the induced voltage, the measurement environment, and the measurement setup.

In this chapter the focus is on the electronics and the measurement setup. Electrode polarization in particular is strongly dependent on the current injection circuitry and on the material and placement of electrodes.

Electrode Polarization

If the input impedances of the buffer amplifiers are not large enough or the voltage sensing circuitry offers another low impedance pathway for the current, current will flow through the voltage pick-up electrodes and the electrodes will polarize. This polarization will result in polarization impedance in series with the sample and too high impedance levels are recorded. Schwan (1992) presented this impedance Z_p as a series combination of resistance R_p and capacitance C_p. Due to the series circuit the polarization impedance may become a significant problem at lower frequencies.

$$Z_p = R_p - j/\omega C_p \tag{31}$$

Also the positioning of recording electrodes may cause them to polarize if they are placed along the current path. The current will prefer the high conductivity path whenever possible and this causes current to enter the recording electrode at one point and exit in another. This is shown in **Figure 2.18**.

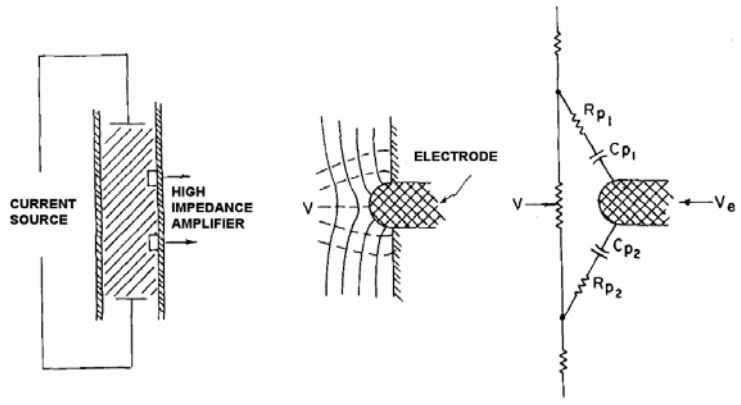

***Figure 2.18**. Polarization of a non-recessed recording electrode. Polarization impedances Z_{p1} and Z_{p2} will lift the electrode to a wrong potential and the error voltage V_e is measured instead of the actual voltage V. (modified from Schwan 1992)*

Polarization due to current entering and exiting the electrode can be avoided by recessing the electrodes, in other words by placing them farther away from the current

path or by removing the sensing electrode area from the sample. One example of removing the sensing electrode area from the sample is to use a salt bridge.

DC Current Flow in Ag/AgCl electrodes

Ag/AgCl electrodes are often considered the best choice for electrodes in applications of biology and medicine where DC current carrying is needed. Typically these electrodes consist of silver covered with AgCl layer and when carrying current the polarization impedances of these electrodes are smaller compared to other electrode materials like stainless steel or platinum. (Grimnes & Martinsen 2008)

If Ag/AgCl electrodes carry DC current for prolonged time the thickness of silver chloride coating changes and this affects the electrode impedance. If the current carrying electrode is anode the layer thickness will increase gradually as will the impedance of the electrode. This depositing of chloride ions is observed as If the electrode is a cathode the covering layer is slowly diminished until only a pure silver surface remains. This silver electrode has much larger polarization impedance and different equilibrium potential than Ag/AgCl electrode. (ibid)

Equilibrium DC Potential

Electrode-electrolyte interface

The transform from electronic to ionic conduction takes place at the electrode-electrolyte interface. This transition zone has a non-uniform distribution of charges and as a result a double layer is formed. The exchange of charges takes place in this layer and creates a DC potential on the electrode. A concept of half-cell is used to evaluate this potential (Grimnes & Martinsen 2008). Since a potential always needs a reference we can only observe potentials consisting of two half-cells, that is, a pair of electrodes or an electrolytic cell.

Under zero current flow between the electrodes, inert noble metals like platinum are preferred as voltage measurement electrodes as an inert metal experiences no electrode metal ion transfer. In other words the oxidation and reduction reactions (known as redox) taking place at the interface balance each other out. The redox equilibrium potential V for an electrolytic cell with no DC current flow can be estimated with Nernst equation

$$V = V_0 + \left(\frac{RT}{nF}\right) ln\left(\frac{\propto_{ox}}{\propto_{red}}\right) \tag{32}$$

where V_0 is the material specific standard half-cell potential of the redox system, n the number of electrons in the unit reaction, R the universal gas constant and F the Faraday constant. α_{ox} and α_{red} are activities that are dependent on specific ion concentrations. If

however electrodes do carry current, polarization takes place in noble metal electrodes and the output voltage is noisy. In presence of a current flow electrode materials with low polarizability like Ag/AgCl should be chosen. (ibid)

The DC potentials in tissue culture research are often measured with battery operated handheld devices using chopsticks resembling electrodes. These commercial applications do however recommend shorting the electrodes together and soaking of chopsticks for at least two hours prior to measurements in order to stabilize the electrode DC potentials (Millipore 2012, World Precision Instruments 2012). Since the electrodes are held by the operator during the measurements the results may vary according to the depth and angle of the placement of the electrodes. A proper placement of electrodes using the well structure as a sample setup is shown in **Figure 2.19**.

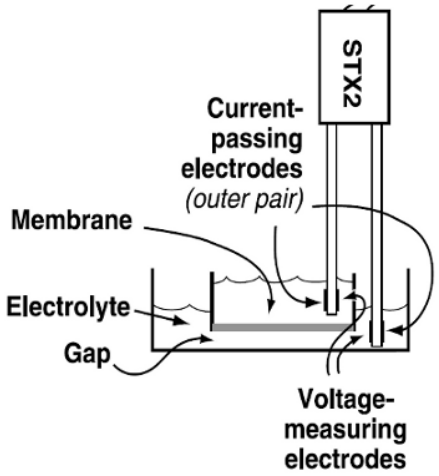

Figure 2.19. *DC potential measurement using the handheld electrodes. The tissue sample would be located in the inner well above the porous membrane. (modified from World Precision Instruments 2012)*

There are commercial applications that enhance the reproducibility of measurement results by automating the procedure of electrode placement or have rigid electrodes and the sample well is inserted into the measurement chamber (ibid). A better accuracy and repeatability of results comes with the price of exerting the cultured cells to mechanical stress each time a measurement is needed. A closed chamber also makes any kind of drug permeability tests more difficult to conduct.

Electrolyte-electrolyte interface

Just as at the electrode-electrolyte interface a potential difference is created also at the interface of two dissimilar electrolyte solutions. This liquid junction potential Φ_{ij} can be determined with an equation similar to Nernst called the Henderson equation

$$\Phi_{ij} = \frac{\mu^+ - \mu^-}{\mu^+ + \mu^-} \frac{RT}{nF} ln \frac{c_1}{c_2} \tag{33}$$

where R is the universal gas constant, c_1 and c_2 concentrations of the liquid junction and μ+ and μ- are the mobilities of cations and anions, respectively. By choosing ions with similar mobilities the junction potential is minimized.

In in vitro measurements it may be desirable to physically separate the electrode-electrolyte interface from the tissue. This can be done by inserting a salt bridge between the solutions. Typically strong KCl electrolyte is used but the choice ultimately depends on the effect different cations have on the sample. The salt solution may be immobilized with agar gel to ensure the strong electrolyte does not reach the sample. The salt bridge creates two junctions instead of one but with opposite signs so they more or less cancel each other. (Grimnes & Martinsen 2008)

2.4.2 Ussing Chamber

Transepithelial electrical measurements have been done extensively with a device known as Ussing chamber. It is commonly used to measure the net ion transport taking place across the membrane, impedance and capacitance. The device is divided into two functional halves. One is the actual chamber where the tissue sample is located while the other contains the electrical circuitry. This way the electrodes are recessed and thus electrode polarization is minimal. Also the electrodes typically use salt bridges to physically isolate the electrodes from the sample.

Two types of Ussing chambers currently exist: the circulating chamber and the continuously perfused chamber. **Figure 2.20** shows the circulating chamber where the solution is circulated in the chambers. The U-shaped tubing secures an equal hydrostatic pressure on each sides of the chamber and damage to the tissue due to bending can be avoided. The tubing can be heated if necessary and the solution gassed with air or gases such as CO_2, O_2 or N_2. The gassing oxygenates the liquid contents and ensures complete convection by stirring the liquid. In perfusion experiments a drug is typically added to one side in a sequential manner. Due to the circulating nature of the chamber the added substances cannot be removed during the experiment. (Li et al. 2004)

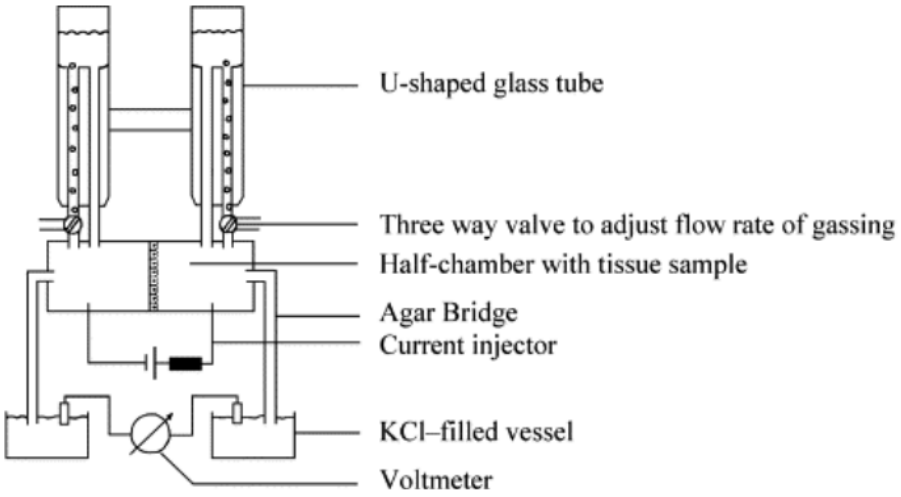

Figure 2.20. *Basic circulating chamber (Li et al. 2004)*

The continuously perfused chamber has two bathing solution reservoirs mounted 20-50 cm above the chamber. The solution is delivered to the chamber via tubes and the flow is regulated with valves. The temperature of the solution can be controlled by means of water jacket heating system. (Li et al. 2004)

The circulating solution in Ussing chamber experiments is typically Ringer's solution. This solution has the same concentration of salts and pH as the bodily fluids of an animal or a human. For example the Ringer's solution used by Gitter et al. (1997b) contained (in mM) 140 Na^+, 5.4 K^+, 1.2 Ca_2^+, 1.2 Mg_2^+, 123.8 Cl^-, 21 HCO_3^-, 2.4 HPO_4^{2-} and 0.6 $H2PO_4^-$ (gassed with 95% O_2 and 5% CO_2; pH 7.4 at 37°C).

2.5 Commercial Applications of Impedance Spectroscopy

There is a variety of devices available on the market for electrochemical impedance spectroscopy. Most of the devices presented here use single-sine or multi-sine excitations to measure the frequency response. Typically modulation and demodulation is used to achieve multi-sine excitation signals. A large number of devices offer a module for FRA and suitable software for the analysis of impedance data. The time taken by an individual frequency response measurement is presented if given by the respective manufacturer.

Solartron 1260A (Solartron Analytical, UK) is widely used by researchers due to high accuracy of the device gained from the single sine sweep technique. Frequency sweep from 10 Hz to 1 MHz with 10 points per decade takes around 2 minutes. Thus the device is more suitable for measurements of time-invariant systems. Impedance interface module increases the measurement range considerably. (Solartron analytical 2011)

Modulab-MTS (Solartron Analytical, UK) with MFRA module utilizes single-sine and multi-sine excitations with FFT operations. Frequency sweep from 10 Hz to 1 MHz with 10 points per decade can be measured in five seconds with accuracy comparable to 1260A (Solartron analytical 2011b).

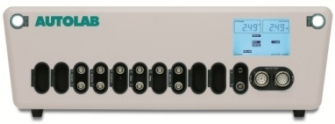

PGSTAT302N (Metrohm, Netherlands) with FRA32M module allows the user to perform potentiostatic and galvanostatic impedance measurements with up to four electrodes. The device uses single-sine and multi-sines to excite the object under study. The total measurement time for a frequency range of 0.1 Hz – 100 kHz is around 10 minutes (Metrohm AG 2012).

HF2IS Impedance Spectroscope (Zurich Instruments, Germany) can measure the frequency response with up to 8 frequencies (with Multi-frequency module) at once in addition to single-sine sweep technique. High sample rate makes the device suitable for microfluidics applications like label free analysis. (Zurich Instruments 2012a)

cellZscope (nanoAnalytics, Germany) measures the impedance of cell culture inserts with permeable membranes by using two electrodes. The device is designed for studying the influence of different substances on the permeability of cell layers (nanoAnalytics 2012a). TER and capacitance of the cell layer can also be measured in addition to the impedance spectrum. A frequency sweep from 10 Hz to 100 kHz with 5 points per decade takes around 5 seconds to complete (Schäfer 2012).

RTCA series (ACEA Biosciences Inc., USA) is designed for long term drug testing. It focuses on measuring the proliferation and viability of cells cultured on top of electrodes. The system output is dimensionless parameter called Cell Index that corresponds to the number of cells, level of adhesion, cell morphology etc. (ACEA Biosciences 2011)

AD5933 and **AD5934**(Analog Devices, USA) offer two terminal impedance converter network analyzer in one integrated circuit (IC). The IC operates with floating load principle and the excitation is applied on specific bias voltage. A device using one of these ICs needs external circuitry however and frequency sweep parameters have to be programmed externally. (Analog Devices 2012).

The commercial FRAs presented above are listed in table 2.1. Also cellZscope is present although the manufacturer does not supply any information on the excitation method. Also the measurement times listed in table 2.1 are all dependent of the sweep parameters like number of integration cycles, amount of averaging etc.

Table 2.1. *Commercial frequency response analyzers with the most relevant parameters. A dash notes a parameter not supplied by the manufacturer.*

	Solartron 1260	**Modulab-MTS**	**PGSTAT302N**	**HF2IS**+ MF module	**cellZscope**
Excitation method	SS	SS, MS	SS, MS	MS	–
Freq. range (Hz)	10µ - 32M	10µ - 1M	10µ - 1M	1µ - 50M	1 – 1 M
Meas. Time	2 min	5 sec	10 min*	♮	5 sec**
Accuracy (% / °)	0.1 / 0.1	0.1 / 0.1	0.2 / –	–	–
# terminals	Up to 4	Up to 4	Up to 4	Up to 4	♯

SS: Single-Sine
MS: Multi-Sine
Measurement time: Time taken to measure the frequency response from 10Hz to 1 MHz with 10 points per decade.
♮ Depends heavily on the sweep parameters (Zurich Instruments 2012b)
♯ Electrodes designed for cell culture measurements
*From 0.1 Hz to 100 kHz
** 5 points per decade

2.6 Electronic design

This chapter introduces the theoretical concepts used in the design of the impedance measurement device. As stated in the previous chapter the impedance spectrum is typically derived from the measured voltage with the assumption of near ideal excitation. This is particularly true with MLBS excitation. As result the most important design aspects in impedance spectroscopy system that utilizes a pulsatile excitation is to ensure the injection of precise wideband current and the accurate measurement of the induced voltage over the load. Thus most attention in this chapter is paid to the design of current injection, **Chapter 2.6.1**, and voltage sensing, **Chapter 2.6.2**.

Another important aspect of electronics design is noise coupling and grounding. Wideband excitation and measurement set limits to filtering the noise by traditional methods like passive filters. To minimize the coupling of noise the use of high-speed, high-linearity analog optocouplers is examined in **Chapter 2.6.3**.

The accurate measurement of DC potentials and the requirements set by electrodes are studied in **Chapter 2.6.4**. Also the filtering needed for DC measurements is discussed here.

2.6.1 Current Injection

When there is direct electrolytic contact between tissue and electrodes, the constant-current circuit is most conveniently employed (Geddes 1968). Typical constant current impedance measurement device contains a voltage controlled current source (VCCS), in other words a transconductance amplifier. This amplifier is generally realised in electrical impedance spectroscopy (EIS) and tomography (EIT) by using one of two approaches, the grounded load current source such as a Howland circuit (Wang et al 2007; Pliquett et al. 2011) or the floating load (also known as *load-in-loop*) current source (Bragos et al. 1994; Annus et al. 2008; Hong et al. 2008; Seoane et al. 2011).

An ideal current source in **Figure 2.21** outputs a current i_O independent of the impedances Z_e of the combined electrode-electrolyte-interfaces and electrode polarization impedances, and load impedance Z_L. In short the ideal transconductance amplifier has infinite output impedance Z_O. In other words the current source can drive constant current no matter what electrode setup is used or how large the load is. However a practical current source has finite output impedance and this results in weakened independence of i_O on Z_L and Z_e.

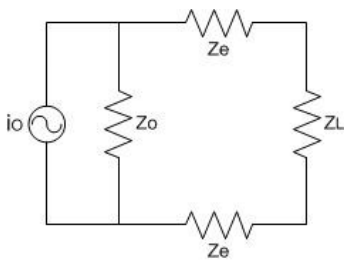

Figure 2.21. *Non-ideal current source with finite output impedance.*

The analysis presented above can be derived for an ideal floating load converter. In floating load topology the load is used as the feedback element. With low to moderate excitation currents the amplifier is used to drive current instead of the voltage source. The circuit is shown in **Figure 2.22**. Here the resistor R_{set} is used to set the current to desired level according to equation (25). More systematic analysis of the load-in-loop current source circuit configuration based on the transfer function approach is presented in Annus et al. (2008).

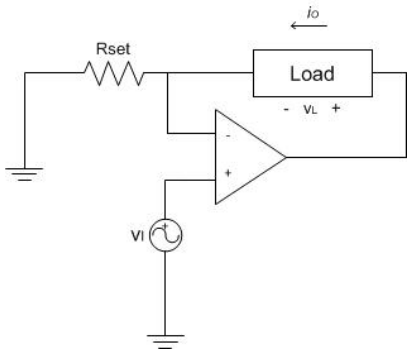

Figure 2.22. *Floating load transconductance amplifier.*

$$i_{\mathrm{O}} = \frac{1}{R_{\mathrm{set}}} v_{\mathrm{I}} \tag{34}$$

One method to increase the output impedance of a current source is to use a Generalized Impedance Converter (GIC). These converters simulate positive or negative impedances depending on the specific structure. Studies show however that GIC is useful when operating with frequencies higher than 1 kHz up to several megahertz. If lower frequencies are under study and the load impedance is expected to be around 1 kilo-ohm or greater, the bandwidth of the GIC may prove to be problematic. Also constructing a wide-band GIC requires trimming in order to avoid negative output impedance that can lead to instability. (Wang et al. 2007)

DC currents

In impedance measurements the DC currents flowing through the electrodes and load are minimized in order to avoid polarization of the materials (Grimnes & Martinsen 2008). All practical operational amplifiers have however non-zero input offset voltages due to the non-identical transistors at the input stage. This dc voltage is also seen at the output and it causes dc current to flow to the load. According to Vuorela (2011, p. 77) this can be overcome in the floating load current source by using a feedback loop to eliminate the input offset voltage. The current feeding amplifier is shown in **Figure 2.23**.

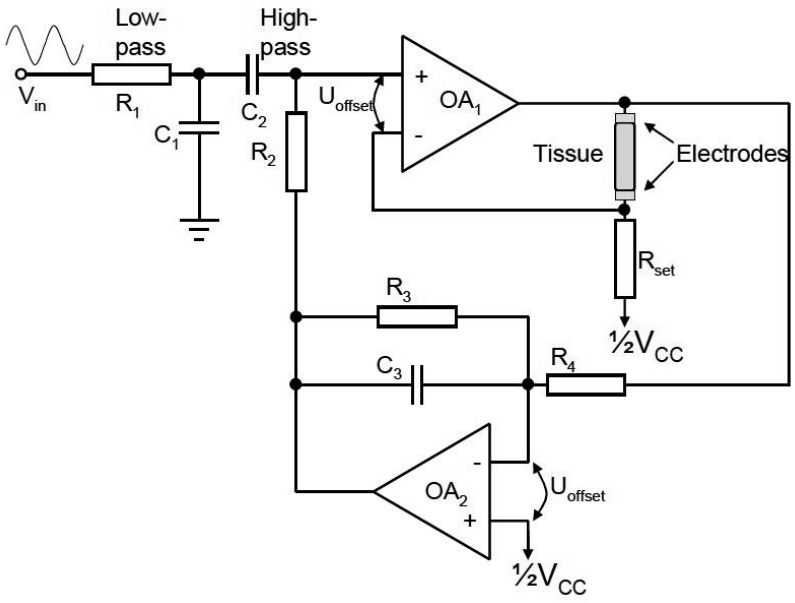

Figure 2.23. *Floating load current injection amplifier with feedback loop for eliminating the DC currents to the load (Vuorela 2011).*

Here the operational amplifier *OA1* forms a floating load transconductance amplifier with the load (electrodes and tissue) and resistor R_{set}. By connecting R_{set} to half of the supply voltage V_{CC} the circuit can operate with a single supply voltage. Low-pass and high-pass filters are used to narrow the band of excitation signal to the desired frequencies. Any possible DC-component of the excitation signal is thus filtered out effectively. The input offset voltage U_{offset} of $OA_1$is normally added to the output. This voltage can be negative or positive depending on the specific component's input stage. By feeding the output of OA_1 to the negative input of OA_2 and comparing this to the reference voltage ½ V_{CC}, the offset voltage is inverted and summed to the excitation signal through resistor R_2. This inverted voltage is amplified by the ratio of resistors R_3 and R_4.

Since OA_2 acts as an active low-pass filter only low frequency components are fed to OA_1. The cut-off frequency of the low-pass filter should be close to dc although this requires a relatively large capacitor for C_3. However if the feedback loop contains frequencies of interest this can create instability due to the positive feedback structure.

With a sufficiently low cut-off frequency of the active low-pass filter the feedback cycle eventually stabilizes and output of OA_1 without excitation is very close to reference voltage ½ V_{CC}. Some error to the output voltage is caused by the input bias current of OA_1 and input offset voltage of OA_2. This error can however be minimized by keeping the resistances of R_3 and R_4 moderate and by choosing amplifiers with low input offset voltages and input bias currents.

2.6.2 Voltage Sensing

Current from VCCS flowing through the load induces a potential difference over the load. The measurement environment can be noisy however or the load can float upon a certain dc potential. By using a difference amplifier only the differential potential is

amplified. An ideal difference amplifier has infinite input impedances, zero output impedance and it does not amplify any common mode signals. In other words it has infinite common mode rejection ratio (CMRR). A lone practical difference amplifier loads the signal source as the differential and common mode input impedances are finite. Also CMRR remains low. This can be overcome by adding two operational amplifiers as buffers. The resulting circuit is known as instrumentation amplifier (IA).

True differential stage requires accurate trimming of resistors. If a CMRR of 80 dB is required the resistors should have no larger difference than 0,003% (Franco 2002). This can be difficult to achieve by manual trimming. In addition the resistances vary according to ambient temperature. Monolithic IAs contain the buffer amplifiers with the difference amplifier in a single chip. Laser trimming of resistors and close placement of amplifiers ensure high CMRR and high input impedances as well as low output impedance. The gain can be usually set with one resistor or as a ratio of two resistors.

Instrumentation amplifier can also be built using only two amplifiers. These are called dual operational amplifier IAs. The benefit of the design is the low cost of the chip due to smaller amount of components, but CMRR of the dual operation amplifier IA is generally lower than in corresponding IA using three operational amplifiers. The lowered CMRR results from the uneven signal pathways at the input of the IA. (ibid.)

When IAs are used to measure wideband signals attention should be paid to CMRR and gain-bandwidth product (GBP). Noise occupying the frequency band of interest that couples to measurement system cannot be simply filtered out without complex compensation circuits. Also amplification of the measured signal should be as large as possible since the following gain stages will also amplify the noise remaining in the signal.

2.6.3 Optocoupling

Galvanic isolation of the patient from the mains is required in all bioimpedance devices. Although this is due to patient safety it can also be useful in in-vitro measurements where ground loops and the galvanic coupling of power line noise decrease the SNR of the measurement system. This has been traditionally done with capacitors and transformers but the major drawback of these approaches is that they cannot transmit dc signals without noisy modulation and demodulation process (Borges et al. 2010; Simoes et al. 1995).

Modern linear analog optocouplers offer a relatively simple and low-cost solution to couple high-speed analog signals with low nonlinearity. An optocoupler consists of a light emitting diode (LED), usually called *servo*, located behind a transparent isolating gap and two photosensitive diodes on the other side of the gap at equal distances from the LED. This way the photodiodes receive the same amount of light. The principle is shown in **Figure 2.24**.

By using PD1 as linearizing feedback diode a high linearity is achieved. This feedback also compensates the temperature drift typical to diodes.

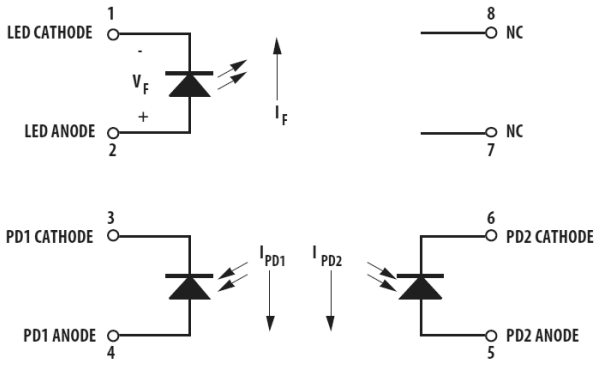

Figure 2.24. *Optocoupler servo diode and two photodiodes. Photodiode 1 (PD1) is on the input side while photodiode 2 (PD2) is the output (Avago Technologies 2011).*

An optocoupler circuit can be operated in two modes depending on the application needs. For low offset drift and high linearity the photovoltaic mode should be used where the LED is driven with forward bias. If maximum bandwidth is important then the servo should be driven in reverse bias mode. This is called photoconductive mode. (Vishay Semiconductors 2011)

In forward bias operation mode a current I_F flows through the LED. Light flux created by LED creates photocurrents I_{PD1} and I_{PD2}. The ratios of these currents define largely the circuitry needed for the isolation amplifier utilizing an optocoupler. The servo gain *K1*, output forward gain *K*2 and transfer gain *K3* are defined as

$$K1 = \frac{I_{PD1}}{I_F} \tag{35}$$

$$K2 = \frac{I_{PD2}}{I_F} \tag{36}$$

$$K3 = \frac{K2}{K1} \tag{37}$$

These gains are typically specified by manufacturers for narrow operating conditions. By choosing a transfer gain near unity the design process is simplified, especially if bipolar operation is required. Also attention should be paid to the operation amplifiers at the input and output stages. These amplifiers add noise and have effect on the bandwidth of the system thus possibly degrading the linearity of the optocoupling (ibid).

2.6.4 DC Potential Measurement

The DC level measurement can be done with the instrumentation amplifier circuit discussed in Chapter 2.6.2 but the electrodes do set certain challenges to this method. First, each electrode-electrolyte interface has a certain offset potential that can drift with time. When sensing the potential over the cell layer the offset potentials of voltage measurement electrodes are added to the TEP of the sample and the sensed voltage does not represent the desired TEP. This significant source of error can be minimized by adding an offset adjustment circuit for the DC potential measurement circuit.

As stated in Chapter 2.2 the electrode offset potential can vary greatly depending on the material of electrode and of the electrode-electrolyte interface (liquid-liquid vs. metal-liquid). This makes the selection of offset compensation range non-trivial and it should be ultimately decided upon the choice of electrodes.

A simple offset compensation circuit consists of a potentiometer and a buffer amplifier connected to the difference or instrumentation amplifier's negative input. **Figure 2.25** shows this compensation circuit.

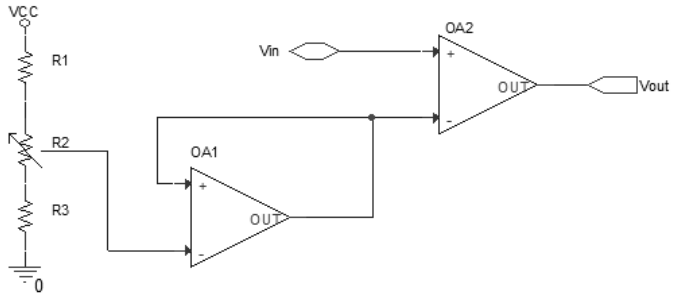

Figure 2.25. *Offset compensation circuit. If* V_{in} *is presumed to be superimposed on ½* V_{CC} *the resistances* R_1 *and* R_2 *should be equal. They are also used to set the maximum current flowing through the voltage divider whereas the compensation voltage range is determined by the ratio of the potentiometer and a current setting resistor.*

AC components of the signal should be filtered from V_{in} if the DC level is to be amplified by a large gain. This can be done with a first order low pass filter by applying only passive components. If however heavier filtering is required an active second order low pass filter with a sufficiently low cut-off frequency can prove to be useful. An active second order low pass filter with unity gain is shown in **Figure 2.26**.

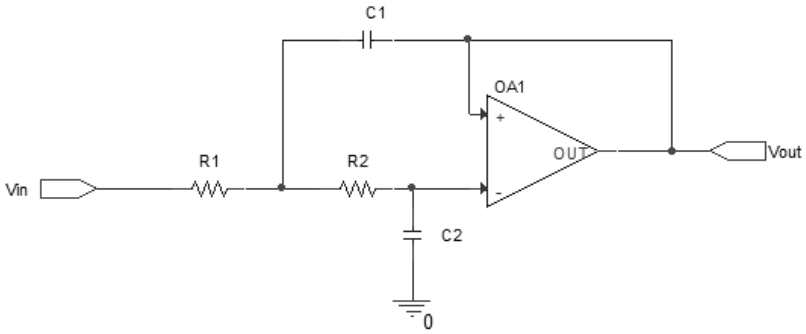

Figure 2.26. *Active second order low pass filter with unity gain.*

3 METHODS

This chapter presents how the study was conducted. **Chapter 3.1** presents how the theoretical background presented earlier was applied for the component selection. Emphasis of the subchapter is on the choice of the instrumentation and operational amplifiers. **Chapter 3.2** presents the circuit used in the simulation of the effects of large polarization impedances.

The actual measurement system used in the impedance measurements is presented in **Chapter 3.3.** The chapter begins with the presentation of the back-end of the measurement system where the excitation signal is designed. This is followed by the high-speed data acquisition system (DAQ). The chapter ends with the introduction of assembled front-end electronics. The chapter end presents the three sample setups, the testing box, the Ussing chamber and the well plate. Also the artificial membranes and the cell lines used in the impedance measurements are introduced here in detail.

The final **Chapter 3.4** clarifies the difference between the measurements conducted during this study and actual epithelial layer frequency response measurements. Also the equipment and the procedures used for obtaining the reference results are explained thoroughly.

3.1 Component Selection

This chapter presents the most important components used in the impedance measurement device. First the needs of input and output signal optocoupling are examined and the choice is made between two high speed analog optocouplers. After this the amplifier that will be used in the current injection block is selected. The same component is also chosen as the general purpose amplifier for the device.

Finally the selection principles for the instrumentation amplifier are presented with a consideration of possible challenges encountered using the component. A complete list of components used in the impedance measurement device is given in **Appendix 2**.

3.1.1 Optocouplers

In choosing the optocoupler the following qualities were required of the component: high linearity, wide bandwidth and low power consumption. One component to fulfil these requirements was the widely used IL300 from Vishay Semiconductors. The optocoupler had 0.01 % servo linearity with a 200 kHz bandwidth. Most importantly the

component was readily available from the large catalogue suppliers and also extensive literature could be found of the possible applications of the component.

Another component fulfilling the set requirements was found from Avago Technologies. A high linearity Optocoupler HCNR200 employed the same principle as Vishay's IL300 with the same amount of linearity but instead offered a bandwidth of 1 MHz. The availability of the components and application literature ultimately lead to choosing IL300 as the optocoupler for the galvanic isolation of the input and output.

3.1.2 Operational amplifiers

The choice for the operational amplifiers used in this thesis was guided by the demands of the current injection circuit. As stated in **Chapter 2.6.1** the feedback structure required low input bias currents and input offset voltages for the offset DC level at the current output to stabilize close to ½ V_{CC}. Also the bandwidth of the amplifier would have to exceed the requirements of the excitation signal by at least a decade.

A precision operational amplifier, AD8616, by Analog Devices was selected after a careful review for the general amplifier for the front-end electronics. This amplifier had a bandwidth over 20 MHz, almost as low input bias currents as INA331, 1pA, and a remarkably low offset voltage, 23 µV. The amplifier was also suitable for use as a photodiode preamplifier or as an active filter and the moderate power consumption of 2 mA made the component an excellent choice for a general purpose amplifier to be used in the measurement device.

3.1.3 Instrumentation amplifiers

A survey on different instrumentation amplifiers showed very few components with wide enough bandwidths and high CMRR. The manufacturers examined were Analog Devices, National Semiconductor/Texas Instruments and Linear Technology. When the requirements for single supply and rail-to-rail operation, low supply current and a gain set with resistors were used as the selection criteria the choice for the amplifier narrowed down to INA331 by Texas Instruments.

The component has a bandwidth of 2 MHz which exceeds the requirements of the application almost by a decade. The component is also designed to be used in battery operated devices and as a result has low quiescent power consumption. The requirement for low input bias current is also satisfied as the amplifier needs a bias current of only 0.5 pA. The bias current flows through the input bias resistors that are typically relatively large and thus can have resistance variation in order of several tens of kilo-ohms. This difference of resistances gives rise to an offset error voltage according to Ohm's law and this is why low input bias currents are essential for the instrumentation amplifiers used in this theses.

One major shortcoming of the component is that it uses the dual amplifier structure and has a relatively low CMRR especially at high frequencies. This was taken into account upon layout design by keeping the routing of inputs as identical as possible.

Also the component was only available in MSOP package with a pitch of 0.65 mm, a pitch size not optimal for soldering by hand. INA331 was used in the front-end electronics as the instrumentation amplifier for sensing the voltage induced by the excitation current and also in a role of difference amplifier in the DC potential gain stage with offset adjustment.

3.1.4 Other components

Other components that required careful selection were the regulator used for the power supply, the current setting resistor in the floating load circuitry and the voltage detector used in the battery monitoring.

Originally, a DC-DC converter was designed to be used as the power supply of the measurement device but it became soon evident that a lower noise solution was needed. As the device was designed to be battery operated and consume power in order of ten to twenty milliamps a linear regulator was chosen as the power supply solution. Although there was a large voltage drop between the battery and the output of the regulator only small amount of power is wasted in the component due to low current consumption. A typical linear regulator has a much lower noise than DC-DC converter and there are even low noise linear regulators available. A review of these regulators with a requirement of fixed 5V output resulted in choosing LT1763-5 from Linear Technology as the power supply solution for the front-end electronics.

The low drop-out linear regulator LT1763-5 is a micropower, low noise regulator with a low 30µA quiescent current. With the addition of an external 0.01 µF capacitor between the output and bypass pin the output noise becomes as low as 20 μV_{RMS} over a 10 Hz to 100 kHz bandwidth. The component has internal protection circuitry that includes reverse battery protection which is essential in preventing extensive damage to the device upon inserting the battery the wrong way. Because of this there is no need for separate protection diodes. The protection circuitry also includes thermal and current limiting properties.

As with all linear regulators the choice of output capacitor is not trivial and should be chosen with care. The manufacturer states that a low ESR capacitor should be used to avoid oscillation of the output and that maximum ESR should be 3 ohms at most. The recommended 10nF bypass capacitor requires a large output capacitor in order of several microfarads. By choosing a large 10 µF high quality tantalum capacitor with low ESR the stable operation of the linear regulator is ensured.

The floating load current injection circuitry uses a resistor in setting the excitation current amplitude. This resistor needed to be as close to the desired value as possible to minimize the errors in the impedance calculations. For this a precision automotive thin film chip resistor with a tolerance of 0.1 % was chosen from Vishay Thin Film.

The measurement device was designed to include a battery monitor and this was done with a voltage detector. A ready-made chip TC54-5 was found from Microchip that suited well for battery powered applications because of its extremely low 1 µA operating current. The modification of the trip-point was also adjustable with a simple

resistor division and this was particularly useful since the manufacturer offered only trip-points for voltages below 5 V.

3.2 Simulation of the Electrode Impedances

The electrode impedances were simulated as part of this study to assess the most likely sources for errors in measured impedances. The construction of the simulation circuit and the choice for the equivalent circuits for polarization effects are presented here as well as the current pathway for the most probable DC current. The program used in the simulation was OrCAD Capture v.16.5 (Cadence Design Systems, Inc., San Jose, CA, USA).

If an instrumentation amplifier is to be used in in vitro measurements with the four electrode setup the excitation current pathways should be examined in detail. All IA circuits should have a current pathway for input bias currents that are typically in order of few nanoamps. The lack of these input bias current pathways slowly saturates the input stage. However the floating load current source requires that the inputs of the IA have to be biased to the floating potential. Absence of this biasing would result in DC common mode signal level equal to half V_{CC} at the input and this would be seen as saturation of the output. **Figure 3.1** shows the IA connected to a floating load current source.

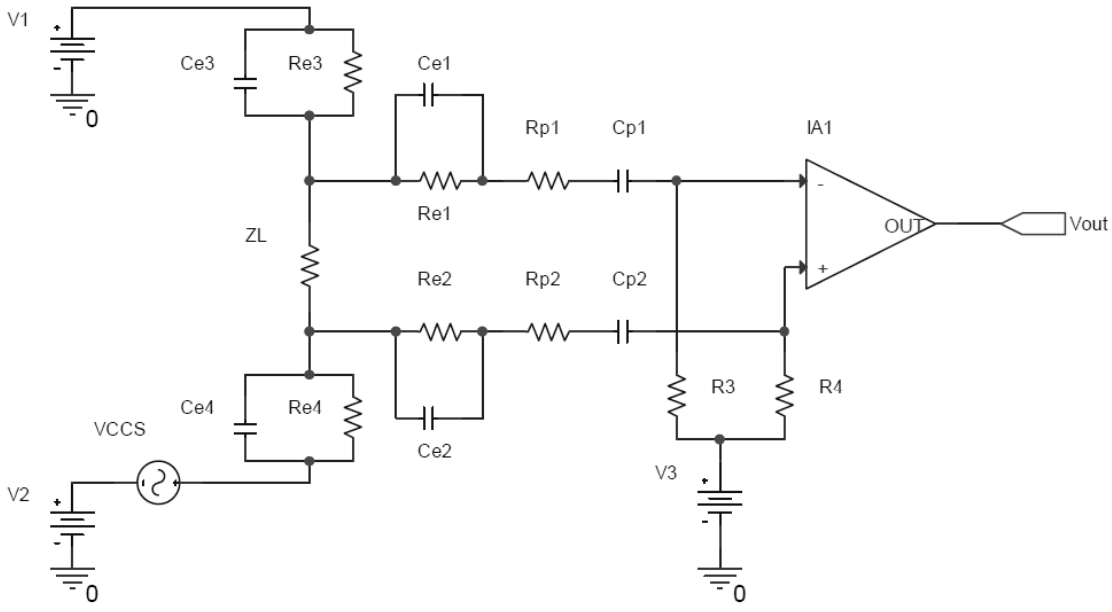

Figure 3.1. *Instrumentation amplifier connected to a floating load. The equivalent circuits for the current injection and voltage measurement electrodes are also included in the figure. The models for the equivalent circuits of the electrodes, parallel* C_e *and* R_e*, are from Schwan et al. (1992).*

The input bias current pathways R_4 and R_5 are of low impedance compared to the input impedances of IA buffer amplifiers. The voltage floating the load (voltage sources V1 and V2) is not exactly the same as the voltage V3 biasing the inputs due to reasons mentioned in **Chapter 2.6.1**. This causes a small amount of DC current to flow through the low impedance pathway of R_3 or R_4 depending on the polarity of the DC

voltage difference. This DC current flows also through the voltage sensing electrodes thus polarizing them in the process. The polarization effect is presented in **Figure 3.1** with two resistors, R_{p1} and R_{p2}, and two capacitors, C_{p1} and C_{p2}.

The increase of the impedance of the voltage sensing electrodes were simulated and the effect on the measured voltage was examined systematically. The simulation results with the exact component values are presented in **Chapter 4.1**.

3.3 Measurement system

This chapter presents the measurement system used in the TEP and the frequency response measurements. The frequency response measurement system consists of a signal processing software running on a portable personal computer, the data acquisition card used to create the excitation signal and sample the recorded voltage and of the front-end electronics used to excite the sample with current pulse and measure the resulting voltage. A block diagram of the applied measurement system is shown in **Figure 3.2**.

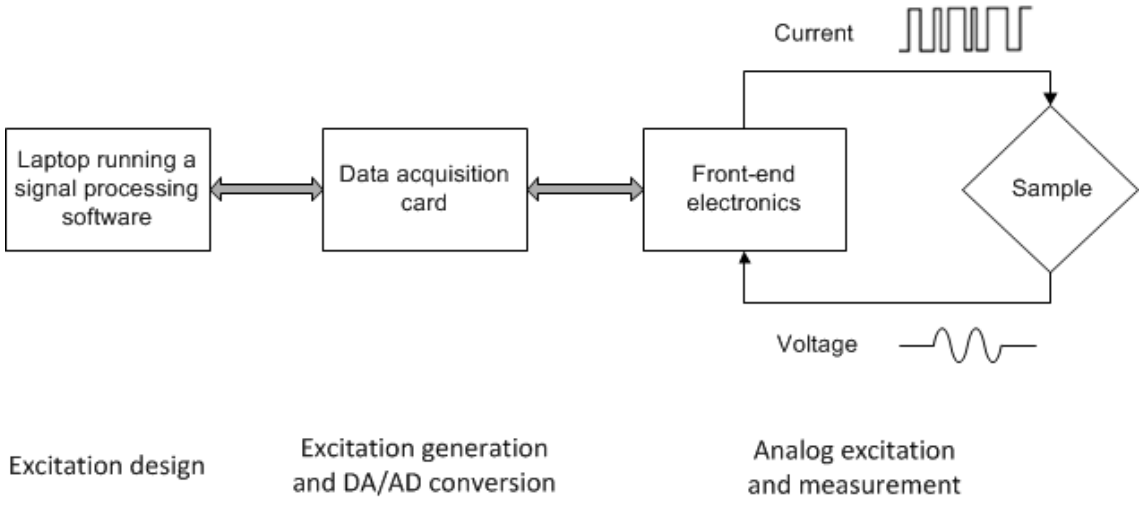

Figure 3.2. *The implemented measurement system.*

3.3.1 Generation of the Excitation Signals

The excitation signals were generated with Matlab version 7.13 (The Mathworks, Inc. Natick, MA, USA). Two scripts were used to generate the excitations: one for covering only the lower frequency band with a high number of data points and the other for covering the same frequency band but with fewer data points.

The first excitation signal was designed on the assumption that the corner frequency of the resulting frequency response would lie between 100 Hz and 1 kHz. This was based on the results gained by Savolainen et al. (2011b). Thus the excitation was designed to cover the frequencies beginning from one decade lower and ending in one decade higher than the aforementioned band. The second excitation was mainly purposed for fast analysis of impedance levels and for the detection of possible electrode polarization (continuously ascending impedance levels). As a result the excitation covered the same frequency band as the first excitation but with lower resolution. Both of the scripts included 30 repetitions of the excitation signal to improve the SNR of the resulting output through averaging.

The scripts used in the measurements are presented in **Appendix 1**. It should be noted however that it was relatively simple to change the frequency band of the excitation although the methods presented here apply to majority of measurements conducted.

3.3.2 Data Acquisition

The excitation signal was created using the data acquisition system USB-6251 BNC (National Instruments, TX, USA) and a signal processing software. Also the output signals of the assembled electronics were recorded using the same system.

The system employs USB connection for easy-to-use signal transmission between the system and a laptop. The DAQ has 8 differential BNC analog inputs with a resolution of 16 bits. Each of these input channels is sampled with 1.25 million samples per second. The system also contains 2 analog outputs with the same resolution as inputs. The maximum sampling rate for the analog outputs is 2.86 million samples per second. The DAQ is compatible with most versions of the Windows operating system. (National Instrument 2008) The DAQ is presented in **Figure 3.3**.

Figure 3.3. *High speed data acquisition system with USB and BNC connections. (National Instruments 2011)*

3.3.3 Implementation of Electronics

Two prototype versions were designed and built of the front end electronics during the thesis. The first version was constructed to see if the floating load principle would work in practice for excitation and measurement and also to get a good understanding of the noise level at the output. Valuable information was also gained with the first version about the shortcomings of the circuit regarding the in vitro electrodes.

The second version employed much of the same design solutions as the first version although the emphasis was on noise reduction. The measurement circuitry for TEP measurement was added to the second version as well as the battery monitor circuitry. The complete schematics of the impedance measurement device are presented in **Appendix 3**.

Test circuit for optocoupling

It was originally agreed that the impedance measurement device should have its inputs and outputs galvanically isolated using high speed analog optocouplers. As stated in **Chapter 3.1.1** IL300 optocouplers were chosen as the component and a test circuit was built to observe how well the bandwidth given by the manufacturer would be achieved.

Upon designing the circuitry for testing the bandwidth of the component it became evident that the photoconductive mode of operation suffers from bias drifting and thus the transmission of accurate DC levels, like TEP results, would be difficult. The circuit shown in **Figure 3.4** is similar to the one built for testing the bandwidth of the optocoupler except for the bipolar junction transistor used to drive the servo. This was left out because the amplifiers used in the circuitry had adequate current output capabilities.

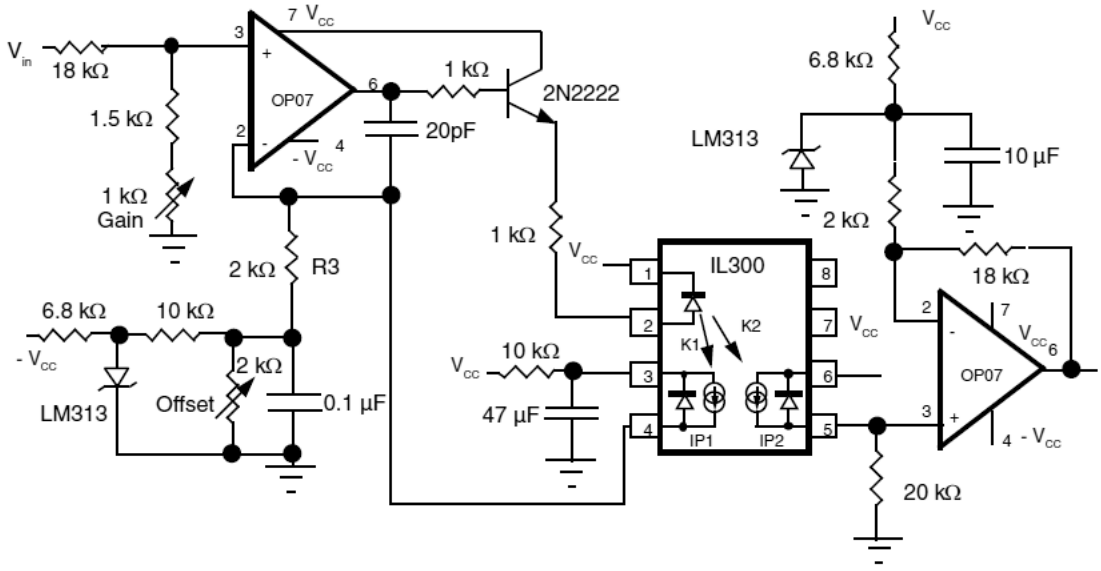

Figure 3.4. *High stability bipolar photoconductive isolation amplifier with non-inverting configuration and unity gain when the transfer gain K3 of the optocoupler close to one. (Vishay Semiconductors 2012)*

The gain of the circuit in **Figure 3.4** can be manually trimmed for unity using the 1 kilo-ohm potentiometer at the input and the photoconductive mode is achieved by reverse biasing the both photodiodes. The layout of the printed circuit board designed for testing the component is shown in **Figure 3.5**. The width of top and bottom layers is 58 mm.

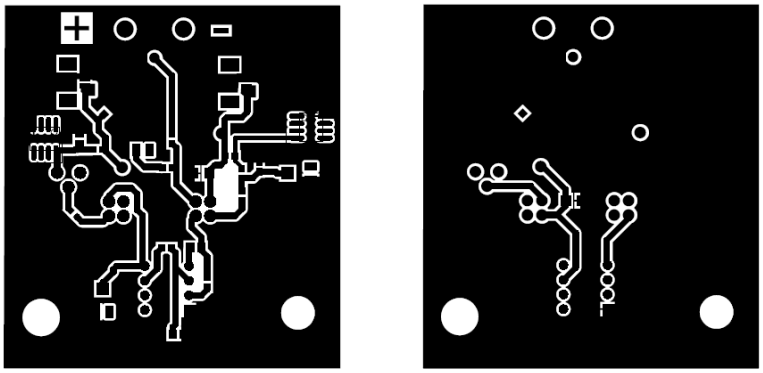

Figure 3.5. *The printed circuit board layouts used in testing the optocoupler. The top layer is shown on the left and the bottom layer on the right.*

The built circuit did not achieve the promised bandwidth and the highest frequency of the input signal to be transferred without distortion remained close to 30 kHz. This may have been due to poor layout design although the frequencies examined remained under 100 kHz. Another reason for the poor performance may have been the smaller current than recommended used to drive the servo LED. The manufacturer recommended 10 mA to be used for driving the servo but this was not feasible however as the final device would include three connectors to galvanically isolate, one for the input and two for the outputs, PRBS signal and TEP level. Thus the total current consumption would have been around 30 mA from the optocoupling alone. Considering the bandwidth problems encountered with optocoupling, the current consumption and the need for dual supplies, the optocoupling was ultimately left out of the first and the second prototypes. This simplified the design considerably and ensured that the excitation signal would suffer from minimal distortions at the input stage. This was one of the most important design aspects of the current injection as the algorithm used in impedance calculations assumed the applied excitation impulse ideal.

Current injection

The both prototypes used basically the same current injection circuitry although the noise and the DC levels were minimized in the second prototype with careful amplifier and power supply selections. The bandwidth of the input was limited in the current injection circuit with two passive filters. First the signal was low pass filtered with a cut off frequency of 624 kHz to filter out high frequency noise. The second filter was high pass filter with a cut off frequency of 0.02 Hz. This was used to filter out any possible DC level in the excitation signal.

The bandwidth of the current injection circuit was simulated with OrCAD Capture and the current injection block presented in **Appendix 3**. The load used in the simulations was the one-path electrical equivalent circuit of epithelium presented in **Chapter 2.3.2** with R_{sub} and R_{epi} as 1 kΩ and C_{epi} as 1µF. Also the current injection electrodes were modelled in a manner presented in **Chapter 3.2**. The simulation results are plotted

as the current *i* flowing through the current setting resistor R_{set} as a function of frequency. This current also flows through the load. The excitation current *i* is shown in **Figure 3.6**. It can be seen that the current stays almost constant with frequencies lower than 100 kHz although trimming is required as the current level is slightly below 10 µA.

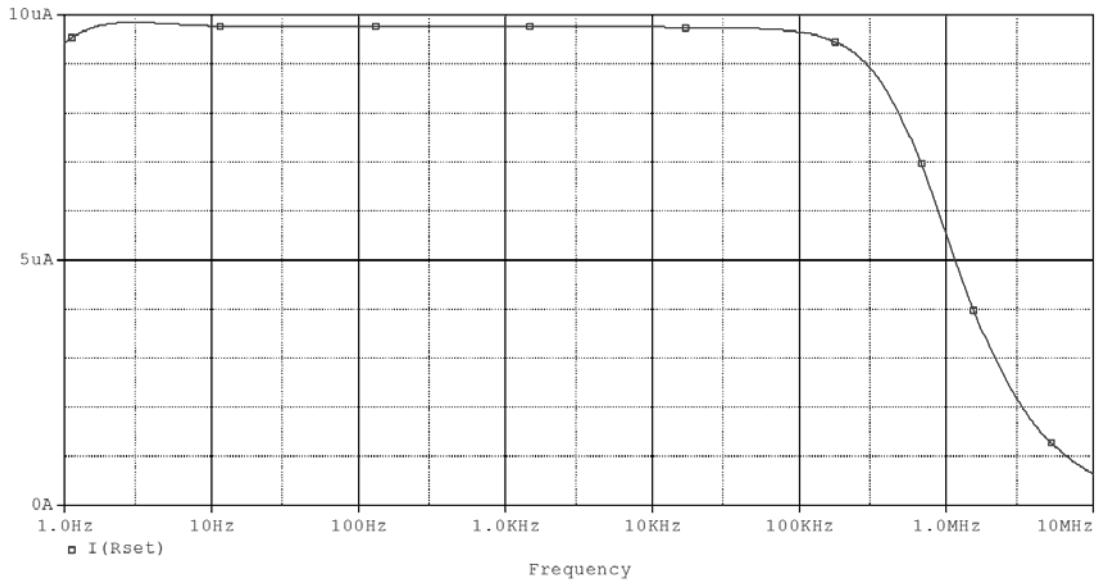

Figure 3.6. *Simulated current injection behavior on the frequencies of interest.*

When the selected AD8616 is used to drive capacitive loads and a unity gain is used, the output exhibits overshoot if there is no compensation. The overshoot was damped by adding 200 ohm resistors and 470 pF capacitors in series with the outputs of both amplifiers used in the current injection circuit. The other ends of the compensation series connections were connected to battery ground.

Voltage Sensing

The device was designed to be battery operated from the beginning due to probable line noise coupling. The operating voltage of the device was selected to be 5 V and this sets certain limits to how large impedances can be measured. Since INA331's output can swing from 0.02 V up to V_{CC} - 0.02 V this gives a dynamic range of 4.96 V for the output. As the current source operates on floating load principle the voltage sensing electrodes have to float also at the same potential. This reduces the dynamic range by half down to 2.48 V. This range must be further divided by the gain of the instrumentation amplifier to solve the maximum measurable load voltage.

Since the peak current that is fed to the load is 10 µA and presuming that all of this current actually flows through the load only, we can solve the theoretical maximum impedance that can be measured with the device

$$\frac{2.48\,V/GAIN_{IA}(30)}{10\;\mu A} \approx 8267\Omega$$

The battery level monitor was designed to warn the user of a failing battery by lighting a red LED. The threshold voltage for the detection was set to 7 V as this was well above the minimum voltage required by the linear regulator but still high enough to supply the current needed by the LED. A ready-made voltage detector component TC45 with a threshold of 4.5 V was used to monitor the battery voltage. The threshold voltage was adjusted with two resistors so that battery voltage of seven volts gave 4.5 V at the detection pin.

BNC connectors were chosen for the inputs and outputs of the device as the DAQ used in the measurements had similar connectors. The current injection and voltage measurements leads were connected with 3.5 mm stereo plugs. The lead shields were connected to the enclosure that floated at battery ground. The final layout of the second prototype is shown in **Figure 3.7**. The final device is shown in **Figure 3.8**.

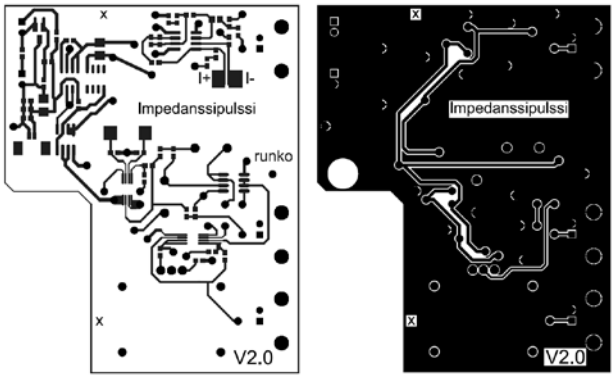

Figure 3.7. *The layout of the second prototype. The top layer is shown on the left and bottom layer on the right. The current injection circuitry is located at the top, power supply at the left and voltage sensing in the middle. The Finnish words on the board are "Impedance pulse" and "chassis".*

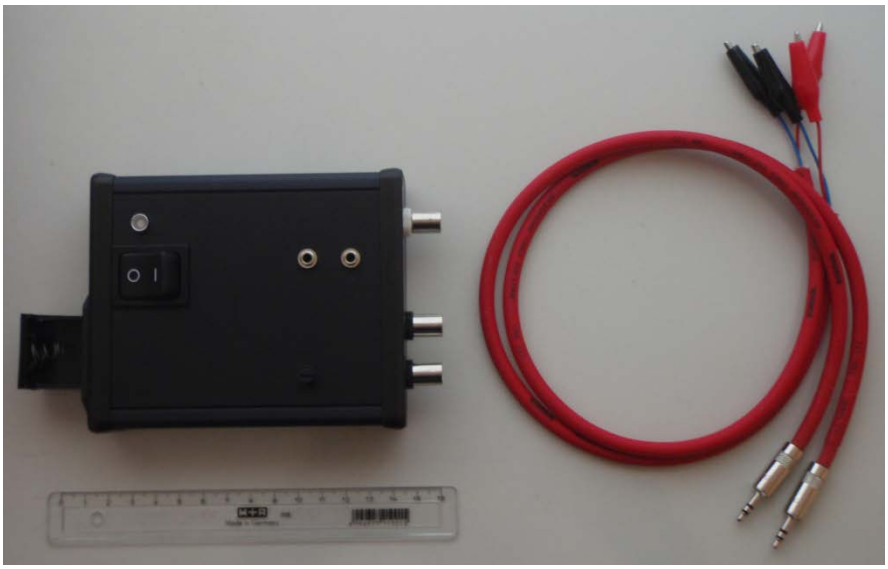

Figure 3.8. *The encased device and the measurement cables.*

3.3.4 Experimental Setups

At the early development stage the measurement system was first tested out with an equivalent circuit. The circuit was built using the one-path equivalent circuit model of the epithelium presented in Chapter 2.4.2. The circuit used two potentiometers that enabled the changing of the level of impedance. In addition to containing the epithelial and subepithelial components the current injection electrodes were also embedded to the equivalent circuit. This circuit is shown in **Figure 3.9**. The exact component values of the equivalent circuit were based on the experimental studies of MSc Virpi Savolainen and professor Jari Hyttinen (Savolainen 2011).

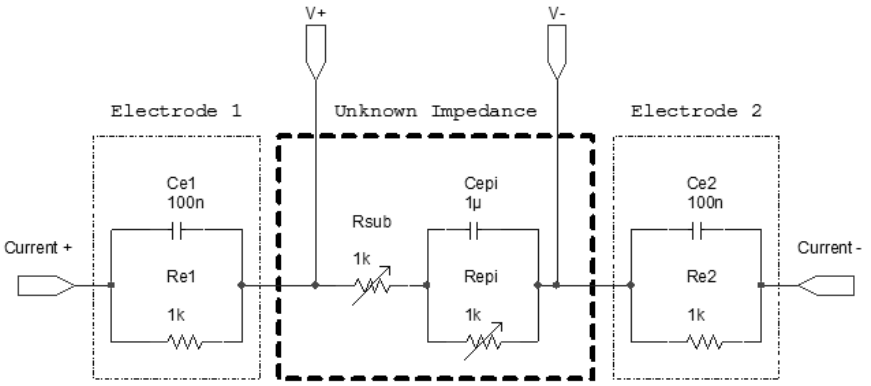

Figure 3.9. *The one-path electrical equivalent circuit of epithelium used for testing the measurement system.*

For the in vitro measurements two different types of sample setups were used. The functionality and accuracy of the impedance measuring device with electrodes as current carriers and voltage registers were assessed with a plastic test box. This box was manufactured at the university work shop. The test box was designed to utilize the same sample sliders as the commercial Ussing chambers by Physiologic Instruments. The sliders were P2307 (Physiologic Instruments, San Diego, USA) with a 2mm diameter aperture. The area of the aperture was 0.031 cm^2. **Figure 3.10** shows the test box with the sample slider in place. The material of the electrodes shown in the figure is 92.5% silver and the diameter of the electrodes is 2 mm. The test box was also used to assess the effect of different electrode materials on the measured frequency responses.

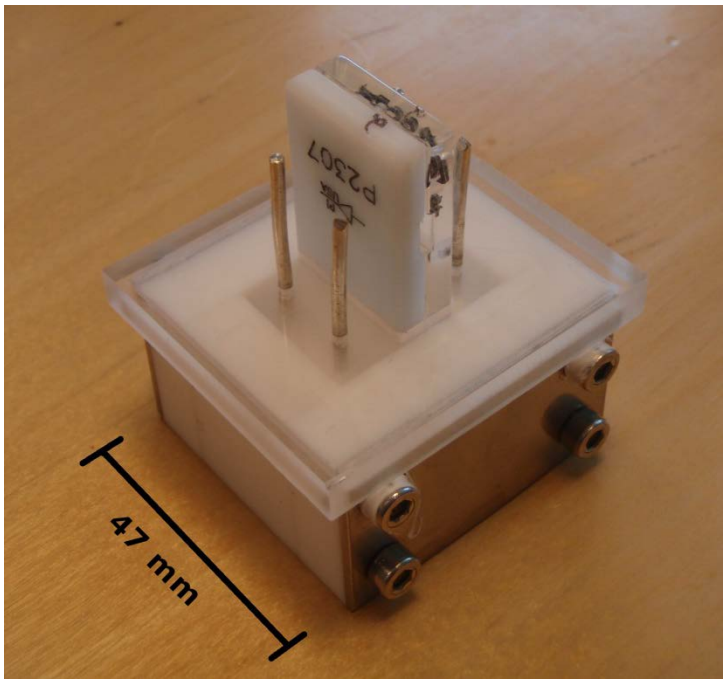

Figure 3.10. *The test box used in the thesis for testing the functionality of the impedance measuring device. In the picture the sample slider is placed to test box through the hole in the cover. The cover of the test box also housed the four silver electrodes mainly used in the test box measurements.*

The electrolyte used with the test box was phosphate buffered saline commonly known as Sörensen's buffer solution. This solution was made in accordance with standards ISO 15814:1999(E): Implants for surgery – Copolymers and blends based on polylactide – In vitro degradation testing, and ISO/DIS 13781: Poly-L-lactide resins and fabricated forms for surgical implants – In vitro degradation testing. One litre of buffer solution contained 1.65 g of KH_2PO_4 and 7.74 g of Na_2HPO_4 and the pH of the solution was 7.4 ± 0.2.

The first series of measurements with live samples were measured using P2300 Ussing Chambers (Physiologic Instruments, San Diego, USA) made of high quality acrylic resin also known as acrylic glass. The material is extremely durable, highly resistive and the heat transfer through the material is about 20% less than through equivalent thickness of glass. (Physiologic Instruments 2002) This commercial Ussing chamber setup is shown in **Figure 3.11**. Gas tubes perforated the samples continuously while the heating block kept the samples in constant temperature. The sliders were inserted to the middle of the chambers while the electrodes were placed as in the basic membrane experiment.

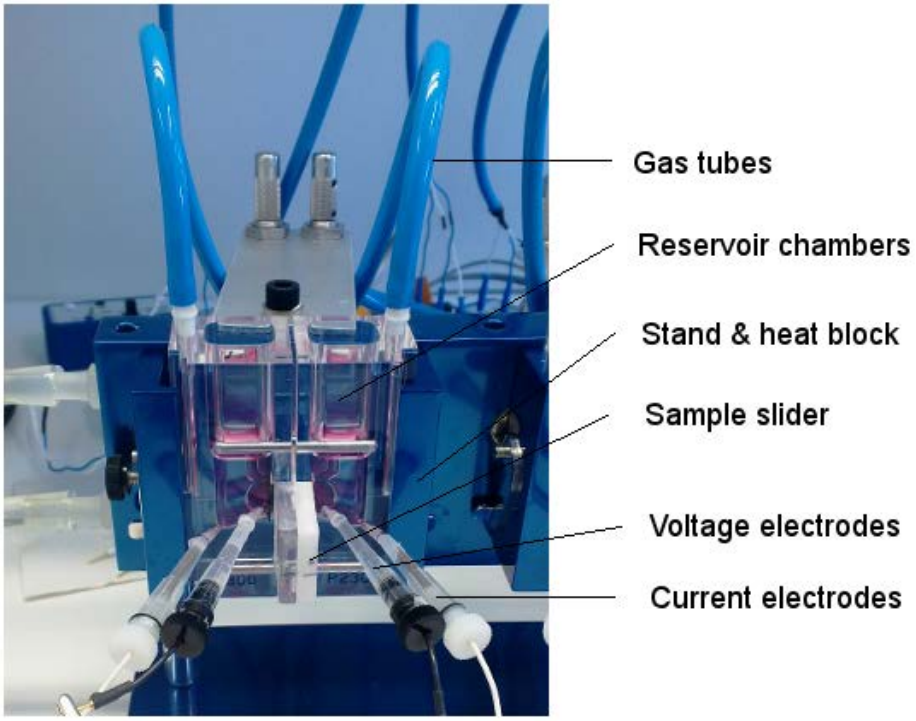

Figure 3.11.*The experimental setup with the Ussing chamber.*

The electrodes used were Ag/AgCl electrodes with agar salt bridges. They were each assembled by hand and this presented some variation to the electrode impedances. A close-up picture of one of the electrodes disassembled is shown in **Figure 3.12**.

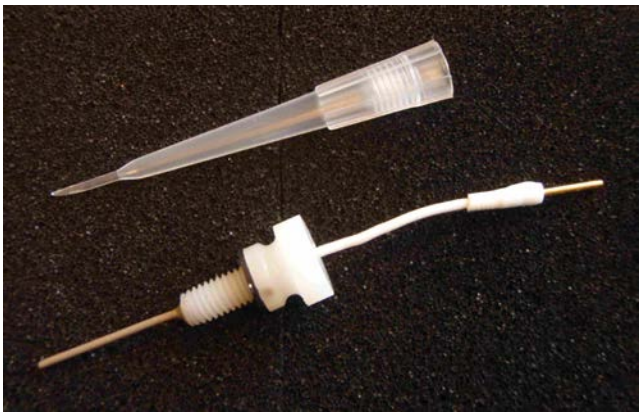

Figure 3.12. *Ag/AgCl electrode used in the Ussing Chamber measurements. The electrode is prepared for the measurements by sealing the tip of the plastic container with agar gel and by filling the container with highly conductive KCl electrolyte. Finally the electrode is placed to the plastic container and fastened tightly.*

The second measurements series with live cells was performed with a well plate, a setup frequently used in cell cultivation. In this setup the cell layer is grown in an insulating insert with a permeable bottom. This allows for the exchange of ions and nutrients across the membrane. The insert and the well create two separable volumes that both have electrodes for current injection and voltage measurement. This setup is shown in **Figure 3.13.**

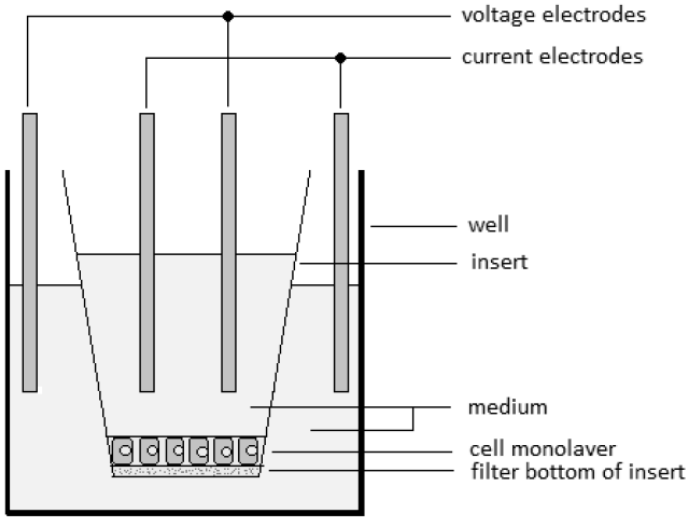

Figure 3.13. *The measurement setup used in the second RPE cell measurements. (Savolainen 2011)*

The well plate and the inserts used in the measurements were manufactured by BD Biosciences (Franklin Lakes, NJ, USA). The material of the well plate and the inserts was insulating polyethylene terephthalate (PET) and because of this the current flows through the filter bottom upon excitation. The area of this bottom was 0.3 cm^2, ten times larger than the aperture in the test box measurements. Due to the larger aperture and the proximity of the electrodes, significantly lower impedance levels were anticipated from the well plate measurements.

3.3.5 Parafilm M and RPE Cells

Before using living cells as samples preparatory measurements were done with Parafilm® M Barrier film (American National Can, Chicago, USA). The film is self-sealing and mouldable with a thickness of 127 µm. It is designed for laboratory sealing. (SPI Supplies 2012)

This film was used as an artificial membrane for measuring higher impedance levels than the level of the test box with an empty slider. The film was placed between the slider sheets and a 0.5 mm diameter hole was pierced through the film. This procedure increased the impedance of the slider by presenting a narrower current pathway. However since the plastic film did not possess any structural similarities with epithelia, for example microvilli, the resulting frequency spectrum was expected to be flat, that is to say that the impedance of the sample would be only resistive.

The first living cells measured were four RPE cell layers that were derived from induced pluripotent stem (iPS) cells. The origin of these iPS cells was the cell line 116A. The cells were first cultivated by Regea Cell and Tissue Center in embryoid-body formations for 57 days while the complete cultivation time was 96 days. The cultivation medium used in the process was a mixture of Dulbecco's Modified Eagle's Medium (DMEM) and Ham's F-12 Nutrient Mixture in 1:1 ratio. The medium did not contain any glutamine or HEPES. The latter is a commonly used in cell cultivation as buffer solution. The cultivation solution is also known as D-MEM/F-12 (Life Technologies Ltd., UK) and the list of amino acids, vitamins, inorganic salts and other components can be found from Life Technologies (2012). The same cultivation medium was also used as the electrolyte in the frequency response measurements of iPS derived RPE.

Preliminary TER measurements were done to assess the confluence of the four samples. These results are presented in **Table 3.1.**

Table 3.1. *Transepithelial resistances of four iPS derived RPE samples.*

	TER (Ω)
RPE 1	1080
RPE 2	1660
RPE 3	1020
RPE 4	1620

The measured TER values had two distinct levels: samples one and three gave resistances around one kiloohm whereas samples two and four TER values around 1.6 kiloohm, about 60% higher than samples one and three. This result gave strong reason to believe that samples two and four would be the best samples to exhibit a non-flat frequency response.

The second set of living cells were measured in similar conditions as the first set of RPE cells. Also the cultivation medium was the same as presented earlier. The cultivation time of the cells was longer than that of the first series, but the exact duration remained unclear. The measured TER values from the second RPE cell measurement series are presented in **Table 3.2**

Table 3.2. *TER values of the three RPE samples from the second measurement series. The values presented here are considerably lower than the resistances shown in Table 3.1 mostly due to the much lower base impedance levels of the well plate measurement setup.*

	TER (Ω)
RPE 1	300
RPE 2	400
RPE 3	400

3.4 Measurement Procedure

A typical epithelial measurement conducted with an Ussing chamber is preceded by a measurement of the resistance of the empty chamber. This way the chamber resistance can be subtracted from the actual epithelial measurements and the frequency response of the epithelium is obtained. Also depending on the electrode type the impedance of an individual electrode may vary over time which may reflect on the results. (Li et al. 2004)

The object of this Thesis was not however to measure the actual impedance of epithelial cell layers but to design a device for measuring the frequency response. Due to this the measurements for live cells were not first done with empty chambers to find out the base impedance level of the empty chamber but only with sample setups that already contained the cells. Also the contribution of error sources similar to both measurement methods were not included as the interest lies in the difference of the measurement results.

To assess the quality of the frequency response results all the measurements were also done with a traditional sine-sweep device, Solartron 1260. The device employed $10\mu A_{RMS}$ as the excitation current and the sweeps contained ten data points per frequency decade. The frequency band measured with Solartron was typically from 1 Hz to 1 MHz. The measurement setup was unchanged between the two measurement methods and the usual time difference between the two measurements was kept as short as possible to minimize the drift of electrode impedances from the results. This time taken to change the measurement method was usually about 1 minute. The measurement accuracy of the Solartron in the frequency band 1 Hz – 100 kHz was 1%.

The TEP measurements were also done with Millicell®-ERS Volt-Ohm meter (EMD Millipore Corporation, Billerica, MA, USA). This handheld device is designed to measure membrane potentials and resistances of epithelial cells in culture. Each electrode tip uses silver/silver chloride pellets to measure the voltage. The voltage was measured by immersing the electrodes by hand so that the electrodes were placed at both sides of the membrane. The measurement accuracy of the device was 0.1 mV.

The test box measurements were done at FinnMedi whereas all the cell measurements were conducted at Regea Cell and Tissue Center. All the Ussing chamber measurements were done with the chambers heated to 37 degrees of Celsius. The well plate measurements were however done in room temperature and about 45 minutes were given to the cells to stabilize after moving the inserts from cultivation wells to measurement wells.

4 RESULTS

This chapter presents he most important results obtained with the device. However **Chapters 4.1 and 4.2** first show the results of simulations and equivalent circuit measurements. These results give a good picture of the capabilities and weaknesses of the front-end electronics. **Chapter 4.3** presents the in vitro measurements conducted with the first prototype. In this chapter the effect of electrode polarization on the measured frequency responses is observed with three different types of electrodes. Also the frequency dependency of the polarization error is presented with two examples. The final in vitro measurements with the second prototype are presented in **Chapter 4.4**. For future measurements a post processing method of the results concerning the output impedance of the current injection is introduced in **Chapter 4.5**.

The results are presented as impedance spectrums where the differences between the results of the device and FRA are obvious. Where the difference is smaller due to improvements done to the device statistical methods are employed. When comparing the response results between the two methods the FRA, that is Solartron 1260, is referred to as the reference. The frequency band of the results is typically presented from 10 Hz to 10 kHz.

4.1 Simulation of Polarization Effects

The effect of large polarization impedances on the load voltage sensed by the IA were simulated using a similar schematic than the one presented in **Chapter 3.2** but without the DC voltage sources since ideally V1, V2 and V3 are equal and there is no DC current flow between them. Input bias resistors R_3 and R_4 were chosen as 100kΩ while all other resistors were set as 1kΩ. Circuit capacitors were selected to be 100nF. With these parameters the peak load voltage should ideally be 10 mV with current amplitude of 10µA. The frequency of excitation current was chosen as 1 kHz. First the simulations were done by keeping the resistance of electrode 2 (positive input of the IA) constant and increasing the resistance of electrode 1 (negative input of the IA). These simulation results are shown in **Table 4.1.**

Table 4.1. *Polarization of the negative input electrode of the IA and the effect on the input voltage of IA.*

R_{p1} (Ω)	$V_{IA1peak}$ (mV)	Error (%)
100	9.74	-2.6
1k	9.81	-1.9
10k	10.39	3.9
100k	13.50	35.0
1M	16.74	67.4

The results of **Table 4.1** show that large polarization resistance of the negative input electrode of IA increases the sensed voltage. With the two smallest polarization resistances the resistance of R_{e1} and the impedance of C_{e1} lower the sensed voltage. As the polarization resistance increases, the voltage sensed by the IA increases as well and the effect is considerable with heavy polarization. This increase would result in higher impedance levels than the actual impedance of the load.

After this the resistances of both electrodes 1 and 2 were increased simultaneously to see how polarization of both electrodes is reflected on the sensed voltage. These results are presented in **Table 4.2.**

Table 4.2. *The effect of equal polarization of the voltage sensing electrodes on the input voltage of IA.*

R_{p1} and R_{p2} (Ω)	$V_{IA1peak}$ (mV)	Error (%)
100	9.72	-2.8
1k	9.65	-3.5
10k	8.87	-11.3
100k	4.92	-50.8
1M	0.90	-91.0

The simulation results in **Table 4.2** show that the simultaneous electrode polarization considerably lowers the voltage sensed by the IA. This lowered voltage would reflect in the impedance calculations as lower impedance values than the actual impedance of the load. The polarization resistances of 100kΩ, same as the input bias resistors, result in about 50% error in IA input voltage. This illustrates the voltage division that takes place between the electrode polarization resistances and the input bias resistors.

The polarization effect can be minimized by selecting R_4 and R_5 as large as possible. All resistors however exhibit thermal noise, also known as Johnson noise, and this noise is amplified by the IA. The thermal noise RMS value v_n can be expressed as

$$v_n = \sqrt{4k_B T R \Delta f} \tag{27}$$

where k_B is the Boltzmann's constant, T the absolute temperature in kelvins, R the resistance and Δf the frequency band in hertz over which the noise is measured. This noise has an evenly distributed power spectral density, that is, it has a constant distribution over the frequency spectrum. The thermal noise of the input bias resistors is seen at the output multiplied by the gain of the IA.

The voltage noise at the IA inputs with 1 MΩ input resistors in room temperature and measured over the 0.02 – 500 kHz frequency band is close to $80\mu V_{RMS}$. With a gain of 30 the noise seen at the IA output is about 2.42 mV_{RMS}.

4.2 Equivalent Circuit Frequency Response

The second prototype was tested by measuring a frequency response with the equivalent circuit. In this measurement the equivalent circuit was set to maximum load, in other words the potentiometers R_{sub} and R_{epi} were set to 1 kilo-ohm each. The measured frequency response with a corresponding ideal response is presented in **Figure 4.1**.

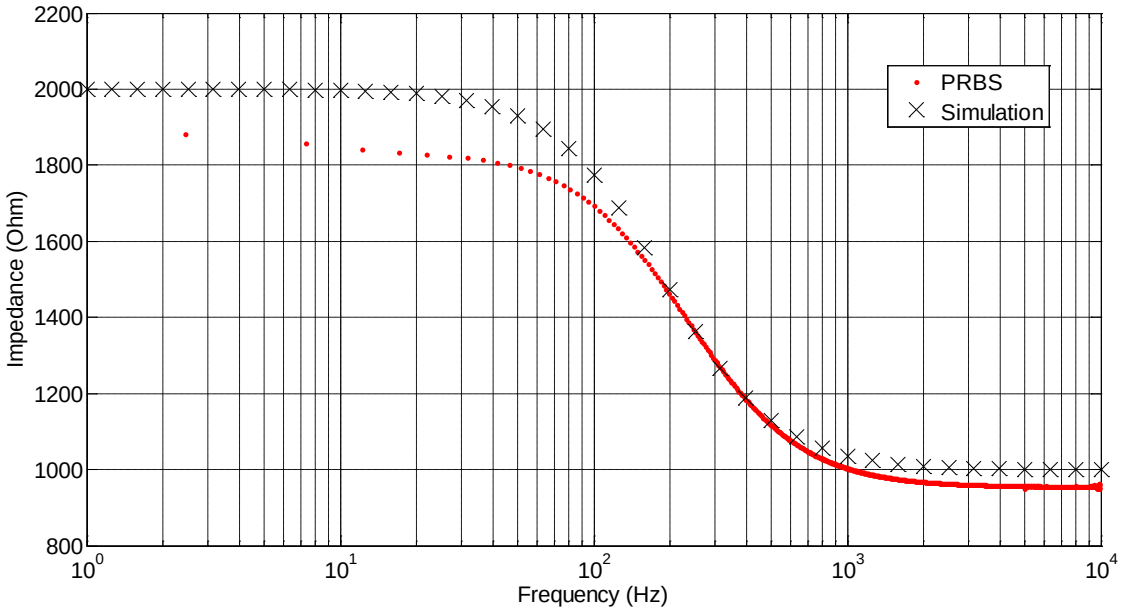

Figure 4.1. *Measured and simulated frequency responses of the equivalent circuit. The measurement with the device was implemented using PRBS excitation and algorithm presented in* ***Appendix 1****.*

The measured frequency response follows the simulated one considerably well. There are however some differences between the two measurement methods especially at low and high frequencies. **Table 4.3** shows the absolute and relative differences at four separate frequencies.

Table 4.3. *The differences at four distinct frequencies between the simulated frequency response and the response measured with the equivalent circuit.*

f (Hz)	Δ (Ω)	Δ (%)
10	-147	-7.4
100	-83	-4.7
1k	-92	-3.2
10k	-85	-4.5

The equivalent circuit is not precisely same as the one presented in **Chapter 3.3.4** due to component tolerances and the equivalent series resistance that practical capacitors have. Some of the observed difference is due to these non-idealities. The response of the equivalent circuit was measured with passive components modelling the electrode impedances. As the largest errors were expected to be encountered with the

use of in vitro electrodes, the slight difference of measured and simulated responses was merely noted but gave yet no reason to implement changes to the circuitry.

The equivalent circuit frequency response was also measured with several excitation signals that had less than 30 excitation sequences. The response was measured using 30, 20, 10, 5 and 1 sequence but no significant change was observed in the measured impedance levels. However the noise of the measured response was higher with fewer excitations. This is due to the averaging procedure of the algorithm.

4.3 In Vitro Measurements with the First Prototype

The impedance measurements of the test box were first done with the empty slider in order to test the device. This was followed by three measurement series to evaluate the repeatability of the measurements and to assess the systematic error of the results.

Electrode polarization was suspected as the reason for the systematic error. The effect of different electrode materials on the polarization error was observed with two measurement series; one with platinum electrodes and the other with silver/silver-chloride electrodes and agar bridges.

For raising the impedance level a plastic film was used in test box measurements. Since this artificial membrane did not exhibit any layered or folded structure that would result in capacitance, only a flat response was expected in each measurement.

4.3.1 Test Box with Ag/AgCl Electrodes

The impedance of the test box with empty slider was first measured to test the impedance measurement device. The impedance levels measured with the device were noticeably higher than the impedance levels obtained with the FRA. This difference was typically about 20% of the baseline impedance measured with FRA.

A second measurement series was done to assess the systematic errors the results obtained with the measurement device had. Also the repeatability of the measurements was studied with the second measurement series. Plastic film was used in the sample slider to obtain higher impedance levels. Altogether three frequency responses were measured with the both methods and these responses are shown in **Figure 4.2**.

The baseline impedance of the test box with plastic film was measured with the FRA to be around 2300 Ω. The corresponding baseline result with the device was about 2800 Ω. Thus the baseline impedance measured with the device exceeds the result of the FRA with 500 Ω that is about 22% of the measurement result of the FRA. The mean impedance of all three measurement series are presented in **Table 4.4**. Also the mean difference is calculated and this difference is presented as relative deviation from the Solartron results.

It can be seen from **Figure 4.2** that with low frequencies the impedance measured with the device increased slightly. This effect was even larger at frequencies below 10 Hz. This can be due to electrode polarization as the polarization capacitance gives rise to large impedances at low frequencies. The decrease of impedance with frequency in the first Solartron measurement can be assumed to be due to unstabilized electrode-electrolyte interface. The failure to measure low frequencies in the same measurement supports this assumption. There can also be seen noise around 5 kHz. This noise is caused by the design of the excitation signal.

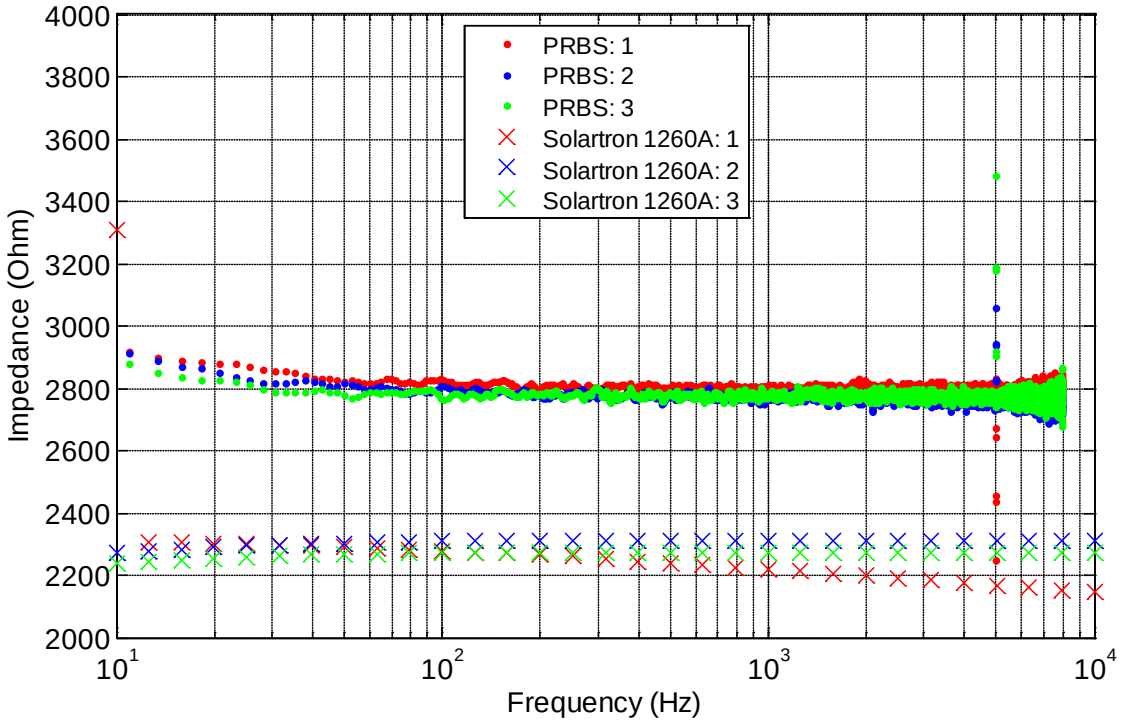

Figure 4.2. *Three consecutive frequency responses measured with the impedance measuring device (PRBS) and Solartron 1260A to assess the systematic error and repeatability of the measurements.*

In these measurements the highest frequencies the PRBS excitation was designed to include were around 10 kHz. Due to the inherent nature of the used excitation the excitation signal contains only little energy at the highest frequencies. This would be seen as the response becoming extremely noisy. This noisy part from 8 kHz to 10 kHz is left out of the **Figure 4.2** since it contains very little information. The time interval between the three measurement series was between 3 and 5 minutes. The first measurement with the FRA was unsuccessful with frequencies lower than 12.6 Hz. This can be seen as a single red data point around 3.3kΩ.

Table 4.4. *The mean impedances of all three measurement series. The frequency band of the results is from 10 Hz to 8 kHz. This leaves out the low frequencies, where the effects of polarization and high pass filter of the current input stage are present, and high frequencies where the energy content of the PRBS excitation signal is low.*

	μ_{PRBS} (Ω)	μ_{Sol} (Ω)	Δμ (Ω)	Δμ (%)
Meas. 1	2798	2279	519	23
Meas. 2	2763	2306	457	20
Meas. 3	2775	2268	507	22

4.3.2 Impedance Levels with Different Electrode Materials

Repeatedly measured higher impedance levels with the test box gave reason to suspect electrode polarization. To determine the dependence of this unwanted effect on the electrodes two measurement series with two different electrode materials was conducted. The materials chosen for testing were platinum and Ag/AgCl electrodes with agar bridges. The platinum and agar bridged Ag/AgCl electrodes were fastened to the test box by using a detachable cover with holes for inserting the electrodes. The salt bridged electrodes were the same kind as the ones presented in **Chapter 3.3.4** and used in the Ussing chamber measurements.

All the measurements were conducted with plastic film in the sample slider. The first electrodes to be tested were platinum electrodes. The observed frequency responses for the three measurement series are presented in **Figure 4.3**. The time interval of each measurement series was longer than in previous measurements, between five and seven minutes. This was due to the small size of the electrodes and the difficulties encountered in holding them fast to the test box cover.

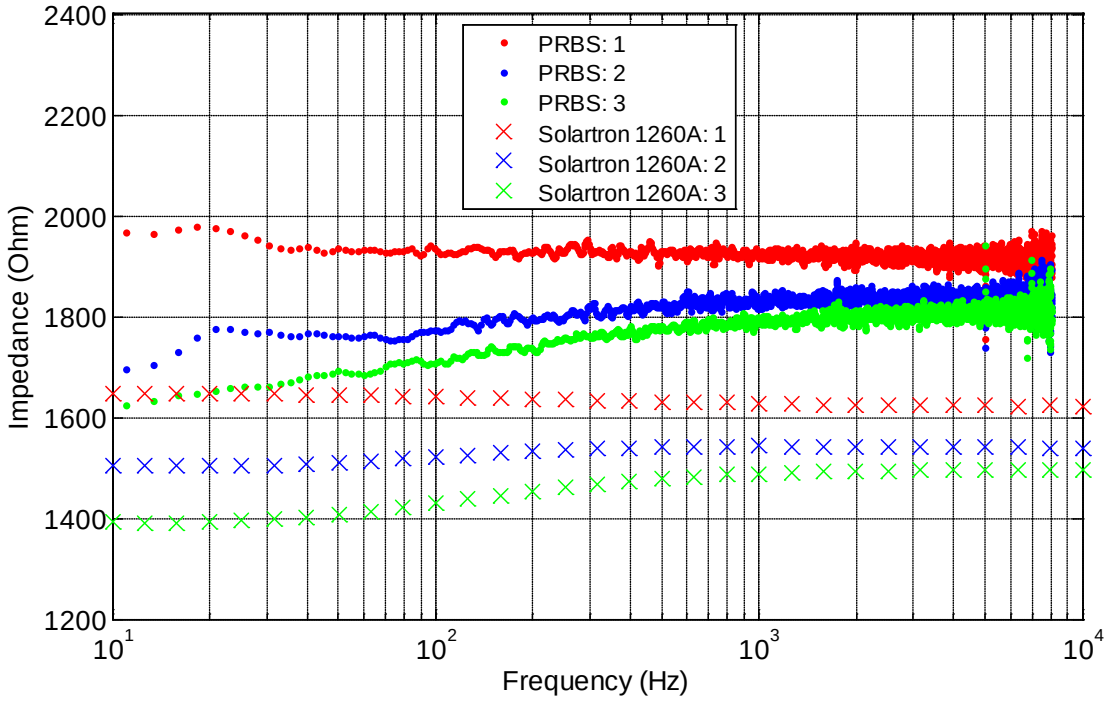

Figure 4.3. *Three measurement series with the test box using platinum electrodes. The PRBS measurements follow the shape of FRA results to some degree although again there are large differences in impedance levels.*

The responses in **Figure 4.3** have much lower impedance levels than the levels measured with silver/silver chloride electrodes in the previous chapter. Also the responses show decrease of impedance with time although this is most likely due to small fluctuations in the level of the electrolyte. This was caused by the porous cover used as the electrode stand. Another more interesting phenomenon is observed in the frequency band 10 – 40 Hz. The response measured with the device settles down with time to fol-

low the shape of response measured with the FRA. This most likely due to the stabilization of electrode-electrolyte interfaces.

As the frequency responses measured are not simply flat but exhibit frequency dependency especially in the last measurement series, simple mean impedance is a poor representative for assessing the difference. **Table 4.5** shows the impedances of all three measurement series at four distinct frequencies, that is 10 Hz, 100 Hz, 1 kHz and 8 kHz. If no data point was available for a particular frequency, one was extrapolated using two nearest data points.

Table 4.5. *The impedances of all three measurement series at four distinct frequencies.*

	Method	Z_{10Hz} (Ω)	Δ (Ω)	Z_{100Hz} (Ω)	Δ (Ω)	Z_{1kHz} (Ω)	Δ (Ω)	Z_{8kHz} (Ω)	Δ (Ω)
Meas. 1	**PRBS**	1987	340	1935	294	1917	289	1910	287
	Solartron	1647		1641		1628		1623	
Meas. 2	**PRBS**	1719	214	1775	254	1823	280	1820	280
	Solartron	1505		1521		1543		1540	
Meas. 3	**PRBS**	1630	238	1710	281	1797	309	1840	344
	Solartron	1392		1429		1488		1496	

The differences between the two measuring methods are between 214 ohms and 344 ohms. This gives relative errors between 14 and 23 percent for measurements with platinum electrodes. This is in the same range as the results with silver/silver chloride electrodes in the previous chapter.

The last electrodes to be tested were agar electrodes. With the first two measurements it became soon evident that the recorded impedance levels were extremely different from each other with the relative error being over 50%. Also the impedance measured with the device was repeatedly higher than the previous measurement result. This gave reason to conduct several measurements with the device to see where the response level would stabilize.

Eight consecutive frequency responses were measured with the device with 10 minutes spent between every measurement. The first measurement gave a flat response with an impedance level close to 250 ohms while the last response measured yielded an impedance level close to 4500 ohms. The reference measurement done with FRA gave a flat response with a level of 1350 ohms

Electrode polarization was suspected as the reason for this severe difference. To confirm the hypothesis the order of current injection and voltage measurement electrodes were reversed. Ideally and without any electrode polarization changing the order of electrodes would have no effect on the measured response. However the change was seen on the response as a doubling of the impedance level. A change back to the original electrode setup also lowered the response close to the level prior to the change.

Replacement of input bias resistors

The electrode polarization was countered by increasing the input bias resistors of the instrumentation amplifier. As stated in **Chapter 4.1** this decreases the amount of DC current flowing through the voltage sensing electrodes which is a major contributor to electrode polarization. The replacing resistors were selected to be 1 mega ohm, one decade larger than the originals. After the replacement the measurements with agar electrodes were repeated with the test box and plastic film. The time interval between the measurement series was about 5 minutes. The results from these measurements are shown in **Figure 4.4**.

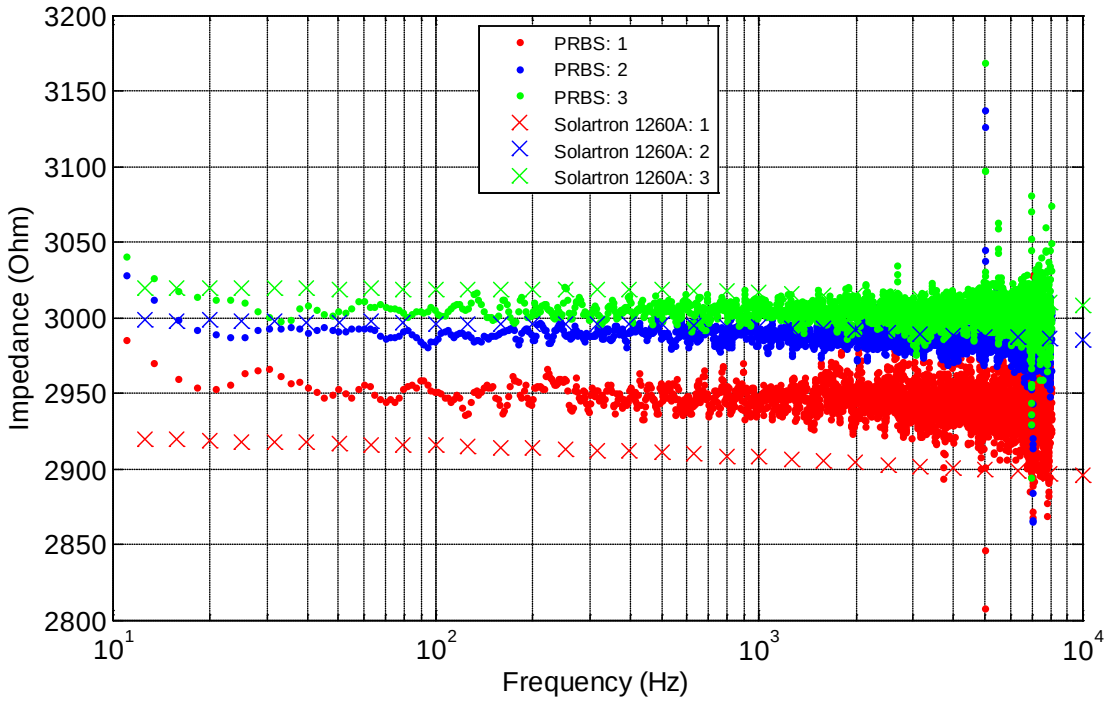

Figure 4.4. *Three measurement series with agar electrodes and the test box containing plastic film after replacing the input bias resistors of the IA. The PRBS response appears noisier than in previous measurements but this is in part due to the y-axis covering a much smaller impedance range.*

The frequency responses obtained with the device are in good agreement with the reference measurements. Since the shape of the responses is nearly flat, the mean impedances are again used to assess the differences between the two methods. These results are presented in **Table 4.6.**

Table 4.6. *Average impedances measured with replaced input bias resistors and plastic film.*

	μ_{PRBS} (Ω)	μ_{Sol} (Ω)	$\Delta\mu$ (Ω)	$\Delta\mu$ (%)
Meas. 1	2991	2910	81	2.78
Meas. 2	3007	2994	13	0.43
Meas. 3	3049	3017	32	1.06

The mean impedances in **Table 4.6** are almost similar between the two methods as the largest difference of three measurements is less than three percent. Also reliability of the measurement series is good with all the results having similar impedance levels. Another interesting observation is that the low frequency response does not shoot up like with other previous measurements, but decreases rapidly. A series of measurements was also done without the film and these results are presented in **Table 4.7.**

Table 4.7. *Average impedances of the empty test box after replacing the input bias resistors.*

	μ_{PRBS} (Ω)	μ_{Sol} (Ω)	$\Delta\mu$ (Ω)	$\Delta\mu$ (%)
Meas. 1	1194	1095	99	9.04
Meas. 2	1250	1189	61	5.13
Meas. 3	1297	1243	54	4.34

The differences of mean impedances without the plastic film are somewhat higher than with the film. This gives reason to believe the load impedance may affect the accuracy of the measurements. Although the impedance levels are lower without the plastic film the variation of reference results is larger than in **Table 4.6**. This may have been caused by the slight leaking of the test box.

4.3.3 Ussing Chamber measurements

The earliest Ussing Chamber measurements were done with the first prototype. Since the test box measurements gave out only flat frequency responses due to the inherent nature of the measurement setup it proved useful to test the device with living samples.

Unfortunately only some of the measured samples yielded non-flat frequency responses as the quality of the samples varied heavily. In following subchapters usually the best sample is used to present the results visually as it offers a straightforward analysis of the quality of the measurement device. The results from the whole measurement series with samples of lower quality included are presented statistically.

The following measurements were done with an excitation signal that covered a frequency band from 10 Hz to 100 kHz. Due to the wider band the RPE measurements had lower resolution than the test box measurements and this can be seen especially in **Chapter 4.3.4** where the measurement differences are examined in more detail.

iPS derived RPE measurements

The first measurements with Ussing chambers were done with four RPE cell layers. From the four frequency responses measured only two chambers exhibited clear frequency dependent behaviour. These were chambers number two and four. The frequency response of chamber number two is presented in **Figure 4.5** while the results from chamber number four are shown in **Figure 4.6**.

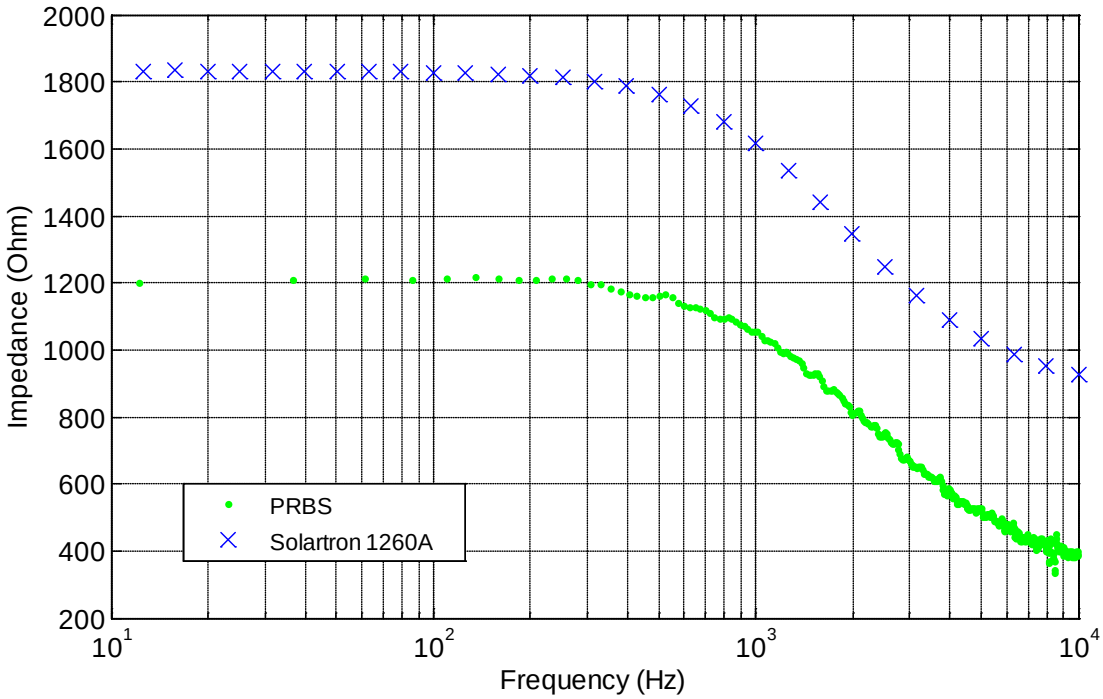

Figure 4.5. *The frequency response of RPE chamber number two. This response was measured with the first prototype.*

The impedance levels measured with the device did not match with the frequency responses obtained with FRA. The measured impedance of chamber number two in

Figure 4.5 is considerably lower than the reference, about 600 ohms. This phenomenon is repeated in **Figure 4.6** although the measured impedance is now much larger than the reference. This behaviour is a strong suggestion that electrode polarization takes place during the measurements.

The shapes of the measured responses do however follow the reference response quote well. The highest frequency for the calculation of low frequency impedance was chosen to be around 300 Hz as both frequency responses from chambers three and four had a similar shape. With Solartron this frequency was about 316 Hz whereas the corresponding frequency with the device was about 305 Hz. The low frequency impedances and the difference between the methods are presented in **Table 4.8**.

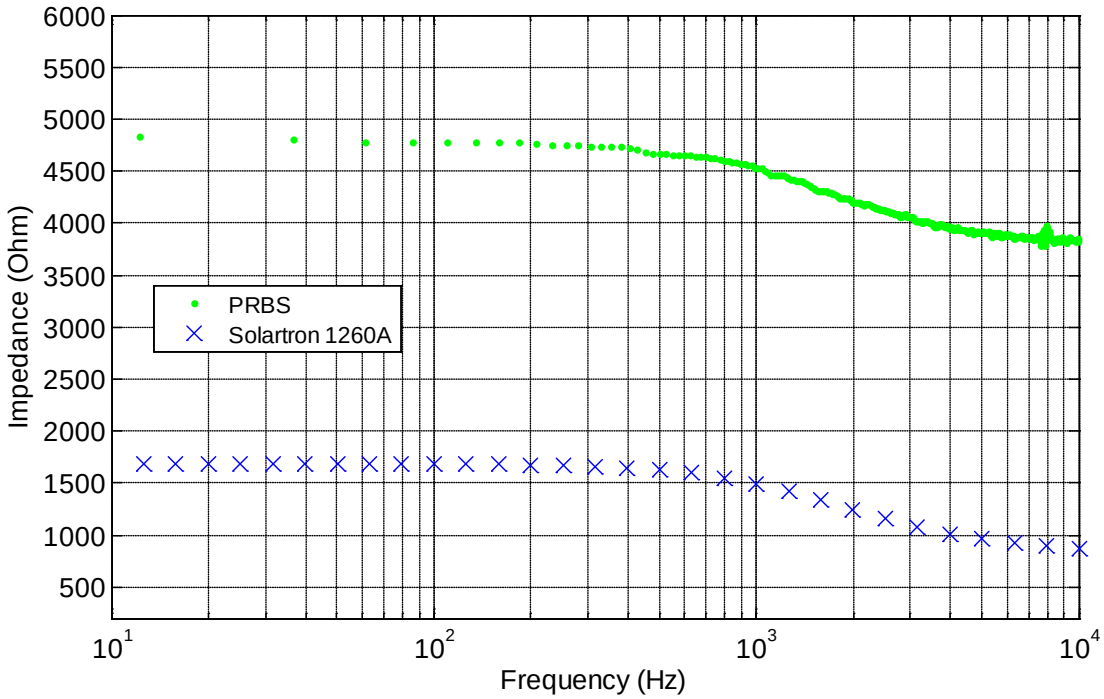

Figure 4.6. *Impedance of RPE chamber number four as a function of frequency. This response was measured with the first prototype.*

Table 4.8. *The low frequency impedances of measured chambers. In chambers one and three the impedance of the lower frequency range presents also well the whole measured frequency range since the samples did not exhibit any frequency dependency.*

	μ_{PRBS} (Ω)	μ_{Sol} (Ω)	$\Delta\mu$ (Ω)	$\Delta\mu$ (%)
Chamber 1	4054	899	3155	351
Chamber 2	1210	1828	-618	-34
Chamber 3	5736	1061	4675	441
Chamber 4	4774	1686	3088	183

4.3.4 Frequency Dependency of the Measurement Differences

The frequency dependency of the observed measurement difference was examined in more detail by comparing the frequency responses from the measurement device and Solartron. This was done to the RPE measurement results where a response with frequency dependency was recorded, in other words, a clear shift in impedance level was observed. Since the sine sweep results were gathered with less data points than the impulse response the excitation data points were compared to the nearest frequency point of the reference result to calculate the difference. The frequency dependent relative measurement differences of RPE samples number two and four presented in the previous chapter are illustrated in **Figure 4.7**.

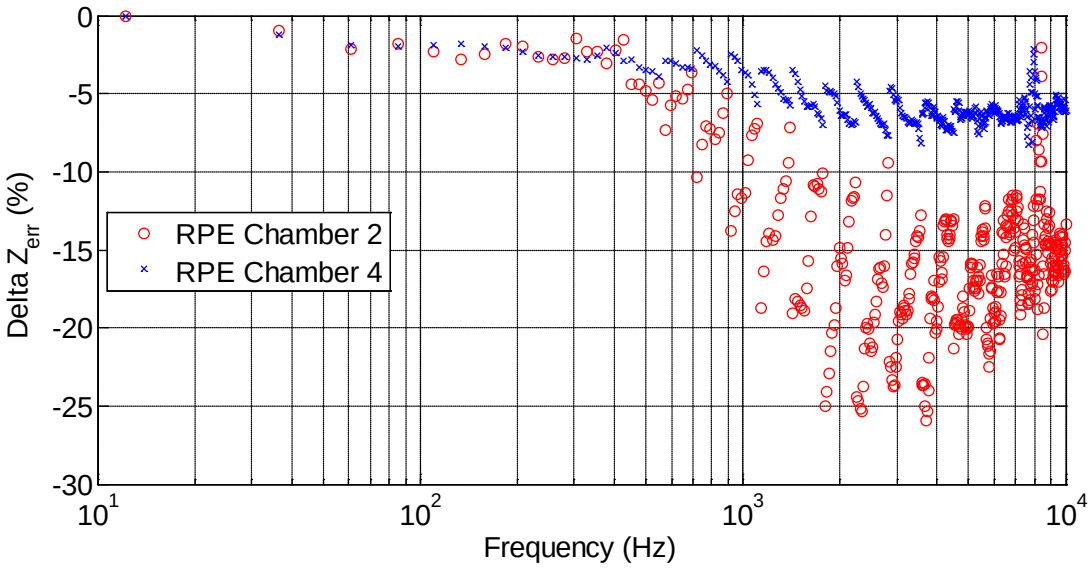

Figure 4.7. *The normalized relative differences of measured frequency responses with the reference. The baseline difference of low frequencies is removed to better illustrate the frequency dependency.*

The measurement difference is presented as a normalized relative difference. This means that the low frequency difference is subtracted from the impulse response and the resulting frequency dependent difference is divided by the same low frequency difference. This gives normalized relative differences that are due to the presentation method always 0 % at the frequency of 12 Hz. The highest frequency examined is 10 kHz as the shunting effect taking place at higher frequencies offers little insight.

The dispersion of the differences is caused by the scarcity of reference data points and the algorithm used to calculate the results. It is evident however that the measurement difference is divided into two bands with a clear transition band that starts from around 500 Hz and ends around 3 kHz. This is similar with the transition bands measured from both RPE samples.

4.4 In Vitro Measurements with the Second Prototype

Two different types of measurements similar to previous chapter were also done with the second prototype. First the improved device was tested with the test box and silver/silver-chloride electrodes with and without the plastic film as artificial membrane. Second, the effect of using shielded measurement cables were tested again with the test box and film. Finally the second prototype was used in another RPE cell measurement series with well plates as the measurement setup.

The time between the test box measurements was typically 2 minutes whereas the time spent between every RPE measurement was around 1 minute. Only the second RPE measurement series was done with the enclosure.

4.4.1 Test Box with Ag/AgCl electrodes

The second prototype was first used to measure the impedance of the empty test box. Again three frequency responses were measured with Solartron and the device. **Figure 4.8** shows the responses obtained with both methods.

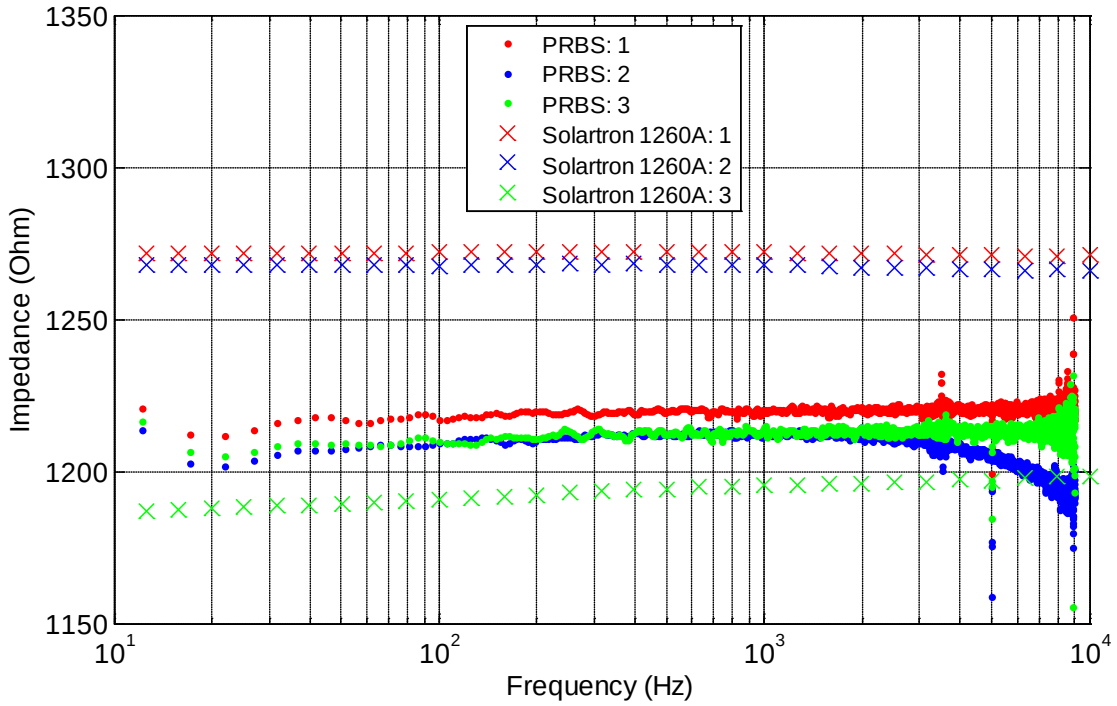

Figure 4.8. *Three frequency responses of the test box with empty sample slider.*

The frequency responses measured with the device show good repeatability although the second measurement shows shunting after 3 kHz. This may have been due to cable layout as it is not seen in other responses. This assumption is supported by the reference responses as the first two reference responses are similar but the third has somewhat lower impedance level. The second PRBS response was measured consecu-

tively with the third reference response which gives reason to assume that both measurements suffered from the same disturbance.

The impedance levels differ by about 5 percent in measurements one and two. The difference is much smaller in the third measurement but as the third reference response deviates clearly from the two previous reference responses, this similarity of results between two methods in the third measurement should not be given too much emphasis. All the mean impedances and the mean differences of impedance levels are presented in **Table 4.9**. The measured responses with the plastic film are presented in **Figure 4.9.**

Table 4.9. *The mean impedances of responses presented in* ***Figure 4.8*** *and the differences between the two methods.*

	μ_{PRBS} (Ω)	μ_{Sol} (Ω)	$\Delta\mu$ (Ω)	$\Delta\mu$ (%)
Meas. 1	1220	1272	-52	-4.26%
Meas. 2	1206	1268	-62	-5.14%
Meas. 3	1213	1193	20	1.65%

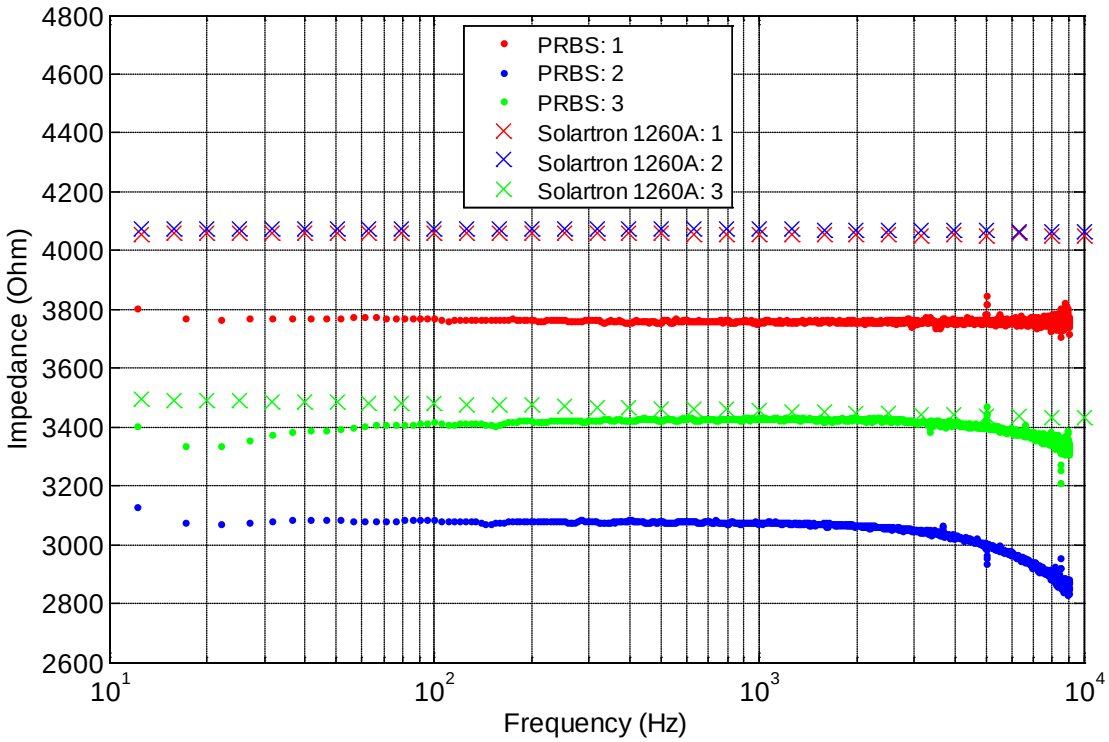

Figure 4.9. *Three measured responses with plastic film in the sample slider.*

The second PRBS response has considerably lower impedance level than the reference response and after this the third reference response is also much lower than the first two references. The last PRBS response is very close to the reference as in the measurements without the plastic film. The mean impedances and differences between the two methods are presented in **Table 4.10**.

Table 4.10. *Mean impedances of three response measurements with plastic film.*

	μ_{PRBS} (Ω)	μ_{Sol} (Ω)	$\Delta\mu$ (Ω)	$\Delta\mu$ (%)
Meas. 1	3760	4056	-296	-7.87%
Meas. 2	3013	4072	-1059	-35.15%
Meas. 3	3403	3467	-64	-1.88%

Shielded Cables

Identical measurements with the two previous measurement series were conducted also with shielded current injection and voltage measurement cables. The responses measured with the empty test box are presented in **Figure 4.10**.

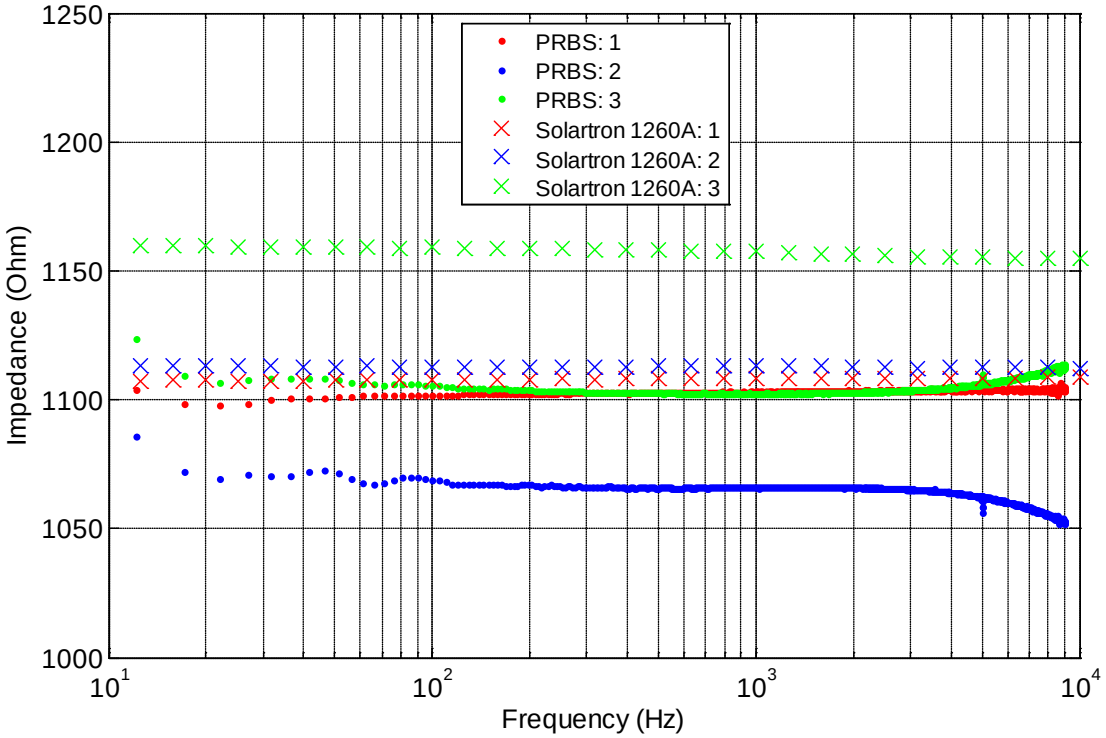

Figure 4.10. *Three frequency responses of the empty test box measured with shielded cables.*

The responses presented in **Figure 4.10** are quite similar in magnitude. The third reference response again has higher impedance level than the first and the second. This difference is similar in magnitude, about 50 ohms, as in the measurement series with empty test box and non-shielded cables.

The second and third PRBS responses show shunting at higher frequencies. This effect is however smaller than without the shielded cables. Also less noise is present than in the responses presented in **Figure 4.8**. This suggests that the number of excita-

tion repetitions could be lowered to see how much faster the measurement procedure can be made. The mean impedances and differences between the two methods are presented in **Table 4.11**.

Table 4.11. *Mean impedances of three response measurements with shielded cables and the empty test box.*

	μ_{PRBS} (Ω)	μ_{Sol} (Ω)	$\Delta\mu$ (Ω)	$\Delta\mu$ (%)
Meas. 1	1104	1108	-4	-0.36%
Meas. 2	1063	1113	-50	-4.70%
Meas. 3	1106	1158	-52	-4.70%

Three responses were also measured with the plastic film and shielded cables. These are presented in **Figure 4.11**. The responses presented have no disturbances encountered with previous measurements and show very good repeatability and the PRBS responses follow the reference responses quite well. It is however obvious that the responses measured with the device have systematic errors as the difference between the methods is almost constant between single measurement pairs. This observation is supported by the mean impedances and the mean differences calculated in **Table 4.12**.

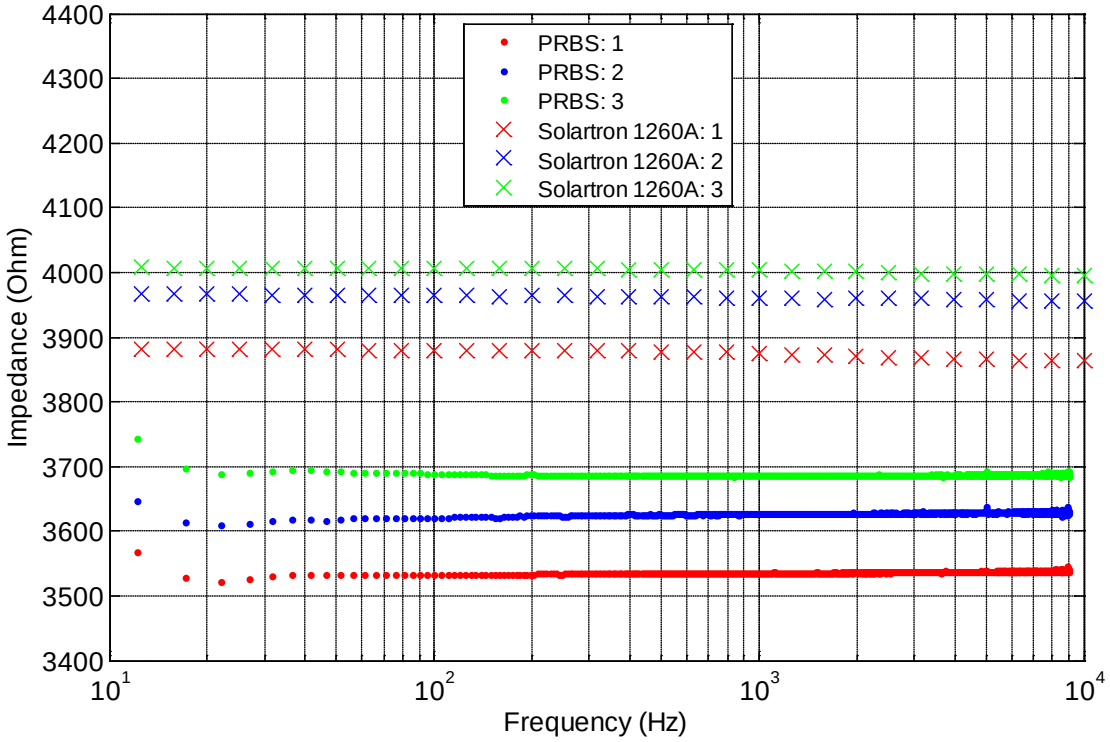

Figure 4.11. *Impedances measured with test box and plastic film in the sample slider. Shielded cables were used in the measurements.*

Table 4.12. *Mean impedances of three response measurements with shielded cables and plastic film as artificial membrane.*

	μ_{PRBS} (Ω)	μ_{Sol} (Ω)	$\Delta\mu$ (Ω)	$\Delta\mu$ (%)
Meas. 1	3570	3876	-306	-8.57%
Meas. 2	3628	3963	-335	-9.23%
Meas. 3	3687	4004	-317	-8.60%

4.4.2 Well Plate Measurements

The second set of RPE measurements were done with the well plate measurement setup. The well plate was chosen for the measurement setup as they are commonly used for cultivation purposes.

Five responses were measured from all the cell layers with the device and the reference. The averages of these measurements were used to calculate the relative differences between the two methods. The relative differences of the measured responses are shown in **Figure 4.12.** All the responses show much higher relative differences than those measured previously with the second prototype.

The impedance levels measured were lower than with other previous setups ranging from 180 ohms to about 400 ohms. As the measurement setup was otherwise highly similar to the previous setups, this gave reason to believe that the magnitude of the measured impedance contributed to the observed difference. This hypothesis was in line with the preliminary TER measurements where the RPE 1 had distinctly lower resistance compared to RPE 2 and RPE 3. In the frequency response measurements the relative difference of the low frequency impedance from RPE 1 was slightly larger than that of two other samples.

The load dependent difference would also in part explain the frequency dependency of measurement differences as the sensed load is lower at high frequencies due to the capacitive nature of the RPE cell layer.

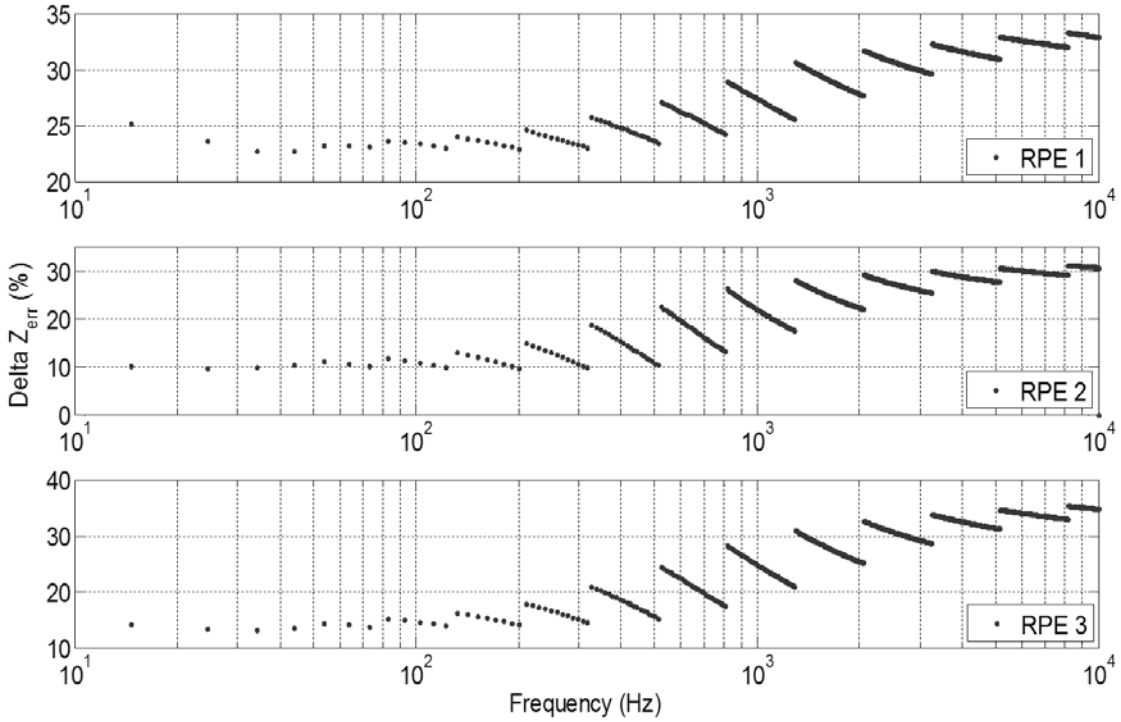

Figure 4.12. *Relative differences of impedances from three RPE cell layers measured with the device and the reference.*

4.4.3 Transepithelial potentials

The first transepithelial potentials were measured during the well plate frequency response measurements, but due to high offset voltages the output of the device was observed to saturate repeatedly although several measurement attempts were done. Also no potentials were successfully recorded with the Millicell ERS-2 meter due to very low TEP.

The well plate measurements remained the only occasion where the measurement of TEP was attempted. In practise the DC measurements would require a variable or adaptive gain at the input stage to eliminate the saturation of the output due to highly variable electrode offsets.

4.4.4 Noise Measurements

The amount of noise in the frequency responses measured was assessed by calculating the standard deviation of five consecutive responses from RPE sample number three from the well plate measurements. In practise the standard deviation was calculated for each 1024 frequency points from 5 impedance values. The resulting frequency dependent standard deviation is presented in **Figure 4.13**.

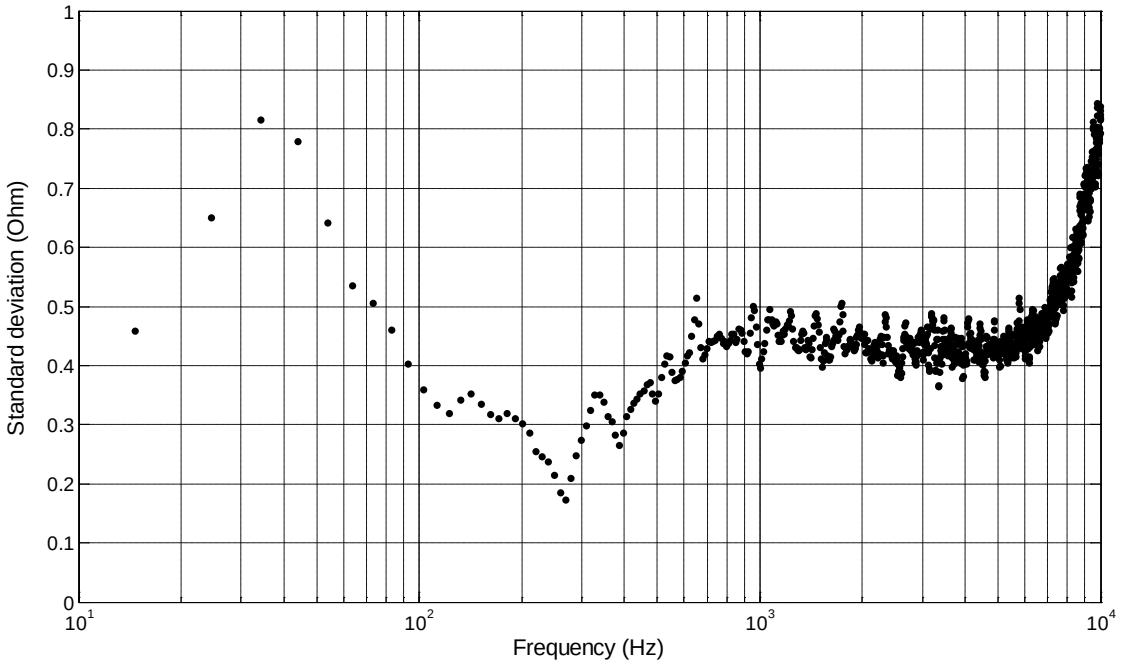

Figure 4.13. *Standard deviation of five frequency response measurements. The responses were measured from sample number three of the well plate measurements.*

The deviation is well defined from 1 kHz to 10 kHz but at lower frequencies it gets more erratic. In overall however the deviation is very small, less than an ohm and as such presents no problem for the measurement system. The maximum standard deviation for Solartron in the same measurements was about 0.12 ohms.

4.5 Output impedance compensation

The relative differences of measured frequency responses were repeatedly observed to be higher with loads below one kilo-ohm. On the other hand the difference remained predictable, around 5% to 10%, when measuring higher loads. This gave reason to conduct a series of simple resistor measurements with the device to see how the magnitude of the load would affect the measurement difference.

This chapter first presents the error source observed from the resistance measurements and the compensation calculated to eliminate the inherent error of the measurement system. After this the well plate measurement results are compensated using the compensation technique presented.

Although a compensation method is presented in this chapter, it only compensates for the current injection error and does not compensate the errors stemming from the electrode impedances.

4.5.1 Current output error

The load dependency of the measurement difference was assessed by measuring the response with known resistive loads. The effect of load resistances below one kilo-ohm was observed in detail whereas the higher load resistances were only measured with intervals of one kilo-ohm. The measurement error dependency on the load resistance is presented in **Figure 4.14.**

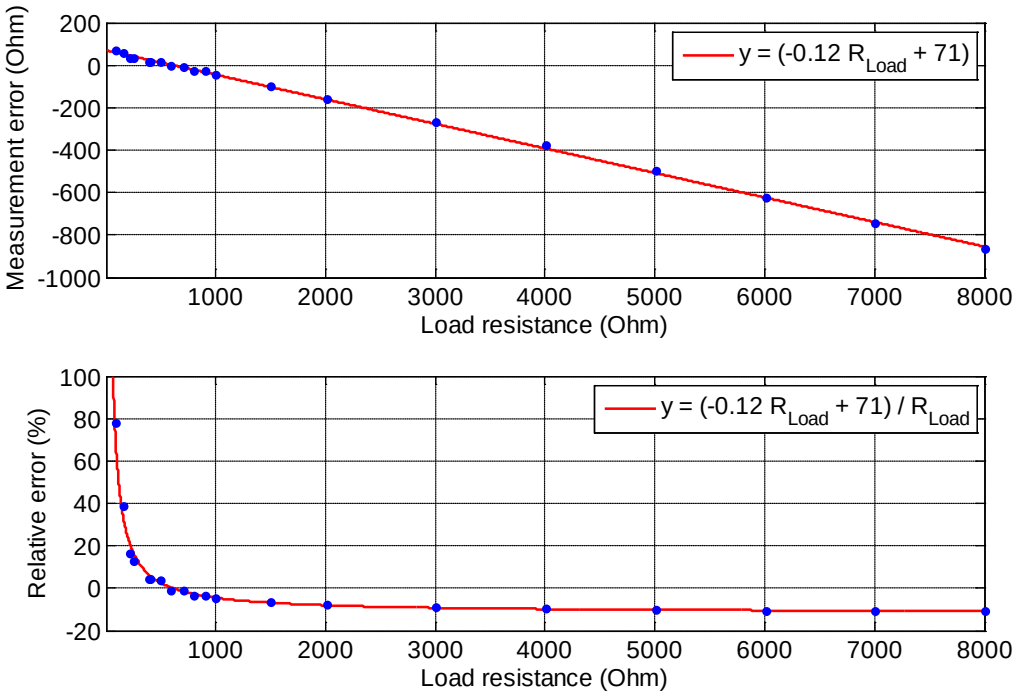

Figure 4.14. *Measurement error and relative error as the function of load resistance.*

It is evident that the measurement error is significant when measuring low load resistances. This is in accordance with observations from the well plate measurements

where low impedance levels resulted in substantial relative errors. The high load resistances show more predictable relative measurement error, another observation in line with the plastic film measurements.

Figure 4.13 includes a fitted line to the measurement errors. This equation

$$Error\ (\Omega) = -0.12\ R_{Load} + 71 \tag{38}$$

can be divided by the load resistance R_{Load} to get the relative error. This function can be used to compensate the current injection error as follows

$$Z_{comp} = \left(\frac{Z_{measured}}{1+Relative\ error}\right) \tag{39}$$

4.5.2 Compensated RPE impedances

The well plate measurement results were compensated using the compensation presented earlier. These compensated results are shown in **Figure 4.15**.

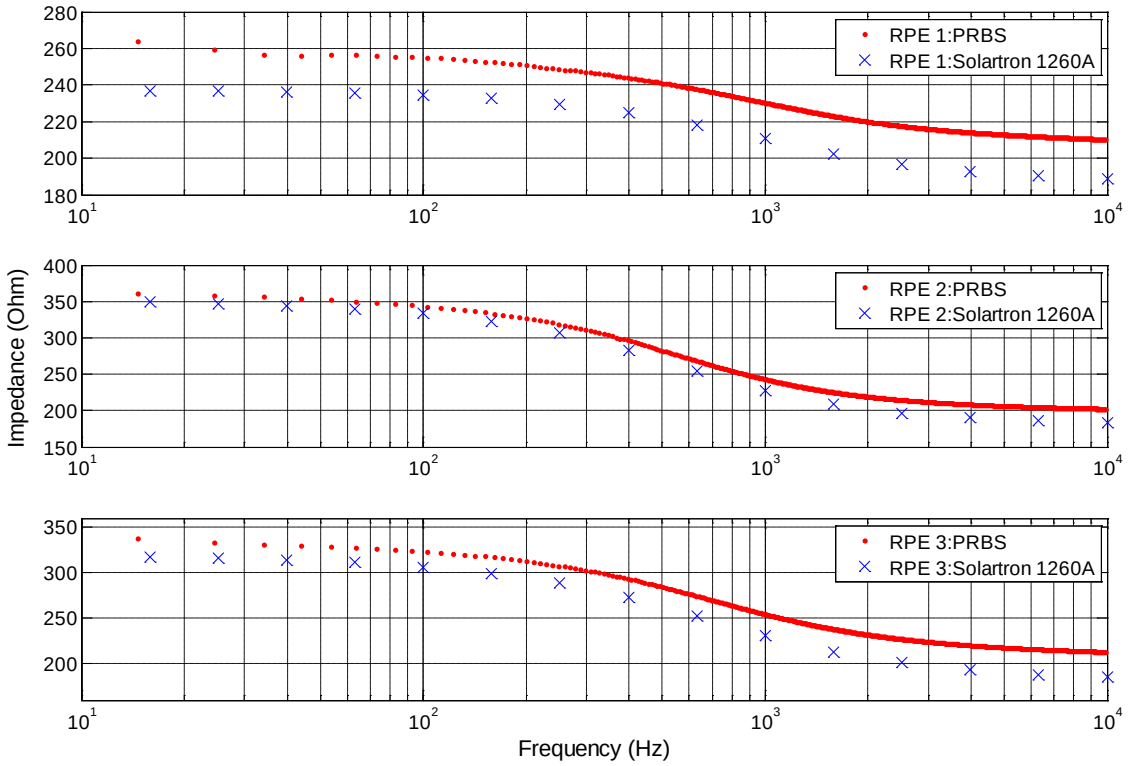

Figure 4.15. *Average compensated frequency responses from the three well plate RPE samples. Number of measurements for each average response was four.*

The relative differences of the presented average responses were also calculated and these relative differences are presented in **Figure 4.16**.

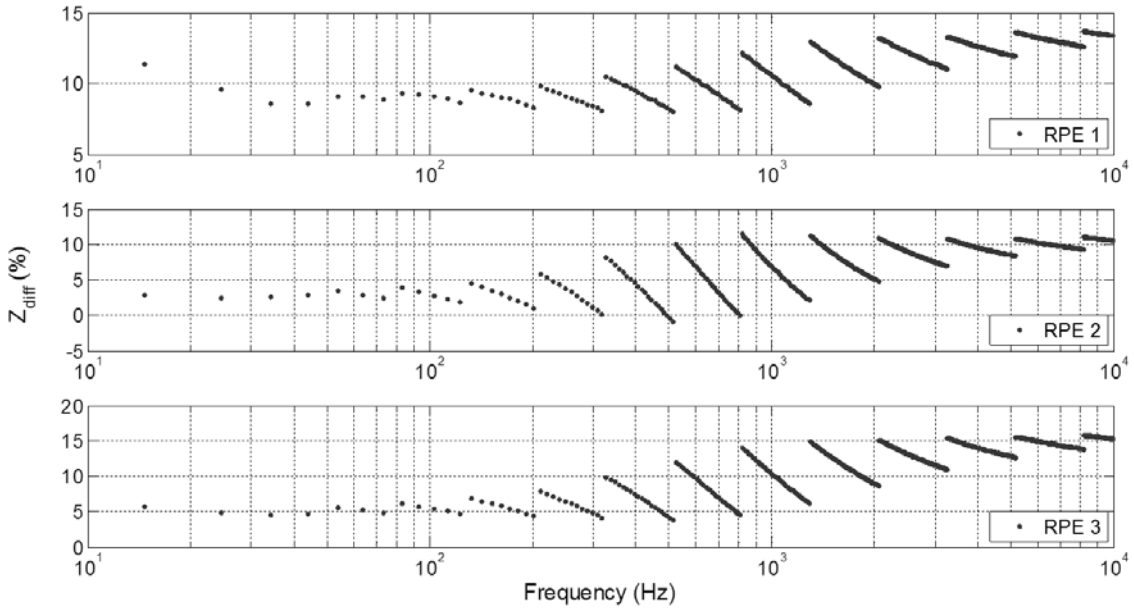

Figure 4.16. *Compensated relative differences of the three RPE layers measured with well plate setup. The responses used in the calculations are the average responses of four different measurements.*

5 DISCUSSION

The focus of this chapter is on the analysis of the measurement results obtained with the device and to give suggestions considering the further development of the front-end electronics. In **Chapter 5.1** the frequency responses are discussed with the emphasis on the measured impedance levels and the frequency dependency of measurement differences. After this the reasons for the failure to measure transepithelial potentials with the device are explained. **Chapter 5.2** examines the error sources introduced by the front end electronics to the frequency response measurement system and **Chapter 5.3** examines the further improvements that can be done to the device in order to decrease the observed differences of measured impedances. **Chapter 5.4** concludes the thesis by evaluating how the objectives of the thesis were completed and how well the device is suited for in vitro frequency response and potential measurements.

5.1 Analysis of the Measurement Results

The device developed in this thesis was tested using several different measurement setups and electrodes. The test box measurements with the first prototype and Ag/AgCl electrodes were conducted and the most important observation in these measurements was the severe impact of polarization impedances on the measurement accuracy. Also changing of the current injection and voltage measurement electrodes other way around did have a significant effect on the measured impedances thus reducing the benefit of using four electrodes for the measurements. Further testing was done using two measurement setups commonly used in cell research; Ussing chamber and well plate. The Ussing chamber measurements with four RPE samples did show that the measured responses followed the reference responses but contained systematic differences. After several improvements the second prototype was used to measure the responses of three RPE samples. This time the cell layers were grown on well plate inserts and the measurements were done in a custom made well plate with Ag/AgCl electrodes fastened on the plate cover.

The frequency responses measured with the second prototype are in good accordance with the shape of reference responses measured with Solartron. With purely resistive loads the IRS used as the excitation signal resulted in responses that had a maximum variation from 5 to 10 ohms in the frequency band of interest. The excitation used in most of the measurements covered the frequencies from 10 Hz to 10 kHz although due to lower SNR at high frequencies most of the responses presented are shown only up to 8 kHz. The maximum frequency of the excitation can be however increased easily to 100 kHz with no increase in time for the measurement procedure. The only

trade-off of this kind of modification is that the resulting response still consists of the same amount of data points as the excitation with lower bandwidth but the resolution of the response is slightly lower.

The impedance levels measured with the device are systematically lower than in the reference responses measured with Solartron 1260A. This difference is dependent on the magnitude of the load impedance and the type of electrodes used. Smallest differences were measured with Ag/AgCl electrodes with salt bridges and plastic film as the load impedance. The average relative difference in these measurements was less than a percent but this good result is a poor representative of the accuracy of the device as much larger relative differences, about fourfold, were obtained with lighter loads. However with loads larger than 700 ohms the relative difference was from 5 % to 10 %.

At 20 Hz the response measured with IRS excitation increased rapidly and the impedance increased continuously as the excitation frequency decreased. This was seen regardless of the load or the type of cables used. All this gives reason to believe that impedance peaking at low frequencies is due to electrode polarization. A polarized electrode can be modelled as a series circuit of a capacitor and a resistor and this gives the polarization impedance a base level and frequency dependency. As the voltage measurement electrodes polarize the measured impedance increases as presented in **Chapter 4.1**. Despite the rapid increase of impedance at low frequencies the behaviour at 20 Hz is not a severe problem as it lies very near the lowest frequency of interest.

The only electrodes used in the measurements that did not exhibit low frequency peaking were the Ag/AgCl electrodes with agar bridges. Even with lower input bias resistors the low frequency response remained stable and the measured impedances actually decreased at frequencies below 10 Hz although the impedance levels were substantially higher than the reference levels. One explanation for this is that the polarization of salt bridged electrodes affects only the resistance of the electrodes and the capacitive contribution is much smaller than in other electrodes.

In general the repeatability of the measurements is good. Especially the impedances measured with cables and plastic film are promising as the maximum deviation of relative errors between measurements is within one percentage point. Some difficulties were however experienced during the earlier measurements with the leaking of the test box. Therefore several measurements had to be done all over due to lower level of electrolyte in the test box as the level of electrolyte has a strong influence on the total measured impedance of the test box.

TEP measurements cannot be done with the second prototype as the device uses only one input stage with a constant gain for voltage measurement. In practice the measured offset voltages especially from the well plate proved to be so high that the output of IA was saturated repeatedly. If the gain of IA is kept constant the largest offset voltage that can be compensated with the device is about 80mV. However offset potentials as high as 200 mV were measured from the well plate.

5.2 Sources of Error in the Measurement System

This chapter discusses the different sources of error present in the measurement system. The analysis will begin with the simple theoretical analysis of inaccuracies introduced by practical aspects concerning the electronics. After this some thought is given to the contribution of the measurement environment and finally the measured differences due to the used measurement setups are discussed in detail.

The floating load principle presents several challenges concerning the DC levels used to float the load impedance. The first main contributor to the DC current flow is the slight difference between the reference voltage used in the current injection feedback loop and the output of amplifier connect directly to the load. Although the current injection circuitry contains a feedback loop for minimizing the effect of offset voltages of the amplifiers the loop does not completely eliminate the DC current flow as the offsets of the amplifiers used are not identical in practice. The second source of DC current flow rises from the difference between the voltages floating the current injection and voltage measurement electrodes. One reason for this may lie in the layout of the electronics and with better symmetry the difference could be minimized.

After the measurements some darkening of the tip of the current injection anode electrode was often observed. This was due to the reduction process taking place at the electrode-electrolyte interface. Without any DC current flow the oxidation and reduction processes at the interface would cancel each other out. The observation of electrode darkening is a strong indication of DC current flowing through the current injection electrodes. As there is no AC coupling at the voltage measurement inputs a small amount of the aforementioned DC current flows via the voltage electrodes also. The reduction process slowly thickens the coating and further imbalances the electrode impedances of voltage measurement electrodes.

Since the input impedance of the voltage measurement input stage is limited by the input bias resistors some of the excitation current can also flow through the voltage measurement electrodes. This polarizes the electrode in question and affects the voltage seen by the IA as presented in earlier. This error was decreased substantially by replacing the input bias resistors with larger ones but still some polarization is present in the second prototype.

The algorithm used to calculate the impedance spectrum makes many assumptions concerning the excitation signal. Since the excitation current is not measured, it is assumed to be constant $10\mu A_{AC}$ over the whole band of interest. The resistor measurement showed however that the output current does not stay constant as the load impedance changes. With 3 ohm resistor as a load an impedance of about 100 ohms was still measured. As the actual load was increased gradually the measurement error decreased slowly and around 700 ohms the error was insignificant. With higher loads the relative error stabilized between 5 % and 10 %. This phenomenon appears as frequency dependent difference in **Chapter 4.3.4** although the difference is caused by the lower load impedance at higher frequencies.

In the voltage measurement block the gain is set with two resistors that have 1% tolerance. In worst case the gain of 30 is lowered to 29.5 or increased to 30.5 due to the component tolerances. This again creates a frequency independent error to the measured impedance that has a magnitude of about 1.7 % of the actual load impedance.

There are not many sources of measurement error due to the measurement environment. The cells used in the measurements were cultured in a temperature of 37 degrees of Celsius but the measurements were however done in room temperature. As the equilibrium potentials of voltage measurement electrodes are dependent on the ambient temperature this difference of temperatures creates a slow drift to the measurements. The significance of this is however very small compared to the sources of errors presented above. Some frequency responses showed rapid increase or decrease in impedance with high frequencies. This phenomenon resembles current shunting but it is highly unlikely to be caused by such as the effect is already seen at 3 kHz and it does not take place in every measurement. Also none of the responses presented in **Figure 4.11** show similar behaviour which gives reason to believe that it is caused by measurement setup more than the measurement system. The reason for the erratic high frequency behaviour was left unknown although attempts were made to reproduce it. No significant 50 Hz noise was detected in any of the measured responses.

More significant sources of TEP measurement errors however rise from the measurement setup. If fixed electrodes are to be used to accurately measure TEP the immersed area of electrodes should be well defined in a similar fashion as in commercial applications. If the offset potential is zeroed in a different well than where the actual measurement is done the millivolt range of TEP is easily lost in the process as the offset potential is dependent on the immersed electrode surface area.

5.3 Future Considerations

The front-end electronics constructed as part of this thesis can be improved in several ways. A fundamental change should be considered regarding the current injection circuitry as the floating load principle presents several issues concerning DC levels and output impedance. The inaccuracies of current injection could also be compensated by measuring the response over the current setting resistor and by using this frequency response to calculate the actual injected current excitation. This actual excitation current could be used in the algorithm in place of ideal excitation and thus more accurate responses would be obtained. Another way used in this thesis is to post-process the recorded responses by compensating the results with a function presented in **Chapter 4.5.1.** The main benefit of the four electrode setup, the separation of current injection and voltage measurement, is lost if DC current flows through the voltage measurement electrodes thus polarizing them in the process. If this current flow cannot be entirely eliminated, much more consideration should be given to the phenomena taking place at the electrode level.

A much more simple way to improve the measured responses would be to AC couple the input stage of the voltage measurement electrodes. This would of course render the input stage useless for transepithelial potential measurements, but a parallel input stage could be designed for DC measurements. A switch could be implemented between the input stages with a relay or transistors to cut off the stage that is not used.
The offset compensation in TEP measurements could be automated using a microcontroller and a digital potentiometer. This kind of a system could also be used to vary the gain of the TEP measurement according to the measured offset voltages. To prolong the life of electrode coatings and to improve the accuracy of TEP measurements the electrodes should be shorted together when no measurements are conducted. This is done in most commercial TEP measurement devices. This kind of shorting could be done with similar switching circuitry as the splitting of voltage measurement input stage.

The cultivation and nurturing process of cell layers takes a long time and as a consequence the total cost of a single sample is not trivial. As a result the in vitro frequency response measurements in general would benefit greatly from an artificial membrane that would exhibit capacitance in addition to resistance. This kind of membrane would help in testing the measurement system and errors concerning the frequency dependency could be recognized with more ease.

5.4 Conclusions

In this MSc. thesis a device was developed for to be used as the front-end electronics in fast in vitro frequency response measurements. Inverse repeat sequence, a pseudo-random binary sequence modified for systems that include nonlinearities, was employed as the wideband excitation signal. In addition to frequency response measurements the front-end electronics were also planned to include capability for TEP measurement but this was not achieved due to various problems encountered with different electrode set-ups and few opportunities to measure cells with moderate TEP.

The floating load circuit used in the current injection block is a simple way to inject relatively constant wideband current to the load. The simplicity comes at the cost of inaccuracy as DC currents flow through the electrodes and polarization is observed as a result. The voltage measurement should have been divided into two separate input stages as the offset voltages encountered with various electrodes were much larger than originally anticipated.

The shape of frequency responses measured with the device are in good agreement with reference responses measured with a commercial frequency response analyser. The impedance levels however suffer from inaccuracies in range of 5% to 10%. These differences are mostly due to electrode polarization and low output impedance of the current injection. The repeatability and low noise of the measurement results were good although flowing DC currents would permanently change the electrode impedances in prolonged measurements.

The suitability of the device for in vitro frequency response measurements is dependent on the expected impedance levels and electrode impedances. The device does however give good estimates of the shape of the frequency responses and this information can be used to estimate the capacitance of the cell layer. The measurement system implemented in this thesis is also substantially easier to use due to its size and speed for research purposes where a fast estimate of the impedance of the cell layer is needed. In Ussing chamber measurements where the total impedance is over one kiloohm the difference of fewer than 10 % is compensated by the speed and the small size of the measurement system. Also if drug permeability of the cell layer is under study the absolute value of the impedance is not as interesting as the change of impedance upon addition of an agent.

Further research needs to be done in order to improve the accuracy of the measurement system developed here. The device itself can be improved by dividing the input of voltage measurement into two separate stages; one DC coupled and the other AC coupled. Also employing of digital potentiometers for easy offset compensation and gain varying would make the device more suitable for measuring TEP with highly varying offset voltages. In addition improved Howland or current conveyer solutions should be examined carefully in order to eliminate the DC current flows. Finally, the measurement system would also benefit from using partially insulated electrodes and with less variation between the electrodes.

REFERENCES

ACEA Biosciences Inc. 2011.Technology [WWW].[Cited: 11/07/2012]. Available at: http://www.aceabio.com/theory.aspx

Agilent Technologies. 2012. LCR Meters, Impedance Analyzers and Test Fixtures. [WWW].[Cited: 30/4/2012]. Available at: http://cp.literature.agilent.com/litweb/pdf/5952-1430E.pdf

Analog Devices. 2012. AD5933: 1 MSPS, 12 Bit Impedance Converter Network Analyzer. [WWW].[Cited: 11/07/2012]. Available at: http://www.analog.com/en/rfif-components/direct-digital-synthesis-dds/ad5933/products/product.html

Annus, P., Krivoshei, A., Min, M., Parve, T. 2008. Excitation Current Source for Bioimpedance Measurement Applications: Analysis and Design. IEEE International Instrumentation and Measurement Technology Conference Proceedings, Victoria, Vancouver Island, Canada, May 12–15, 2008.Piscataway, NJ, IEEE Service Center, pp. 848–853.

Asphahani, F., Zhang, M. 2007. Cellular Impedance Biosensors for Drug Screening and Toxin Detection. Analyst 132, 9, pp. 835–841.

Avago Technologies. 2010. HCNR200 and HCNR201 High-Linearity Analog Optocouplers Data Sheet. [WWW].[Cited 06/07/2012]. Available at: http://www.avagotech.com/docs/AV02-0886EN

Barsoukov, E. & Macdonald, J. R. 2005.Impedance spectroscopy theory, experiment, and applications.John Wiley & Sons, Inc. 595 p.

Bernd, K. Biology Department of Davidson College. 2010. Epithelial Cells. [WWW].[Cited: 16/5/2012]. Available at: http://www.bio.davidson.edu/people/kabernd/BerndCV/Lab/EpithelialInfoWeb/index.html

Bertrand, C.A., Durand, D.M., Saidel, G.M., Laboisse, C., Hopfer, U. 1998. System for Dynamic Measurements of Membrane Capacitance in Intact Epithelial Monolayers. Biophysical Journal 75, 6, pp. 2743–2756.

BioMediTech. 2012. Human Spare Parts. [WWW].[Cited: 30/4/2012]. Available at: http://www.biomeditech.fi/research/human_spare_parts_program.php

Borges, E., Figueiras, E., Pereira, H.C., Cardoso, J.M., Ferreira, L.R., Correia, C. 2010. Optically Isolated Current Source. World Congress on Medical Physics and Biomedical Engineering, Munich, Germany, September 7 - 12, 2009,IFMBE Proceedings 25, 4, pp. 2020–2023.

Bragos, R.,Roselli, J., Riu, P. 1994. A Wide-band AC-coupled Current Source for Electrical Impedance Tomography. Physiological Measurement 15, 2A, pp. A91–A99.

Cole, K.S., Cole, R.H. 1941. Dispersion and Absorption in Dielectrics. Journal of Chemical Physics 9, pp. 341–351.

Dorf, R.C., Bishop, R.H. 2008. Modern Control Systems.11th edition, Pearson Education Inc., Pearson Prentice Hall,1018 p.

Dubé J., Rochette-Drouin O., Lévesque P., Gauvin R., Roberge C.J., Auger F.A., Goulet D., Bourdages M., Plante M., Germain L., Moulin V.J. 2010. Restoration of the transepithelial potential within tissue-engineered human skin in vitro and during the wound healing process in vivo. Tissue Engineering Part A 16, 10, pp. 3055–3063.

Franco, S. 2002. Design with Operational Amplifier and Analog Integrated Circuits. 3rd ed., International ed., New York, McGraw-Hill, 658 p.

Gabrielli, C. 1984. Identification of Electrochemical Processes by Frequency Response Analysis.Solartron Technical report number 004/83.[WWW].[Cited: 06/06/2012]. Available at: http://www.solartronanalytical.com/Pages/ApplicationTechnicalNotes.htm

Gawad, S., Sun, T., Green, N.G., Morgan, H. 2007. Impedance Spectroscopy Using Maximum Length Sequences: Application to Single Cell Analysis. Review of Scientific Instruments 78, 5.

Gitter, A.H.,Bertog, M., Schulzke, J.D., Fromm, M. 1997.Measurement of Paracellular Epithelial Conductivity by Conductance Scanning.PflugersArchiv European Journal of Physiology 434, 6, pp. 830–840.

Gitter, A.H., Schulzke, J., Sorgenfrei, D., Fromm, M. 1997. Ussing Chamber for High-Frequency Transmural Impedance Analysis of Epithelial Tissues. Journal of Biochemical and Biophysical Methods 35, 2, pp. 81–88.

Grimnes, S. &Martinsen, Ø.G. 2008.Bioimpedance and Bioelectricity Basics.Second Edition.Academic Press.471 p.

Golomb, S. 1967. Shift Register Sequences. San Fransisco, Holden-Day.

Good Will Instrument Co. 2010.LCR-8000G Series.[WWW].[Cited: 30/4/2012]. Available at: http://www.gwinstek.com/en/product/productdetail.aspx?pid=39&mid=79&id=1177

Günzel, D., Zakrzewski, S.S., Schmid, T., Pangalos, M., Wiedenhoeft, J., Blasse, C., Ozboda, C., Krug, S.M. 2012.From TER to Trans- and Paracellular Resistance: Lessons from Impedance Spectroscopy. Annals of the New York Academy of Sciences 1257, 1, pp. 142–151.

Haug, E., Sand, O., Sjaastad, Ø.V., Toverud, K.C. 1999. Ihmisen Fysiologia, 2nd ed. Porvoo. WSOY. 526 p.

Hong, H., Rahal, M., Demosthenous, A., Bayford, R.H. 2008.Floating Voltage-controlled Current Sources for Electrical Impedance Tomography. European Conference on Circuit Theory and Design 2007, ECCTD 2007, Seville, Spain, August 26–30, IEEEConference Publications.

King, D. Southern Illinois University School of Medicine. Epithelium Study Guide [WWW]. [Cited: 16/5/2012]. Available at: http://www.siumed.edu/~dking2/intro/epith.htm

Krug, S.M., Fromm, M., Günzel, D. 2009.Two-Path Impedance Spectroscopy for Measuring Paracellular and Transcellular Epithelial Resistance. Biophysical Journal 97, 8, pp. 2202–2211.

Laitala-Leinonen, T. 2004. Epiteeliluento 18.10.2004. Turku University Anatomy [WWW]. [Cited: 05/10/2012]. Available at: http://bonebiology.utu.fi/tilale/luennot/epiteeliluento181004.pdf

Land, R., Cahill, B.P., Parve, T., Annus, P., Min, M. 2011.Improvements in Design of Spectra of Multisine And Binary Excitation Signals for Multi-frequency Bioimpedance Measurement. Proceedings of the Annual International Conference of the IEEE Engineering in Medicine and Biology Society, EMBS, Boston, MA, USA, August 30– September 3, Stoughton, Wisconsin, The Printing House, Inc., pp. 4038–4041.

Lewis, S.A.& Diamond, J.M. 1976. Na+ Transport by Rabbit Urinary Bladder, a Tight Epithelium. Journal of Membrane Biology 28, 1, pp. 1–40.

Li, H., Sheppard, D.N., Hug, M.J. 2004.Transepithelial Electrical Measurements with the Ussing Chamber. Journal of Cystic Fibrosis3, 2, pp. 123–126.

Life Technologies Corporation. 2012. Technical Resources - Media Formulations [WWW]. [Cited: 28/08/2012]. Available at: http://www.invitrogen.com/site/us/en/home/support/Product-Technical-Resources/media_formulation.329.html

Ljung, L. 1987. System Identification: Theory for the user. Englewood Cliffs, New Jersey, Prentice-Hall, Inc. 519 p.

Lo, C-M., Keese, C.R., Giaever, I. 1995. Impedance Analysis of MDCK Cells Measured by Electric Cell-Substrate Impedance Sensing. Biophysical Journal 69, pp. 2800–2807.

Malmivuo, J. &Plonsey, R. 1995.Bioelectromagnetism - Principles and Applications of Bioelectric and Biomagnetic Fields - web edition, [WWW].[Cited: 24/07/2012]. Available at: http://www.bem.fi/book/

Maminishkis, A., Chen, S., Jalickee, S., Banzon, T., Shi, G., Wang, F. E. et al. 2006. Confluent Monolayers of Cultured Human Fetal Retinal Pigment Epithelium Exhibit Morphology and Physiology of Native Tissue. Investigative Ophthalmology & Visual Science 47, 8, pp. 3612-3624.

Markx, G.H. & Davey, C.L. 1999.The Dielectric Properties of Biological Cells at Radiofrequencies: Applications in Biotechnology. Enzyme and Microbial Technology 25, 3–5, pp. 161–171.

McNeil, E., Capaldo, C.T., Macara, I.G. 2006.Zonula Occludens-1 Function in the Assembly of Tight Junctions in Madin-Darby Canine Kidney Epithelial Cells.Molecular Biology of the Cell 17, 4, pp. 1922–1932.

Metrohm AG. 2012. Autolab Application Note EIS02.[WWW].[Cited: 14/07/2012]. Available at: http://www.metrohm-autolab.com/export/Homepages/Autolab/download/Applicationnotes/Autolab_Application_Note_EIS02.pdf

Miao, B., Zane, R., Maksimovic, D. 2004. A Modified Cross-correlation Method for System Identification of Power Converters with Digital Control.IEEE 35th AnnualPower Electronics Specialists Conference, PESC 04. 2004, volume 6, Aachen, Germany, June 20–26, IEEE Conference Publications, pp. 3728–3733.

Millipore. 2012. Millicell ERS-2 Volt-Ohm Meter and Accessories.[WWW].[Cited: 30/4/2012]. Available at: http://www.millipore.com/catalogue/module/c77976

Min, M., Land, R., Annus, P., Ojarand, J. 2011. Chirp Pulse Excitation in the Impedance Spectroscopy of Dynamic Subjects — Signal Modelling in Time and Frequency Domain. Lecture Notes on Impedance Spectroscopy. Lecture Notes on Impedance Spectroscopy: Measurement, Modeling and Applications , pp. 79-82.

Min, M., Paavle, T., Ojarand, J. 2011. Time-Frequency Analysis of Biological Matter Using Short-Time Chirp Excitation.20th European Conference on Circuit Theory and Design, ECCTD 2011, Linköping, Sweden, August 29–31, pp. 298–301.

Misaridis, T.X., Jensen, J.A. 2005. Use of Modulated Excitation Signals in Medical-Ultrasound. Part II: Design and Performance for Medical Imaging Applications,IEEE Trans. on Ultrasonics, Ferroelectrics, and Frequency Control 52, 2, pp. 192–207.

Molecular Devices. 2012. Label-Free Analysis. [WWW].[Cited: 30/4/2012]. Available at: http://www.moleculardevices.com/Products/Instruments/Label-Free-Analysis.html

nanoAnalytics. 2012. cellZscope® - The Automated Cell Monitoring System. [WWW].[Cited: 30/4/2012]. Available at:
http://www.nanoanalytics.com/en/hardwareproducts/
cellzscope/index.php

nanoAnalytics. 2012. cellZscope - How It Works - Barrier Forming Tissue. [WWW]. [Cited: 10/07/2012]. Available at: http://www.nanoanalytics.com/en/hardwareproducts/ cellzscope/howitworks/chapter01/index.php

National Instruments. 2011. High-Speed M Series Multifunction DAQ for USB - 16-Bit, up to 1.25 MS/s, Integrated BNC Connectivity. [WWW].[Cited: 02/08/2012]. Available at:http://sine.ni.com/ds/app/doc/p/id/ds-21/lang/en

Ojarand, J., Giannitsis, A.T., Min, M., Land, R. 2011.Front-end Electronics for Impedimetric Microfluidic Devices.Proceedings of SPIE vol. 8068- The International Society for Optical Engineering, Prague, Czech Republic, April 18–20, Bellingham, Washington, SPIE.

Onnela, N., Savolainen, V., Juuti-Uusitalo, K., Vaajasaari, H., Skottman, H., Hyttinen, J. 2011. Electric Impedance of Human Embryonic Stem Cell-derived Retinal Pigment Epithelium. Medical and Biological Engineering and Computing 50, 2, pp. 107–116.

Paavle, T. 2008. Using of Chirp Excitation for Bioimpedance Estimation: Theoretical Aspects And Modelling. Electronics Conference, 2008.BEC 2008.11th International Biennial Baltic. Tallinn, Estonia, October 6–8, IEEE Conference Publications, pp. 325–328.

Paavle, T., Min, M., Trebbels, D. 2011.Low-energy Chirps for Bioimpedance Measurement. 34th International Conference on Telecommunications and Signal Processing, TSP 2011 – Proceedings, Budapest, Hungary, August 18–20, IEEE Conference Publications, pp. 398–402.

Physiological Instruments. 2002. Physiological Care and Feeding Instructions forEasyMount Chambers. [WWW].[Cited: 02/08/2012]. Available at:y946j.9wv5p.servertrust.com/v/vspfiles/downloadables/EasyMount Care and Feeding Instructions.pdf

Pliquet, U., Gersing F., Pliquett, F. 2000. Broadband Excitation for Short-time Impedance Spectroscopy.Physiological Measurement 26, pp. 185–192.

Quinn, R. H. & Miller, S. S. 1992. Ion Transport Mechanisms in Native Human Retinal Pigment Epithelium. Investigative Ophthalmology & Visual Science, 33, 13, pp. 3513-3527.

Roinila, T. Vilkko, M., Suntio, T. 2009.Fast Frequency-response Measurement of Switched-mode Power Supplies in the Presence of Nonlinear Distortions, IEEE Transactions on Power Electronics 25, 8, pp. 2179–2187.

Roinila, T. Vilkko, M., Suntio, T. 2009. Fast Loop Gain Measurement of a Switched-ModeConverter Using a Binary Signal with a Specified Fourier Amplitude Spectrum. IEEE Transactions on Power Electronics 24, 12, pp. 2746–2755.

Roinila, T., Vilkko, M., Taskinen, A. 2009.Improved Fast Frequency Response Measurements of Switched-Mode Power Supplies Using Dirac-Ideal PRBS Excitation, 2nd International Conference on Adaptive Science and Technology, ICAST 2009, Accra, Ghana, December 14–16, IEEE Conference Publications, pp. 175–181.

Savolainen, V. Impedance Measurements of Retinal Pigment Epithelium. Master's Thesis. Tampere 2011. Tampere University of Technology. 77 p.

Savolainen, V., Juuti-Uusitalo, K., Onnela, N, Vaajasaari, H., Narkilahti, S., Suuronen, R., Skottman, H., Hyttinen, J. 2011. Impedance Spectroscopy in Monitoring the Maturation of Stem Cell-Derived Retinal Pigment Epithelium. Annals of Biomedical Engineering 39, 12, pp. 3055–3069.

Schäfer, M. 2012. AW: Contact Form nanoAnalytics. nanoAnalytics GmbH. Reply to email.

Schifferdecker, E., Frömter, E. 1978. The AC Impedance of Necturus Gallbladder Epithelium. Pflugers Archiv European Journal of Physiology 377, pp. 125–133.

Schwan, H.P. & Kay, C.F. 1957.Capacitive Properties of Body Tissues. Circulation Research 5, pp. 439–443.

Schwan, H.P. & Kay, C.F. 1957.The Conductivity of Living Tissue. Annals of the New York Academy of Sciences 65, pp. 1007–1013.

Schwan, H.P. 1992. Linear and Nonlinear Electrode Polarizationand Biological Materials.Annals of Biomedical Engineering 20, pp. 269–288.

Seoane, F., Macías, R., Bragós, R., Lindecrantz, K. 2011.Simple Voltage-controlled Current Source for Wideband Electrical Bioimpedance Spectroscopy: Circuit Dependences and Limitations. Measurement Science and Technology 22, 11, 11 p.

Shanin, A.V. &Valyaev, V.Y. 2011.Method of the Maximum Length Sequences in a Diffraction Experiment. Acoustical Physics 57, 3, pp. 427–431.

Simoes, J.B., Silva, R.M.C., Morgado, A.M.L.S., Correia, C.M. 1995. The Optical Coupling of Analog Signals. Nuclear Science Symposium and Medical Imaging Conference Record, San Francisco, CA, USA, October 21–28, IEEE Conference Publications, pp. 315–317.

Sun, T., Gawad, S., Bernabini, C., Green, N.G., Morgan, H. 2007. Broadband single cell impedance spectroscopy using maximum length sequences: theoretical analysis and practical considerations. Measurement Science and Technology 18, 9, pp. 2859–2868.

Solartron Analytical. 1998.Impedance Measurement Techniques: Sine Correlation. [WWW]. [Cited: 03/05/2012]. Available at:
http://156.17.46.1/pdm/instrukcje/fra/impedtech.pdf

Solartron Analytical. 2011. Systems for the Electrical Characterization of Materials. [WWW].[Cited: 03/05/2012]. Available at: http://www.solartronanalytical.com/Pages/Materials.htm

Solartron Analytical. 2011. ModuLab-MTS System for the Electrical Characterization of Materials. [WWW]. [Cited: 11/07/2012]. Available at:
http://www.solartronanalytical.com/Pages/ModuLab-MTS.htm

SPI Supplies. 2012. Parafilm® M Barrier Film. [WWW].[Cited: 13/08/2012]. Available at: http://www.2spi.com/catalog/supp/parafilm.php

Trebbels, D., Jugl, M., Zengerle, R. 2010.Real-time Cannula Navigation in Biological Tissue with High Temporal and Spatial Resolution Based on Impedance Spectroscopy. Annual International Conference of the IEEE Engineering in Medicine and Biology Society, EMBC'10, Buenos Aires, Argentina, August 31– September 4, 2010.IEEE Conference Publications, pp. 1886–1889.

Vanderkooy, J. 1994. Aspects of MLS Measuring Systems. AES: Journal of the Audio Engineering Society 42, 4, pp. 219–231.

Vishay Semiconductors. 2011. IL300 Datasheet. [WWW].[Cited: 06/07/2012]. http://www.vishay.com/docs/83622/il300.pdf

Vishay Semiconductors. 2012. Designing Linear Amplifiers Using the IL300 Optocoupler – Application Note 50. [WWW].[Cited 03/10/2012]. Available at: http://www.vishay.com/docs/83708/appn50.pdf

Vuorela, T. 2011. Technologies for Wearable and Portable Physiological Measurement Devices. [WWW].[Cited: 05/07/2012]. Dissertation. Tampere. Tampere University of Technology. Publication 962. 106 p. Available at: http://URN.fi/URN:NBN:fi:tty-2011101114828

World Precision Instruments. 2012. EVOM2, Epithelial Voltohmmeter for TEER. [WWW]. [Cited: 30/4/2012]. Available at: http://www.wpiinc.com/index.php/vmchk/EVOM2.html

Wang, W., Brien, M., Gu, D.-W., Yang, J. 2007. A Comprehensive Study on Current Source Circuits.13th International Conference on Electrical Bioimpedance and the 8thConference on Electrical Impedance Tomography, IFMBE Proceedings 17, Graz, Austria, August 29. – September 2., 2007. Springer Verlag.

Zurich Instruments. 2012. HF2IS Impedance Spectroscope. [WWW].[Cited: 11/07/2012]. Available at: http://www.zhinst.com/products/hf2is

Zurich Instruments. 2012. Frequency Sweep Primer. [WWW].[Cited: 25/09/2012]. Available at: http://www.zhinst.com/docs/technotes/zi_hf2_technote_sweep.pdf

APPENDIX 1: EXCITATION SCRIPT

```
%--------------------------------------------------------------------
% NI USB-6251 IRS
%--------------------------------------------------------------------

% Tomi Roinila (29.5.2012)
% Scripts inject the IRS and measures the current.

%--------------------------------------------------------------------
clear
%--------------------------------------------------------------------
% USER-DEFINED VALUES
%--------------------------------------------------------------------
K = 0.2; % excitation amplitude
gen_freq = 10000; % MLBS generation_frequency
sf = 40000; % sampling frequency (integer multiple of gen_freq)
degree = 11; % length of shift register
periods = 30; % number of excitation periods
transient_estimate = 3; % length of transient

C1_max = 10; % maximum value of channel 1
C2_max = 10; % maximum value of channel 2
C1_min = -C1_max; % minimum value of channel 1
C2_min = -C2_max; % minimum value of channel 2

fil = 0 ; % use filter = 1, no filter = 0
BW = 10000; % bandwidth of interest

%--------------------------------------------------------------------
% INITIALIZING THE MEASUREMENT CARD
%--------------------------------------------------------------------
daqreset
daqregister('nidaq')
ai = analoginput('nidaq','Dev1'); % defining input channel
ao = analogoutput('nidaq','Dev1'); % defining output channel

%--------------------------------------------------------------------
% GENERATING THE EXCITATION (NO MORE USER-DEFINED VALUES)
%--------------------------------------------------------------------
mlbs = idinput(2^degree-1,'prbs');
multi = sf/gen_freq; % samples per clock pulse
transient_periods = round((transient_estimate*sf)/(multi*2*(2^degree-1))+0.5);
end_periods = 1;

% Generating auxiliary matrix
aux = [0;1];
auxmat = repmat(aux,2^degree-1,1);

% Generating coefficient matrix
doubled_mlbs = repmat(mlbs,2,1);

% Generating the IRS
irs = 2*xor((doubled_mlbs+1)/2,auxmat)-1;

% Excitation matrix with multigeneration
irs_multi = repmat(irs,multi,1);
```

```
k1 = 0;
for i = 1:length(irs);
   irs_multi(k1*multi+1:(k1+1)*multi) = repmat(irs(i),multi,1);
   k1 = k1+1;
end

% gain
irs_multi = K*irs_multi;

% Designing the low-pass filter
if fil == 1
   filter_co = 2*BW/sf; % filter cut-off with respect to Nyquist frequency
   n = 8; % filter's degree
   [B,A]=cheby1(8,0.1,filter_co);
   y=filter(B,A,[irs_multi; irs_multi; irs_multi]);  % filtered excitation
   irs_multi = y(length(irs_multi)+1:2*length(irs_multi)); % omitting the side effects by choosing the middle period
end

% Following plots the (filtered/non filtered) excitation spectrum
spectrum = db(fft(irs_multi));
f = (0:length(spectrum)-1)'*sf/length(spectrum);
spectrum_irs = nan(length(spectrum)/2,1);
f_irs = nan(length(f)/2,1);

for k = 1:length(spectrum_irs)
   spectrum_irs(k) = spectrum(2*k);
   f_irs(k) = f(2*k);
end

% figure(1), semilogx(f_irs,spectrum_irs,'.'),
% title('Single excitation')
% xlabel('Frequency (Hz)'), ylabel('Gain (dB)'), grid

% Multiplying the single-period excitation
excitation_actual = repmat(irs_multi,periods+transient_periods+end_periods,1);

%-----------------------------------------------------------------
% FREQUENCY RESPONSE MEASUREMENT
%-----------------------------------------------------------------
SampleRate = sf; % sampling frequency
addchannel(ai, 0); % adding input channel
addchannel(ai, 1); % adding input channel
addchannel(ao, 0); % adding output channel

ActualInputRange = setverify(ai.Channel(1),'InputRange',[C1_min C1_max]);
ActualInputRange = setverify(ai.Channel(2),'InputRange',[C2_min C2_max]);
duration = length(excitation_actual)/sf; % duration of measurement process
set(ai,'SampleRate',SampleRate); % input sampling frequency
set(ai,'SamplesPerTrigger',length(excitation_actual)); % number of input samples
set(ao,'SampleRate',SampleRate); % output sampling frequency
putdata(ao, excitation_actual); % excitation into buffer
start([ao ai]); % starting measurement system
wait(ao,duration+0.1); % waiting till end of measurements
measurements = getdata(ai); % collecting measured samples
channel_1 = measurements(:,1); % Input voltage (excitation current)
channel_2 = measurements(:,2); % Output voltage

% Scaling
```

```
channel_1 = channel_1./20000;
channel_2 = (channel_2-mean(channel_2))./30;

figure(3), plot(channel_2), legend('Output voltage')
ylabel('Voltage(V)'),xlabel('Time(s)')

 % Omitting transient and averaging "periods"-number of periods of input-output-data.
L =2*(2^degree-1)*multi; % length of one excitation period (bits)
T = transient_periods*L; % length of transient period (bits)
k = 0;
for i=1:periods
   channel_1_matrix(:,i) = channel_1((T+k*L+1):(T+(k+1)*L));
   channel_2_matrix(:,i) = channel_2((T+k*L+1):(T+(k+1)*L));
   k=k+1;
   i;
end

channel_1_mean = sum(channel_1_matrix(:,:),2)/periods;
channel_2_mean = sum(channel_2_matrix(:,:),2)/periods;

% Admittance
Y = fft(channel_2_mean);   % current spectrum
X = fft(channel_1_mean);   % voltage spectrum

% Following cancels the trash bits
f_irs = (0:length(X)-1)'*sf/length(X);
Y1_irs = nan(length(Y)/2,1);
X1_irs = nan(length(X)/2,1);
f = nan(length(f_irs)/2,1);

for k = 1:length(Y1_irs)
   Y1_irs(k) = Y(2*k);
   X1_irs(k) = X(2*k);
   f(k) = f_irs(2*k);
end

Y = Y1_irs;
X = X1_irs;

Rxx = conj(X) .* X; % energy spectrum of x
Rxy = conj(X) .* Y; % cross-energy spectrum
Hxy = Rxy ./ Rxx;   % frequency response

m = db(Hxy); % magnitude in decibels
p = unwrap(angle(Hxy)); % phase in radians
p = p*180/pi; % phase in degrees

m_s = wsmooth(m,0.01);
p_s = wsmooth(p,0.01);

figure(4),subplot(2,1,1),semilogx(f,m_s,'r.'),axis([10 18000  40 65]),grid
title('Frequency response'),ylabel('Magnitude(dB)')
subplot(2,1,2),semilogx(f,p_s,'r.'),axis([10 18000 -5 5]),grid
xlabel('Frequency (Hz)'),ylabel('Phase(deg)')

data = [f m_s p_s];
% save data data
```

APPENDIX 2: COMPONENT LISTING

The complete component listing of the impedance measurement device

Comment	Description	Designator	Footprint	#	Value
C0603	Ceramic Chip Capacitor - Standard	C1, C3, C4, C5, C11, C12, C13	0603	7	1uF, 10nF, 50pF, 100nF, 470nF, 470pF
C0805	Ceramic Chip Capacitor - Standard	C2	0805	1	4.7uF
Cap Semi	Capacitor (Semiconductor SIM Model)	C6, C7	Panasonic_caps	2	220nF, 470nF
Cap Semi	Capacitor (Semiconductor SIM Model)	C8, C9	0603	2	10nF, 47pF
T491B	Solid Tantalum Chip Capacitor, Standard T491 Series	C10, C14	B	2	10uF
BNC	BNC Elbow Connector	CON1, CON2, CON3	BNC_RA CON	3	
BATT_LOW	LED Panel Mount Indicator (red)	D1	BAT-2	1	
INA331	Low -Power, Single-Supply, CMOS	IA1, IA2	MSOP-8	2	
LT1763-5	500mA, Low Noise, LDO Micropower Reg.	LINREG	SO-8	1	
1251S-02-SM1	Header, Vertical, SMT, 2-Pin	P1	1251S-02-SM1	1	
Res Semi 1%	Semiconductor Resistor	R1- R5, R7, R8, R12 - R21, Rg1 - Rg4	1608[0603]	21	470, 5.6K, 5K, 7K, 10K, 40K, 50K, 51.K, 82K, 100k, 200, 200K, 1Meg
Res Semi 0.1%	Semiconductor Resistor	R6	1608[0603]	1	20K
Res Tap	Tapped Resistor	R_knob	Bourns_pot	1	10K
AD8616	Precision, 20 MHz, CMOS, Rail-to-Rail IO Dual Op Amp.	U1, U3, U4	SO-8_M	3	
LM285M-2.5	Micropower Voltage Reference	U2	SO-8_M	1	
TC54	Voltage Detector	VDET	SOT-23	1	

APPENDIX 3: Complete Schematics of the Device

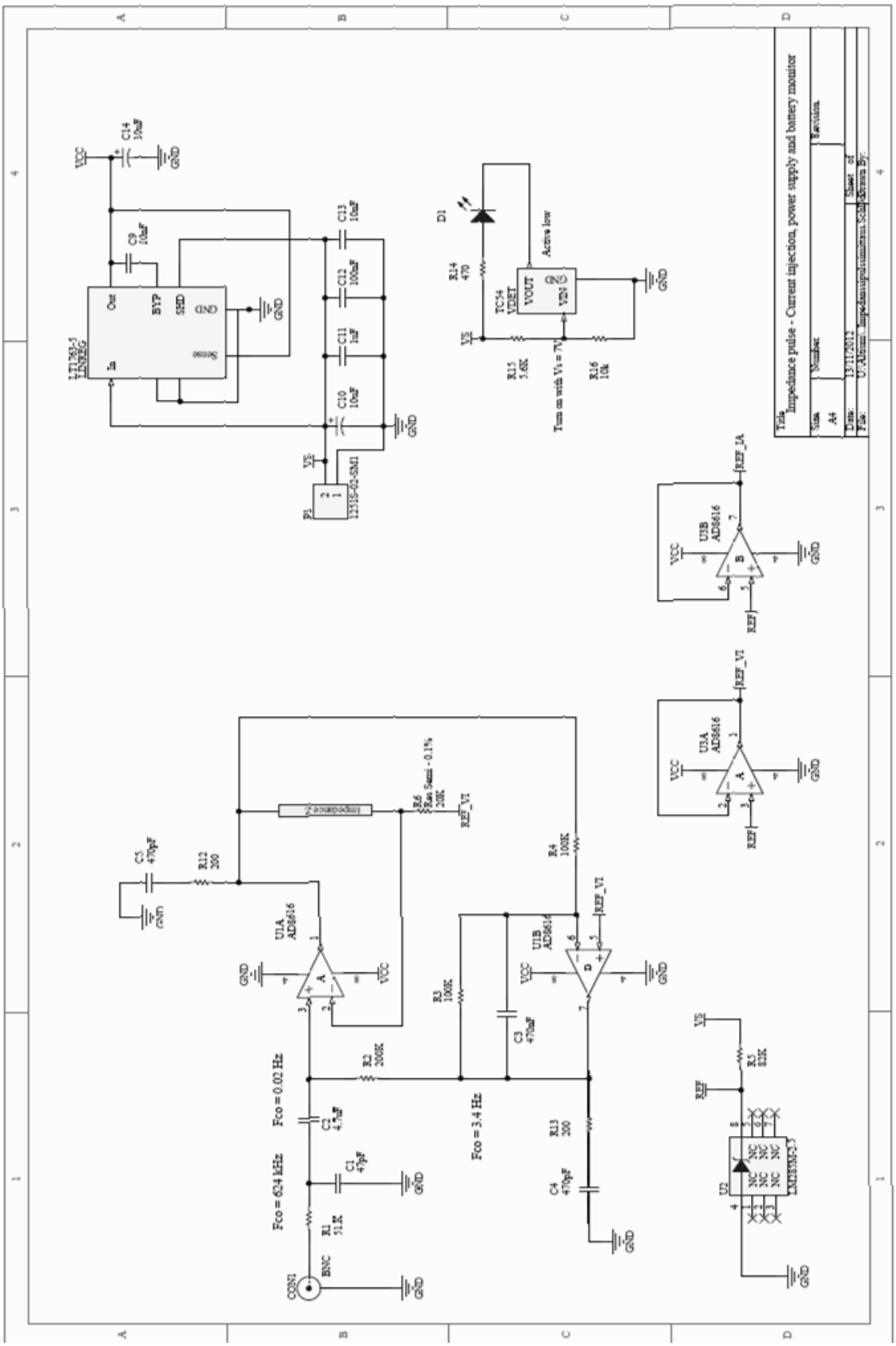

Appendix 3: Figure 5.1. *Current injection block, power supply and battery monitor.*

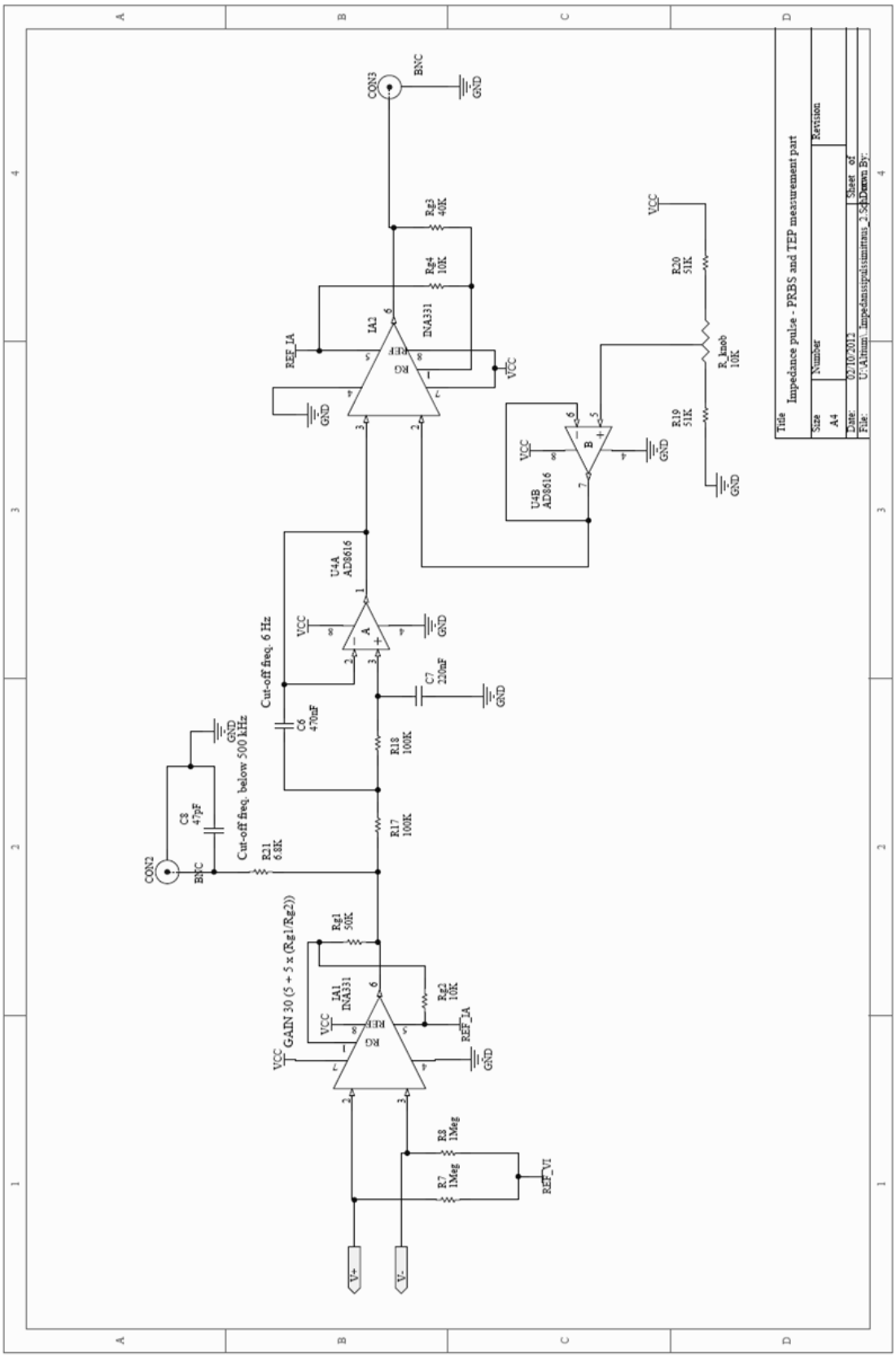

Appendix 3: Figure 5.2. *Voltage sensing, 2. order low pass filtering and TEP offset adjustment.*